

2009

## A Doubly-Fed Induction Generator (DFIG)-Based Wind-Power System with Integrated Energy Storage for Remote Electrification

Faruk Ahmed Bhuiyan

Follow this and additional works at: <https://ir.lib.uwo.ca/digitizedtheses>

---

### Recommended Citation

Bhuiyan, Faruk Ahmed, "A Doubly-Fed Induction Generator (DFIG)-Based Wind-Power System with Integrated Energy Storage for Remote Electrification" (2009). *Digitized Theses*. 3801.  
<https://ir.lib.uwo.ca/digitizedtheses/3801>

This Thesis is brought to you for free and open access by the Digitized Special Collections at Scholarship@Western. It has been accepted for inclusion in Digitized Theses by an authorized administrator of Scholarship@Western. For more information, please contact [wlsadmin@uwo.ca](mailto:wlsadmin@uwo.ca).

# **A Doubly-Fed Induction Generator (DFIG)-Based Wind-Power System with Integrated Energy Storage for Remote Electrification**

(Spine title: DFIG-Based Wind-Power System with Energy Storage)

(Thesis format: Monograph)

by

**Faruk Ahmed Bhuiyan**

2

Graduate Program

in

Engineering Science

Department of Electrical and Computer Engineering

A thesis is submitted in partial fulfilment  
of the requirements for the degree of  
Master of Engineering Science

School of Graduate and Postdoctoral Studies

The University of Western Ontario

London, Ontario, Canada

© Faruk Ahmed Bhuiyan 2009

## Abstract

Electrification of off-grid remote communities is commonly accomplished through diesel generators. The method may even be employed in cases where there exists an unreliable connection to the power grid. Regardless, the method is environmentally-hostile, typically costly, and likely risky. Therefore, to mitigate the reliance on diesel fuel, utilization of renewable energy resources has been considered in recent years. This thesis investigates the feasibility of and technical considerations involved in the employment of a specific class of variable-speed wind-power systems, integrated with battery energy storage, for remote electrification applications.

The wind-power system under consideration is based on the doubly-fed induction generator (DFIG) technology, which features a number of characteristics that render it attractive for the incorporation of battery energy storage. This thesis identifies the control strategy, different control sub-functions, and the controllers structures/parameters required to accommodate the battery energy storage. The developed control strategy enables the operation of the wind-power/storage system in the off-grid (islanded) mode of operation, as well as the grid-connected mode of operation. Under the developed control strategy, the wind-power/storage system can operate in parallel with constant-speed wind-power units, passive loads, and induction motor loads. The effectiveness of the proposed control strategy has been demonstrated through comprehensive simulation studies enabled by the commercial software package PSCAD/EMTDC.

In addition to the control aspects, this thesis studies the reliability aspects of the proposed wind-power/storage system, for an example remote electrification system. Thus, a new reliability assessment method has been developed in this thesis, which combines the existing analytical and simulation-based probabilistic approaches. The reliability analysis conducted indicates that the battery energy storage capacity, the wind magnitude and profile, and the load profile impose remarkable impacts on the reliability of the electrification system. It also indicates that a connection to the power grid, however unreliable, significantly mitigates the need for a large battery to achieve a given degree of reliability.

**Keywords-**Doubly-Fed Induction Generator (DFIG), Wind Power, Remote Electrification, Battery, Energy Storage, Power Electronics, Control, Stability, Micro-grid, Reliability.

## **Acknowledgements**

The research work presented in this thesis has been carried out under the guidance and supervision of Professor Amirnaser Yazdani. I would like to express my sincere and profound gratitude to Professor Amirnaser Yazdani for his invaluable guidance, encouragement, and continuous support during this research work. In addition, financial supports of the Faculty of Engineering of the University of Western Ontario and Natural Sciences and Engineering Research Council of Canada (NSERC) are gratefully acknowledged.

I would also like to thank my wife for her time, care and understanding throughout this research work, and my kids, Farzan and Mehjabin, for their patience.

# Table of Contents

<b>Certificate of Examination</b>	<b>ii</b>
<b>Abstract</b>	<b>iii</b>
<b>Acknowledgements</b>	<b>v</b>
<b>Table of Contents</b>	<b>vi</b>
<b>List of Tables</b>	<b>ix</b>
<b>List of Figures</b>	<b>x</b>
<b>1 Introduction</b>	<b>1</b>
1.1 Statement of the Problem and Thesis Objectives . . . . .	1
1.2 Background . . . . .	4
1.3 Solution Proposed in This Thesis . . . . .	6
1.4 Research Methodology . . . . .	8
1.4.1 Assessment of Technical Feasibility . . . . .	8
1.4.2 Assessment of System Reliability . . . . .	9
1.5 Scope . . . . .	10
1.6 Thesis Outline . . . . .	11
1.7 Contributions . . . . .	12
<b>2 Mathematical Model and Control of the Wind-Power and Storage Unit (WPSU)</b>	<b>14</b>
2.1 Introduction . . . . .	14

2.2	List of Abbreviations and Symbols . . . . .	14
2.3	System Structure of the Study-System . . . . .	18
2.3.1	Wind-Power and Storage Unit (WPSU) . . . . .	18
2.3.2	Distribution Network of the Electrification System . . . . .	20
2.4	Mathematical Model of WPSU . . . . .	21
2.4.1	DFIG Current/Torque Control Scheme . . . . .	22
2.4.2	Grid Side Real/Reactive Power Control Scheme . . . . .	24
2.5	Real- and Reactive-Power Management Schemes . . . . .	26
2.5.1	Real-Power Management Scheme . . . . .	26
2.5.2	Reactive-Power Management Scheme . . . . .	30
2.5.3	Pitch-Angle Control Scheme . . . . .	31
2.6	Simulation Results . . . . .	32
2.7	Summary . . . . .	46
<b>3</b>	<b>Stability Analysis of the Wind-Power and Storage Unit (WPSU)</b>	<b>48</b>
3.1	Introduction . . . . .	48
3.2	Linearization of a Nonlinear System . . . . .	49
3.3	Small-Signal Model of WPSU . . . . .	52
3.3.1	Linearized Model of the DFIG Subsystem . . . . .	52
3.3.2	Linearized Model of the PLL Subsystem . . . . .	54
3.3.3	Linearized Model of the Capacitor Subsystem . . . . .	54
3.3.4	Linearized Model of the GSC Subsystem . . . . .	55
3.3.5	Overall Linearized Model . . . . .	56
3.4	Stability of the WPSU . . . . .	58
3.5	Robustness of the WPSU . . . . .	59
3.6	Summary . . . . .	62
<b>4</b>	<b>Reliability of the Remote Electrification System</b>	<b>63</b>
4.1	Introduction . . . . .	63
4.2	List of Symbols . . . . .	63
4.3	Background on Reliability Assessment Methods . . . . .	65

4.4	Study System . . . . .	66
4.4.1	Reliability Indices . . . . .	68
4.4.2	Proposed Hybrid Approach for Reliability Assessment . . . . .	69
4.5	Grid-Side Converter (GSC) Rating . . . . .	81
4.6	Simulation Results . . . . .	83
4.6.1	Case-1: Impact of Units FOR on the LOLE . . . . .	86
4.6.2	Case-2: Impact of Load Distribution and Maximum Yearly Peak Power on the LOLE. . . . .	86
4.6.3	Case-3: Impact of Wind Profile and Magnitude on the LOLE. . . . .	87
4.6.4	Case-4: Impact of Maximum Permissible Battery Power on the LOLE . . . . .	88
4.6.5	Case-5: Impact of Grid FOR on the LOLE . . . . .	89
4.6.6	Case-6: Impact of Number of Generators on the LOLE . . . . .	90
4.6.7	Case-7: Grid-Side Converter Rating . . . . .	92
4.7	Summary . . . . .	93
<b>5</b>	<b>Conclusions and Future Work</b>	<b>94</b>
5.1	Conclusions . . . . .	94
5.2	Future Work . . . . .	96
	<b>Appendices</b>	<b>97</b>
<b>A</b>	<b>System Data</b>	<b>98</b>
<b>B</b>	<b>Nonlinear and Linearized Equations</b>	<b>102</b>
B.0.1	Equations of DFIG Subsystem . . . . .	102
B.0.2	Equations of PLL Subsystem . . . . .	104
B.0.3	Equations of Capacitor Subsystem . . . . .	105
B.0.4	Equations of GSC Subsystem . . . . .	105
	<b>References</b>	<b>107</b>
	<b>Vita</b>	<b>112</b>

# List of Tables

3.1	Eigenvalues of the WPSU for Different Wind Speeds . . . . .	59
3.2	WPSU State Variables and Their Participation Factors (Wind Speed=9.0 <i>m/s.</i> ) . . . . .	61
3.3	WPSU State Variables and Their Participation Factors (Wind Speed=12.0 <i>m/s.</i> ) . . . . .	62
4.1	States Probabilities for Generator $k$ . . . . .	77
4.2	Explanation of Subscript $j$ in $S_{ij}^{(k)}$ ( $i = 1$ or $2$ ) . . . . .	78
4.3	State Probabilities and Corresponding Power Outputs for the System of Fig. 4.1 . . . . .	79
4.4	Numerical Version of the Capacity-In Probability Table of Table 4.3 . . . .	85
4.5	Reliability Indices for the System of Fig. 4.1 and a Hypothetical Four- Generator System . . . . .	91
A.1	Control System Parameters . . . . .	98
A.2	DFIG and Constant-speed Turbine Parameters . . . . .	99
A.3	DFIG Parameters . . . . .	99
A.4	Power-Electronic Interface and Network Parameters . . . . .	100
A.5	Induction Generator and Motor Parameters . . . . .	101
A.6	Base Values for the WPSU Parameters . . . . .	101

# List of Figures

2.1	Schematic diagram of (a) the Wind-Power and Storage Unit (WPSU), and (b) distribution network of the remote site . . . . .	19
2.2	Block diagram of the real-power management scheme . . . . .	26
2.3	Block diagram of the dc-link voltage regulation scheme . . . . .	28
2.4	Block diagram of the reactive-power management scheme . . . . .	31
2.5	Case1: waveforms of (a) dc-link voltage, (b) DFIG speed and generated power, and (c) battery power and DFIG delivered real power . . . . .	34
2.6	Case2: waveforms of (a) DFIG generated and delivered real powers, (b) battery power, (c) dc-link voltage, and (d) GSC real power . . . . .	36
2.7	Case3: waveforms of (a) delivered real power, (b) DFIG speed, (c) DFIG generated power, (d) GSC real power, (e) frequency, and (f) battery power . . . . .	38
2.8	Case3: waveforms of (a) delivered reactive power, (b) GSC reactive power, and (c) PCC voltage magnitude . . . . .	39
2.9	Case3: waveforms of (a) PCC voltage, (b) current injected into the distribution network, (c) DFIG stator current, and (d) DFIG rotor current . . . . .	40
2.10	Case4: waveforms of (a) wind speed, (b) battery power and delivered real power, and (c) pitch angle . . . . .	42
2.11	Case4: waveforms of (a) DFIG speed, (b) PCC voltage magnitude, and (c) frequency . . . . .	43
2.12	Case5: waveforms of (a) PCC voltage, (b) load real and reactive powers, and (c) motor load and DFIG speeds . . . . .	44
2.13	Case6: system responses in the islanded mode, under parallel operation of the WPSU and the CSU . . . . .	46

4.1	Single line schematic diagram of the remote electrification system . . . . .	67
4.2	Load Duration Curves (LDCs) corresponding to three different load models	73
4.3	State transition diagram for a wind-power unit without energy storage . . .	76
4.4	Variations of (a) slip and (b) rotor power as functions of the wind speed . .	82
4.5	Variations of LOLE vs. battery capacity, for different FOR . . . . .	86
4.6	LOLE vs. $E_{max}$ curves for different (a) load distributions, and (b) load yearly peak powers . . . . .	87
4.7	LOLE vs. $E_{max}$ curves for different (a) wind-speed time series, and (b) wind speed magnitudes . . . . .	88
4.8	LOLE vs. $E_{max}$ curves for (a) $P_{dch-max} = 350 kW$ and different values of $P_{ch-max}$ ; (b) $P_{ch-max} = 800 kW$ and different values of $P_{dch-max}$ . . . . .	89
4.9	LOLE vs. $E_{max}$ curves in the grid-connected mode, for (a) different values of the grid FOR and (b) for FOR=15% totally random and FOR=15% with 96 hours continuous down . . . . .	90
4.10	A curve indicating the total number of hours per year during which the GSC power exceeds a certain value on the vertical axis . . . . .	92

# **Chapter 1**

## **Introduction**

### **1.1 Statement of the Problem and Thesis Objectives**

Electrification of remote communities and islands remains a burden on many utility companies in Canada and across the world. The reason is mainly the cost and/or technical complications involved in constructing transmission lines. Thus, the delivery of electricity to remote communities is either entirely overlooked or it is handled through costly and environmentally-hostile methods, most notably through the diesel-based generation. In addition to the cost, labor, and risks associated with the fuel transportation process, diesel generators are inefficient and pollute the environment. Thus, a need is felt for development of remote electrification systems that are less dependent on diesel fuel, but rely more on renewable energy resources which may be available at the sites. Among renewable energy resources, wind is potentially the most technically- and economically-viable one, due to its typical abundance in many remote sites, remarkable advancements in the technology, decreasing extraction costs, and large investments made by

governments and the private sector. However, the intermittency and uncontrollability of wind energy must be compensated by some sort of energy storage mechanism, to make the overall electrification system suitable for off-grid remote sites.

To electrify a remote site, whether off-grid or through an unreliable connection to the grid, a variable-speed wind-power unit with an integrated battery energy storage may be a suitable option, provided that the area has adequate wind energy. A variable-speed wind-power unit employs a power-electronic converter which enables a superior wind energy capture and greater controllability. Moreover, the intermediate dc link of the power-electronic converter renders a variable-speed wind-power unit potentially suitable for direct interfacing with a battery bank. A wind-power unit with energy storage can be employed independently, if an adequate energy storage capacity is provided, or it can augment the existing diesel generators to reduce their burden and mitigate the reliance on diesel fuel. Amongst different variable-speed wind-power technologies, the one based on the Doubly-Fed Induction Generator (DFIG) accommodates a reduced-size electronic power converter while offers the same technical features of the other variable-speed technologies. Thus, this thesis has been dedicated to an investigation on the suitability of a DFIG-based wind-power unit augmented with battery energy storage, for remote electrification. Hereinafter, we refer to the DFIG-based wind-power unit with the energy storage as the “*Wind-Power and Storage Unit*” (WPSU).

This thesis:

1. Proposes an effective control strategy that enables the WPSU to operate in the islanded as well as the grid-connected mode of operation, with the capability to smoothly switch from one mode to the other mode.

The proposed control strategy:

- guarantees voltage and frequency regulation in the islanded mode of operation;
  - provides protection against a dc-link voltage runaway if the battery fails due to death or conductor rupture, or it is out for maintenance;
  - enables the WPSU to operate in parallel with diesel generators, similar units, or other types of Distributed Generation (DG) units; and
  - employs a vectorial torque-control strategy for the generator that enables maximization of the power extracted from the turbine.
2. Formulates a mathematical model for the WPSU that enables stability analysis, characterization of dynamics, and selection of controllers parameters.
  3. Develops a new methodology for assessment of the reliability of the WPSU, with respect to the energy storage capacity, wind potential of the site, failure rates of the components, etc.

## 1.2 Background

Worldwide, about two billion people living in rural areas and islands have no access to electricity [1]. In Canada, there are more than three hundred remote communities that are isolated from the power system [2]. In Northern Ontario, alone, there are about thirty off-grid remote communities whose electricity is exclusively supplied by diesel generators [3]. Many other remote communities are connected to the power system via unreliable transmission lines which pass through rough terrains or forests and, as such, experience frequent downtimes due to landslides or wildfires. Presently, the state-of-the-art remote electrification technique is to utilize diesel generators [2]– [4], due to their simplicity, ruggedness, and acceptable reliability. However, diesel generators are rather inefficient and pollute the environment. Moreover, the transportation of diesel fuel can be costly and risky. Therefore, a fair number of studies have been dedicated in the recent past to the subject of augmenting diesel-based electric power generation with renewable energy resources [5]– [10].

Reference [5] investigates the effect of energy storage in different wind-diesel system configurations, from the economic operation viewpoint. Reference [6] discusses different system configurations, and the economics associated with major components of a solar/wind/diesel system which also includes energy storage. In [7] the economic dispatch problem in wind-diesel hybrid systems has been investigated. Reference [8] deals with the modeling and performance of a wind-diesel hybrid system based on an electronically-coupled squirrel-cage asynchronous generator.

In [9] an electronically-controlled, variable-frequency, wind-diesel hybrid system has been proposed to improve the overall system efficiency. Reference [10] proposes a stand-alone wind-power unit which is based on the asynchronous generator and a reduced-rating voltage-sourced converter, (abbreviated as VSC). The systems proposed in references [8]- [10] require dump loads to maintain the voltage and frequency, in scenarios where the load demand is low while the wind speed is high, and are therefore wasteful of energy. This issue can be resolved if the stand-alone electrification system is augmented with some sort of energy storage. Energy storage also acts as an effective means to mitigate the impact of wind power fluctuations and consequent power quality problems [11]. A properly sized energy storage enables a wind-power system to operate in isolation of the utility grid [12]- [13], at least for a reasonable period. In case that a remote community is connected to a weak grid, the incorporation of energy storage enhances the reliability of supply [14] and ensures the continuity of service [11].

Many previous research works have investigated the technical and/or economical advantages of augmenting a wind-power system with energy storage, for example, based on hydrogen [15], batteries [11], [16], hybrid Static Synchronous Compensator (STATCOM) [17], Compressed-Air Energy Storage (CAES) [18], and pumped hydro [19]. However, the aforementioned energy storage technologies require geographically suitable sites. Moreover, they are economically viable only for large-scale wind-power systems where economies of scale justify the cost of dedicated equipment and infrastructure. However, for a small-scale wind-power system, e.g. a

few wind-power units serving a remote community, it is potentially more economical to upgrade and utilize the built-in system hardware and control software to integrate the energy storage; this has been the motivation behind the solution proposed in this thesis.

### **1.3 Solution Proposed in This Thesis**

Wind-power systems are broadly classified as the “constant-speed” and the “variable-speed” systems. A constant-speed wind-power unit is basically an asynchronous generator that is directly interfaced with the power system. Therefore, it essentially rotates at an angular velocity dictated by the power system frequency and, consequently, yields a relatively poor energy capture. Moreover, its stand-alone operation, i.e. in isolation of the power system, is not straightforward. Furthermore, its direct connection to the grid brings about power quality problems, mechanical stress, and a relatively demanding reactive-power requirement. By contrast, a variable-speed wind-power unit employs a power-electronic converter and, therefore, extracts more energy from wind. It also operates more smoothly, while demands insignificant reactive power; the cost of the additional power-electronic and control equipment of a variable-speed wind-power unit is justified in view of its superior energy capture and potentially lower need for major maintenance or repair operations.

Presently, variable-speed wind-power units are dominated by the Doubly-Fed Induction Generator (DFIG) technology [20]. The main advantage of a DFIG-based wind-power unit is that its power-electronic converter can be

rated at a considerably smaller capacity as compared to the output rating of the wind-power unit. Moreover, the intermediate dc link of the converter, combined with the converter rapid response, renders a DFIG-based wind-power unit attractive for integration with such energy storage devices as flywheels, supercapacitors, or batteries [21]- [22]. Reference [22] discusses that a grid-connected DFIG-based wind-power unit augmented with energy storage can deliver a regulated amount of real power to the host grid, despite wind speed/power fluctuations. In addition, incorporation of energy storage into a DFIG-based wind-power unit makes it dispatchable and, therefore, capable to operate in the islanded mode of operation [23].

Expanding on the ideas proposed in [22] and [23], this thesis proposes a unified control strategy for a DFIG-based WPSU. The proposed control strategy enables operation in the islanded as well as the grid-connected mode of operation. For the grid-connected mode, the proposed control strategy relieves the need for modification of the control algorithm or reconfiguration of the hardware, to accommodate the battery storage. On the other hand, if the WPSU is to be used without the battery storage, the proposed control strategy requires no reconfiguration of the software and/or the hardware, to permit the operation. Thus, the proposed control strategy preserves the characteristics of a conventional DFIG-based wind-power unit, as well as those featured in [22]. Moreover, the proposed control strategy renders the WPSU protected against sudden disconnection or failure of the battery bank.

The proposed control strategy also enables the WPSU to continue to

operate subsequent to an islanding incident, and to regulate the voltage and frequency of the islanded distribution network, despite load/generation fluctuations. The regulation task is based on the reactive-power versus voltage ( $Q - V$ ) and the real-power versus frequency ( $P - \omega$ ) droop techniques [24]-[25]. The real and reactive power are controlled based on a current-mode control strategy which mitigates dynamic cross-couplings and also provides an effective protection against external faults. Using the proposed control strategy, in the islanded mode the WPSU can operate in parallel with constant-speed wind-power units, induction motor loads, and passive loads; the WPSU is also expected to be able to operate in parallel with similar wind-power units, diesel generators, Photovoltaic (PV) units, etc.

## **1.4 Research Methodology**

The material presented in this thesis describes two main tasks: one is the assessment of the technical feasibility of the proposed solution, with respect to the control, stability, and performance; and the other one is the evaluation of the system reliability as well as the requirements for the energy storage capacity, components ratings, etc. The methodologies adopted to carry out each task are explained as follows.

### **1.4.1 Assessment of Technical Feasibility**

To assess the technical feasibility of the proposed solution, the following steps have been taken:

1. A large-signal mathematical model has been developed for a conventional DFIG-based wind-power unit. The developed model is then augmented to include the impact of an added battery energy storage.
2. Based on the developed mathematical model, a unified control strategy has been devised to enable both the grid-connected and islanded modes of operation. Further, different sub-controllers, their expected functions, and their structures have been identified.
3. The mathematical model, combined with the controls, have been linearized, a stability analysis conducted, and the controller parameters calculated.
4. A detailed topological model of the overall system has been developed and simulated in the PSCAD/EMTDC [26] software environment, to verify and possibly refine the design. This step is considered as a close approximation of an experimental set-up. The flexibility offered by the software simulation has enabled testing of different operational scenarios, with no fear of components failure, equipment limitations, etc.

#### **1.4.2 Assessment of System Reliability**

To assess the reliability of the proposed system, the following steps have been taken:

1. A new model for reliability assessment has been developed which is a combination of probabilistic and simulation-based approaches. This hybrid model combines the advantages of the two foregoing methods,

while it largely avoids their limitations. The developed model takes into account the chronological variations of wind speed at the site, failure rates of the system components, battery state-of-charge, and the grid reliability. In return, the model determines the battery capacity that is required to achieve a certain degree of reliability.

2. The proposed hybrid model has been implemented in MATLAB software environment, and a comprehensive set of sensitivity analyses has been performed to characterize the impact on the battery capacity of such factors as wind profile and magnitude, components failure rates, number of units within the electrification system, and grid reliability, for a desired reliability.

## **1.5 Scope**

It is understood that, at the time of writing, batteries are quite expensive and subject to major overhauls once every few years. It is also recalled that new battery technologies are emerging [27]- [28]. These need to be considered in the economic analysis of the electrification system, at the planning stage. Such an analysis is quite involved and outside the scope of this thesis. Thus, a simplified battery model has been adopted in this thesis, irrespective of any particular technology. The adopted model, however, provides a fair description of a lead-acid battery. A more detailed investigation may be conducted to identify the battery technology most suitable for the proposed solution.

## 1.6 Thesis Outline

The rest of the thesis is organized in four chapters, as follows.

- In Chapter 2, a mathematical model has been derived for the WPSU and its control subsystems. In addition, the principles of operation of the WPSU have been explained and the study test system introduced. Chapter 2 also presents different simulation case studies to verify the effectiveness of the WPSU and the controls under normal as well as adverse operating conditions.
- The Chapter 3 presents a small-signal, linearized, model for the WPSU, to enable an eigenvalue analysis to evaluate the stability of the proposed control strategy.
- The Chapter 4 conducts a reliability analysis on the WPSU, based on a new methodology. The proposed reliability-assessment methodology combines the probabilistic and simulation-based approaches, and is less computationally involved. Using the proposed reliability-assessment approach, the capacity of the battery energy storage can be determined as a function of a desired degree of reliability.
- Chapter 5 concludes the thesis and suggests a few future research topics related to the WPSU;

## 1.7 Contributions

The contributions of this thesis are summarized as follows:

1. The thesis proposes a mathematical model and a control strategy that enables incorporation of battery energy storage into a DFIG-based wind power unit. The proposed control strategy enables the grid-connected mode of operation, the islanded mode of operation, and smooth transition from one mode to the other. The implementation of the proposed control strategy requires no modifications in the electronic hardware or the control software of a conventional DFIG-based wind-power unit and, therefore, can be appealing to manufacturers. Based on the proposed control strategy, the WPSU preserves all the features of a conventional DFIG-based wind-power unit, while is able to operate in isolation of the power system, in parallel with other generators. The WPSU and its proposed control strategy, thus, is potentially suitable for remote electrification systems, which may be either isolated from the power system, or their connection to the power system is through unreliable transmission lines.
2. The thesis proposes a new approach for the reliability assessment of the WPSU, which with minor modifications can also be applied to other system configurations. The proposed approach combines the probabilistic and simulation-based methods, is adequately accurate, and is less computationally involved. Using the proposed reliability assessment method, the capacity of the battery energy storage can be deter-

mined for a desired degree of reliability. Moreover, factors such as wind profile and magnitude, battery state-of-charge, number of units in the electrification system, grid reliability, etc., are accounted for.

## **Chapter 2**

# **Mathematical Model and Control of the Wind-Power and Storage Unit (WPSU)**

### **2.1 Introduction**

This chapter introduces the structure, principles of operation, the mathematical model, and the control schemes of the Wind-Power and Storage Unit (WPSU). In addition, the test system used to verify the design and evaluate the system performance is introduced in this chapter. The model and control loops introduced in this chapter are linearized in Chapter 3 and used for stability analysis of the WPSU.

### **2.2 List of Abbreviations and Symbols**

The following abbreviations and symbols are specific to this chapter and Chapter 3.

- WPSU*** : Wind-power and storage unit
- CSU*** : Constant-speed wind-power unit
- DFIG*** : Doubly-fed induction generator
- PCC*** : Point of common coupling
- RSC*** : Rotor-side converter
- GSC*** : Grid-side converter
- pu*** : per-unit
- s*** : Complex frequency
- Tr<sub>(.)</sub>*** : Interface transformer
- B<sub>(.)</sub>*** : Breaker
- i<sub>s</sub>*** : DFIG stator current
- i<sub>r</sub>*** : DFIG rotor current
- i<sub>b</sub>*** : Battery current
- i<sub>c</sub>*** : AC-side current of the GSC
- i<sub>t</sub>*** : Current delivered to the network, at the PCC, by the WPSU
- i<sub>cs</sub>*** : Current of the CSU
- i<sub>L</sub>*** : Load current
- i<sub>g</sub>*** : Grid current
- v<sub>s</sub>*** : DFIG stator voltage
- v<sub>sm</sub>*** : Peak value of the DFIG stator line-to-neutral voltage
- v<sub>r</sub>*** : DFIG rotor voltage
- v<sub>b</sub>*** : Battery voltage
- v<sub>c</sub>*** : AC-side voltage of the GSC
- v<sub>dc</sub>*** : DC-link voltage

- $V_{dc-L}$  : Minimum permissible DC-link voltage  
 $V_{dc-H}$  : Maximum permissible DC-link voltage  
 $v_t$  : Voltage at the PCC  
 $v_g$  : Grid voltage  
 $P_e$  : DFIG electrical power  
 $P_s$  : Real power leaving the DFIG stator  
 $P_r$  : Real power delivered by the DFIG rotor windings  
 $P_b$  : Battery power  
 $P_c$  : Real power leaving the AC-side terminals of the GSC  
 $P_t$  : Real power delivered by the WPSU to the network, at the PCC  
 $P_{cs}$  : Real power delivered by the CSU  
 $P_L$  : Load real power  
 $P_g$  : Real power delivered to the grid  
 $Q_s$  : Reactive power leaving the DFIG stator  
 $Q_c$  : Reactive power leaving the AC-side terminals of the GSC  
 $Q_f$  : Reactive power supplied by  $C_f$   
 $Q_t$  : Reactive power delivered by the WPSU to the network, at the PCC  
 $Q_{cs}$  : Reactive power delivered by the CSU  
 $Q_L$  : Load reactive power  
 $Q_g$  : Reactive power delivered to the grid  
 $\theta_s$  : Phase angle of the DFIG stator voltage  
 $\omega$  : Angular frequency of the DFIG stator voltage  
 $\theta_r$  : DFIG rotor mechanical angle  
 $\omega_r$  : Angular velocity of the DFIG rotor

- $\omega_0$  : Steady-state angular frequency of the grid  
 $\sigma_s$  : DFIG stator leakage factor  
 $\lambda_{sm}$  : Peak value of the stator flux  
 $L_m$  : DFIG magnetizing inductance  
 $L$  : Inductance of the GSC interface reactor  
 $L_b$  : Inductance to smooth the battery current  
 $L_1$  : Inductance of the  $R - L$  load  
 $L_g$  : Inductance of the transmission line  
 $R$  : Resistance of the GSC interface reactor  
 $R_b$  : Battery resistance  
 $R_1$  : Resistance of the  $R - L$  load  
 $R_g$  : Resistance of the transmission line  
 $C_f$  : Capacitance of the shunt AC filter  
 $C_L$  : DC-link capacitance  
 $C_2$  : Power-factor correction capacitance of the induction motor load  
 $\tau_{(.)}$  : Time constant of the closed current-control loop  
 $N$  : Gearbox ratio  
 $r$  : Turbine radius  
 $A$  : Turbine swept area  
 $C_{pmax}$  : Peak value of the turbine power efficiency curve  
 $T_{tur}$  : Turbine mechanical torque  
 $T_e$  : DFIG electrical torque  
 $\lambda_{opt}$  : Turbine tip-speed ratio  
 $V_w$  : Wind speed

## 2.3 System Structure of the Study-System

The schematic representation of the DFIG-based wind-power unit and the distribution network is shown in Fig. 2.1. The detailed description of this study system is organized as follows:

### 2.3.1 Wind-Power and Storage Unit (WPSU)

Fig. 2.1(a) illustrates a single-line schematic diagram of the “Wind-Power and Storage Unit” (WPSU). The WPSU comprises a wind-turbine, a gear-box, a DFIG, a back-to-back AC-DC-AC converter, and an interface transformer. As Fig. 2.1(a) indicates, the WPSU is interfaced with a distribution network, Fig. 2.1(b), at a Point of Common Coupling (PCC) and through the interface transformer  $Tr_1$ . Fig. 2.1(a) also shows that the DFIG stator is directly connected to the low-voltage side of  $Tr_1$ , whereas the rotor circuit is interfaced with  $Tr_1$  via the breaker  $B_r$ , the AC-DC-AC converter, and the breaker  $B_c$ . Fig. 2.1(a) further shows that a three-phase capacitor,  $C_f$ , is connected to the low-voltage side of  $Tr_1$ , to suppress the switching voltage harmonics generated by the AC-DC-AC converter. However,  $C_f$  also supplies a relatively small reactive power,  $Q_f$ . The real and reactive power that the WPSU delivers to the distribution network are denoted by  $P_t$  and  $Q_t$ , respectively, and referred in this chapter to as the “*delivered real power*” and the “*delivered reactive power*”.

As shown in Fig. 2.1(a), the AC-DC-AC converter itself is composed of two back-to-back connected two-level voltage source converters (VSC). The VSCs are labeled as the rotor-side converter (RSC) and the grid-side

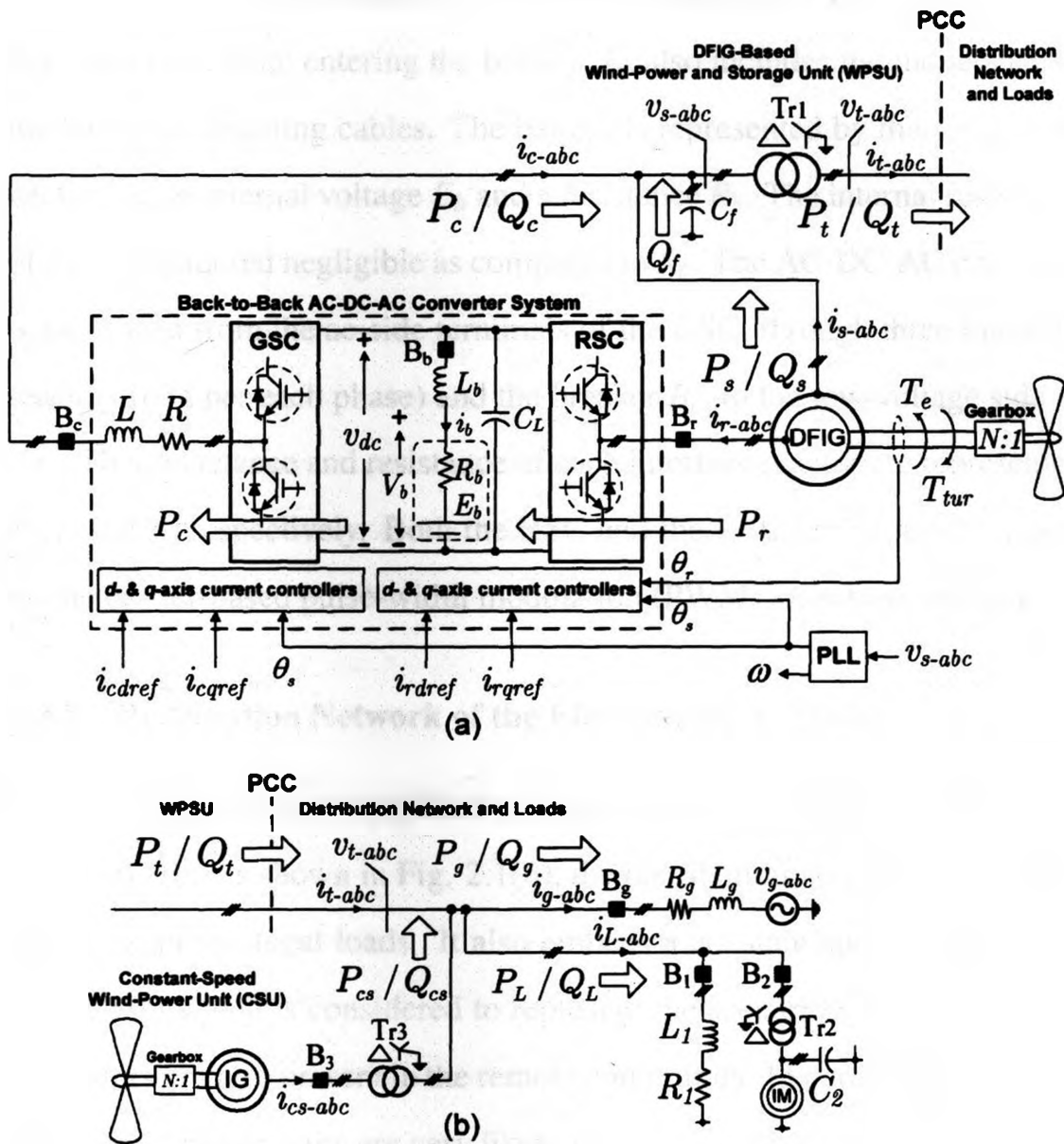


Fig. 2.1: Schematic diagram of (a) the Wind-Power and Storage Unit (WPSU), and (b) distribution network of the remote site

converter (GSC), whose dc sides are connected in parallel to the dc-link capacitor  $C_L$  and a battery bank. The battery bank, hereinafter referred to as the “battery”, consists of an array of series-/parallel-connected low-voltage battery cells. The inductor  $L_b$ , shown in series with the battery, may be in-

stalled to prevent high-frequency components of the dc-side currents of the RSC and GSC from entering the battery.  $L_b$  also includes the inductance of the battery connecting cables. The battery is represented by the series connection of an internal voltage  $E_b$  and a resistance  $R_b$ . The internal resistance of  $L_b$  is considered negligible as compared to  $R_b$ . The AC-DC-AC converter is interfaced from the ac-side terminals of the GSC, through three interface reactors (one per each phase) and the breaker  $B_c$ , to the low-voltage side of  $Tr_1$ . The inductance and resistance of each interface reactor are represented by  $L$  and  $R$ , respectively. Both the RSC and the GSC are controlled based on the carrier-based pulse-width modulation (PWM) switching strategy.

### 2.3.2 Distribution Network of the Electrification System

Fig. 2.1(b) illustrates a simplified schematic diagram of the remote distribution network. As shown in Fig. 2.1(b), the distribution network includes an aggregate of the local loads. It also embeds a constant-speed wind-power unit (CSU) which is considered to represent the scenario where distributed generators are also present in the remote community. In particular, constant-speed wind-power units are very likely to exist in such a community, due to their low cost, simplicity, and ruggedness. Fig. 2.1(b) also shows a transmission line that links the distribution network to the power system. The power system is represented by an ideal three-phase voltage source,  $v_{g-abc}$ . The transmission line is represented by a series  $R - L$  branch whose inductance and resistance are  $L_g$  and  $R_g$ , respectively. The distribution network can be isolated from the power system by means of the breaker  $B_g$ .

The remote distribution network is assumed to be of a limited geographical span. Therefore, the inductances and resistances of the feeders are ignored or lumped with those of the loads.

Fig. 2.1(b) shows that the aggregate of the local loads is represented by the parallel connection of a series  $R - L$  branch and an induction motor. The inductance and the resistance of the  $R - L$  load are  $L_1$  and  $R_1$ , respectively. The  $R - L$  load can be isolated from the network by the breaker  $B_1$ . The induction motor load is interfaced with the network through the transformer  $Tr_2$  and drives a mechanical load whose torque is proportional to the square of its angular velocity. The induction motor load can be isolated from the network by means of the breaker  $B_2$ . A three-phase shunt capacitor,  $C_2$ , provides power-factor correction for the induction motor.

Fig. 2.1(b) also shows that the CSU unit is interfaced with the distribution network through the transformer  $Tr_3$ . The real and reactive power that the CSU exchanges with the network are denoted by  $P_{cs}$  and  $Q_{cs}$ , respectively. It should be pointed out that  $Q_{cs}$  is negative since the CSU is a consumer of reactive power. The CSU can be isolated from the network by means of the breaker  $B_3$ .

## 2.4 Mathematical Model of WPSU

The overall control system can be divided into two subsystems: 1) the DFIG current/torque control, and, 2) the grid real and reactive power control. The former is exercised through the control of the RSC, while the latter is enabled by the control of the GSC. Each control subsystem is described in the

following sections.

### 2.4.1 DFIG Current/Torque Control Scheme

The first control sub-system of the WPSU, Fig. 2.1(a), is the torque-control scheme. The function of the torque-control scheme is to control the DFIG torque through a vectorial control strategy, to maximize the power extracted from wind by the wind turbine. The turbine (and thus the DFIG) power is maximized if the DFIG torque is changed according to the following law [29]:

$$T_e \simeq T_{eref} = k_{opt}\omega_r^2 \quad (2.1)$$

where  $T_e$  is the DFIG torque,  $T_{eref}$  is the torque reference command, and  $\omega_r$  is the DFIG shaft speed. The proportionality constant  $k_{opt}$  is

$$k_{opt} = \frac{0.5\rho Ar^3 C_{pmax}}{N^3 \lambda_{opt}^3}, \quad (2.2)$$

where  $\rho$  is the air density in  $kg/m^3$ ,  $A = \pi r^2$  is the turbine swept area in  $m^2$ ,  $r$  is the turbine radius in  $m$ , and  $N$  is the gearbox ratio.  $C_{pmax}$  (unit-less) is the peak value of the turbine power-efficiency curve and a decreasing function of the turbine pitch angle. In (2.2),  $C_{pmax}$  is evaluated at zero pitch angle.  $\lambda_{opt}$  (unit-less) is the turbine tip-speed ratio corresponding to  $C_{pmax}$  [20].

If the DFIG is controlled in its stator-flux coordinates,  $T_e$  is expressed as [30]:

$$T_e = \frac{3}{2} \frac{1}{1 + \sigma_s} \lambda_{sm} i_{rq}, \quad (2.3)$$

where  $\sigma_s$  is the stator leakage factor,  $\lambda_{sm}$  is the amplitude of the stator flux, and  $i_{rq}$  is the quadrature component of the rotor current.  $\lambda_{sm}$  can be approximated as  $v_{sm}/\omega$ , where  $v_{sm}$  is the peak value of the stator line-to-neutral voltage and  $\omega$  is the frequency of the stator voltage. Assuming that  $\omega$  is approximately (in the islanded mode of operation) or precisely (in the grid-connected mode of operation) equal to the standard power system frequency, i.e.  $\omega_0$ ,  $\lambda_{sm}$  can be replaced by  $v_{sm}/\omega_0$  in (2.3), and one obtains

$$T_e = \frac{3}{2} \frac{v_{sm}}{(1 + \sigma_s)\omega_0} i_{rq}. \quad (2.4)$$

The reference command for  $i_{rq}$  can then be calculated in terms of  $T_{eref}$ , based on (2.4), as

$$i_{rqref}(t) = \frac{(1 + \sigma_s)\omega_0}{1.5v_{sm}} T_{eref}(t), \quad (2.5)$$

where  $T_{eref}$  is determined by (2.1). Multiplying both sides of (2.1) by  $\omega_r$ , one can express the DFIG generated power as

$$P_e \approx k_{opt}\omega_r^3. \quad (2.6)$$

The control law (2.6) results in a constant tip-speed ratio [29]. Hence,  $\omega_r$  becomes proportional to the wind speed,  $V_w$ , and (2.6) can be rewritten as

$$P_e \approx \left( \frac{N\lambda_{opt}}{r} \right)^3 k_{opt} V_w^3. \quad (2.7)$$

Equation (2.7) indicates that, in the steady-state, the maximized DFIG generated power is proportional to the cube of the wind speed.

The direct component of the rotor current,  $i_{rd}$ , may be used to control the stator reactive power  $Q_s$ . This is possible based on

$$Q_s = -\frac{3}{2} \frac{v_{sm}^2}{(1 + \sigma_s)L_m\omega_0} - \frac{3}{2} \frac{1}{(1 + \sigma_s)} v_{sm} i_{rd}, \quad (2.8)$$

where  $L_m$  is the DFIG magnetizing inductance.  $i_{rd}$  and  $i_{rq}$  can be independently controlled by a current-control scheme [30], such that they track their respective reference commands according to the transfer functions

$$\frac{I_{rd}(s)}{I_{rdref}(s)} = \frac{I_{rq}(s)}{I_{rqref}(s)} = \frac{1}{\tau_1 s + 1}, \quad (2.9)$$

where  $\tau_1$  is the time-constant of the closed current-control loop.  $i_{rqref}$  is calculated based on (2.5). Based on (2.8),  $i_{rdref}$  can be set based on the desired value of  $Q_s$ . In this thesis  $i_{rdref}$  is set to such a (constant) value that  $Q_s + Q_f = 0$  if  $v_{sm}$  and  $\omega_0$  have their respective nominal values.

#### 2.4.2 Grid Side Real/Reactive Power Control Scheme

In the WPSU, the real- and reactive-power components  $P_c$  and  $Q_c$  (subscript  $c$  signifies “converter”) are controlled by the GSC. In the grid-connected mode of operation, the control of  $P_c$  may be employed to manage the battery State-of-Charge (SOC), to regulate the delivered real power, or to maintain the dc-link voltage  $v_{dc}$  if the battery fails or it is disconnected from the dc link. In the islanded mode of operation, however,  $P_c$  is controlled to regulate the frequency of the (islanded) network. In either mode, i.e. the grid-connected or the islanded,  $Q_c$  is controlled to regulate the PCC voltage amplitude, i.e.  $v_{sm}$ .

Fig. 2.1(a) shows that the control is exercised in a  $dq$  frame that is synchronized to  $v_{s-abc}$  through a phase-locked loop (PLL). Therefore,  $P_c$  and  $Q_c$  are, respectively, proportional to and can be controlled by the direct and quadrature current components  $i_{cd}$  and  $i_{cq}$ , as

$$P_c = \frac{3}{2}v_{sm}i_{cd}, \quad (2.10)$$

$$Q_c = -\frac{3}{2}v_{sm}i_{cq}, \quad (2.11)$$

In turn,  $i_{cd}$  and  $i_{cq}$  can be independently controlled by current-control scheme [31], such that they track their respective reference commands  $i_{cdref}$  and  $i_{cqref}$ , according to the transfer functions

$$\frac{I_{cd}(s)}{I_{cdref}(s)} = \frac{I_{cq}(s)}{I_{cqref}(s)} = \frac{1}{\tau_2 s + 1}, \quad (2.12)$$

where the time-constant  $\tau_2$  can be made reasonably small by proper selection of the controller parameters. Based on (2.10) and (2.11)  $i_{cdref}$  and  $i_{cqref}$  are, respectively, calculated from the real- and reactive-power reference commands,  $P_{cref}$  and  $Q_{cref}$ , as

$$i_{cdref} = \frac{2}{3v_{sm}}P_{cref}, \quad (2.13)$$

$$i_{cqref} = \frac{2}{3v_{sm}}Q_{cref}. \quad (2.14)$$

$P_{cref}$  and  $Q_{cref}$  are determined by the real- and reactive-power management schemes as described in Section 2.5.

## 2.5 Real- and Reactive-Power Management Schemes

The power management process consists of the real-power management and the reactive-power management, to generate the reference commands  $P_{cref}$  and  $Q_{cref}$ , respectively. These are explained in the subsections 2.5.1 and 2.5.2.

### 2.5.1 Real-Power Management Scheme

Fig. 2.2 illustrates a block diagram of the real-power management scheme of the WPSU. Fig. 2.2 shows that  $P_{cref}$ , i.e. the output of the real-power management scheme, is composed of the output of the dc-link voltage regulation scheme, i.e.  $P_{reg}$ , the output of the real-power/frequency droop function, i.e.  $P_{droop}$ , and the battery power command  $P_{b-ref}$ . The following subsections elaborate on each component of  $P_{cref}$ .

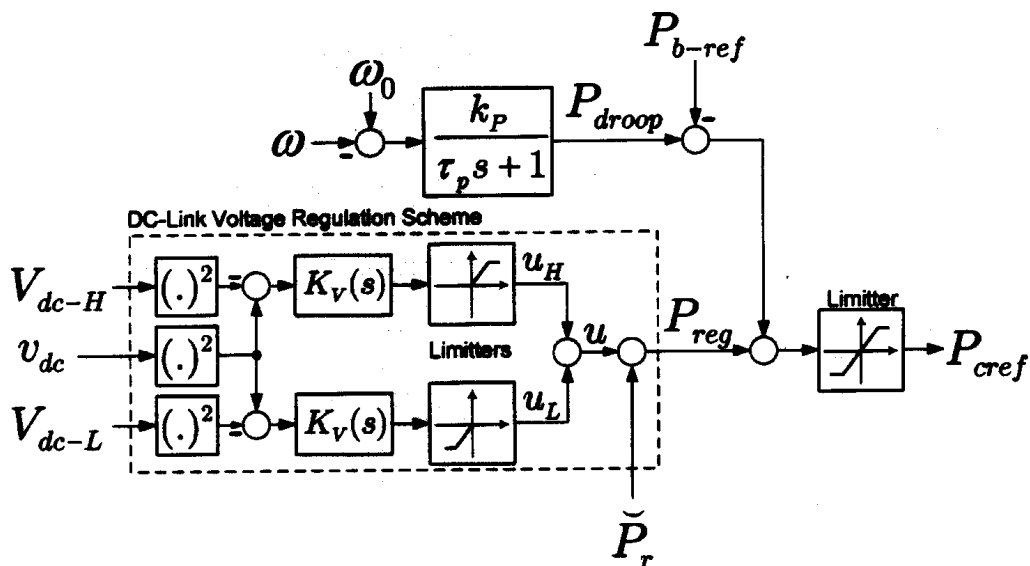


Fig. 2.2: Block diagram of the real-power management scheme

### 2.5.1.1 DC-link Voltage Regulation Scheme

The outlined area of Fig. 2.2 illustrates the block diagram of the dc-link voltage regulation scheme, whose function is to maintain the dc-link voltage in the grid-connected mode of operation. This scheme enables the WPSU to operate without a battery in the grid-connected mode, that is, the same way that a conventional wind-power unit operates. In addition, if the WPSU has a functioning battery, the dc-link voltage regulation scheme provides protection against dc-link voltage runaway, in case the battery fails to function properly, for example, due to maintenance, failure, or conductor rapture. To maintain  $v_{dc}$  within an acceptable range, the regulation scheme controls  $P_{cref}$  (and thus  $P_c$ ) through its output  $P_{reg}$ . Dynamics of  $v_{dc}$  are described by the power balance equation

$$\left(\frac{C_L}{2}\right) \frac{dv_{dc}^2}{dt} \approx P_r - P_c, \quad (2.15)$$

where  $P_r$  and  $P_c$  act as the disturbance and the control inputs, respectively. Fig. 2.2 shows that  $P_{reg}$  is the superposition of the control signal  $u$  and a measure of the rotor power  $P_r$ , denoted by  $\check{P}_r$ .  $u$ , in turn, is the superposition of the outputs of two compensators: The first compensator processes the error  $v_{dc}^2 - V_{dc-H}^2$  and delivers the output  $u_H$ , only if  $v_{dc}$  exceeds the maximum permissible level  $V_{dc-H}$ ; the second compensator processes the error  $v_{dc}^2 - V_{dc-L}^2$  and stipulates  $u_L$ , only if  $v_{dc}$  drops lower than the minimum permissible level  $V_{dc-L}$ . Thus,  $u = u_H + u_L$  assumes a nonzero value only if the battery voltage is lower than  $V_{dc-L}$  or higher than  $V_{dc-H}$ ;  $u$  settles at zero if  $V_{dc-L} < v_{dc} < V_{dc-H}$ , i.e. if the dc-link voltage is impressed by

the battery. Based on this regulation strategy, the battery voltage is permitted to vary between  $V_{dc-L}$  and  $V_{dc-H}$ , depending on its SOC.  $\check{P}_r$  acts as a feed-forward signal and ensures that  $u$  takes a typically small steady-state value, corresponding to the power loss of the GSC, when the battery is out of service.

Fig. 2.3 illustrates a control block diagram of the dc-link voltage regulation scheme, corresponding to the range  $v_{dc} \in \{(0, V_{dc-L}) \cup (V_{dc-H}, +\infty)\}$ . It is observed that  $P_{b-ref}$  and  $P_r$  act as the disturbance inputs to the control loop. In the control block diagram of Fig. 2.3, the reference command  $V_{dc-ref}$  is

$$V_{dc-ref} = \begin{cases} V_{dc-L} & \text{if } v_{dc} \leq V_{dc-L} \\ V_{dc-H} & \text{if } v_{dc} \geq V_{dc-H} \end{cases}$$

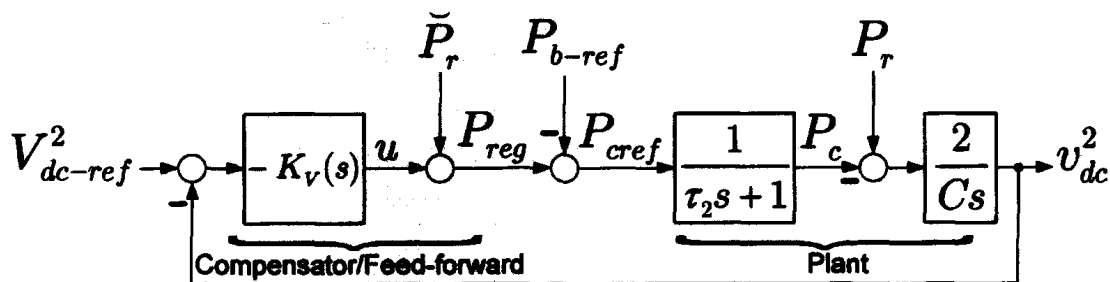


Fig. 2.3: Block diagram of the dc-link voltage regulation scheme

In addition, Fig. 2.3 shows that the control plant consists of series connection of a first-order transfer function and an integrator. For such a control plant the compensator  $K_V(s)$  can be readily designed using the method of “symmetrical optimum” [30]. It should be noted that  $\omega = \omega_0$  in the grid-connected mode of operation. Therefore,  $P_{droop}$  is zero and does not appear in Fig. 2.3.

### 2.5.1.2 Frequency Regulation Scheme

Fig. 2.3 also shows that  $P_{droop}$  and  $P_{b-ref}$  are the two other components of  $P_{cref}$ .  $P_{droop}$  is the output of a first-order filter whose input is the frequency error  $\omega_0 - \omega$  in which  $\omega$  is the network (actual) frequency. The droop filter has a dc gain of  $k_p$  and a time-constant of  $\tau_p$ .

In the grid-connected mode of operation,  $\omega = \omega_0$  and thus  $P_{droop} = 0$ . Hence, as understood from Fig. 2.3,  $P_{cref} = -P_{b-ref} + \check{P}_r + u$ . If  $v_{dc}$  is impressed by the battery, that is  $V_{dc-L} < v_{dc} < V_{dc-H}$ , then  $u = 0$  and

$$\underbrace{P_{cref}}_{\approx P_c} = -P_{b-ref} + \underbrace{\check{P}_r}_{\approx P_r} \quad (2.16)$$

As Fig. 2.1 illustrates,  $P_b = P_r - P_c$ . Therefore, based on (2.16), one deduces

$$P_b = P_r - P_c \approx P_{b-ref} \quad (2.17)$$

Equation (2.17) indicates that, in the grid-connected mode of operation the battery power is controlled by the reference command  $P_{b-ref}$  which can be determined in two distinct ways; (i) if  $P_{b-ref}$  is set in such a way that  $P_{b-ref} = P_e - P_{tref}(t)$ , where  $P_{tref}(t)$  is a desired profile for the delivered real power, then  $P_t$  tracks the desired profile; (ii) alternatively,  $P_{b-ref}$  can be calculated based on a desired battery current profile, through a battery charging algorithm. It should be noted that, irrespective of the method adopted for the calculation of  $P_{b-ref}$ , i.e. (i) or (ii) above,  $P_b$  tracks  $P_{b-ref}$  only if  $V_{dc-L} < v_{dc} < V_{dc-H}$ ; once  $v_{dc}$  approaches either  $V_{dc-L}$  or  $V_{dc-H}$ , the dc-link voltage regulation scheme (see Fig. 2.2 ) reacts,  $u$  assumes a

non-zero value that, due to the integral action of  $K_V(s)$ , overrides  $P_{b-ref}$ , and  $v_{dc}$  stops drifting. Hence, based on the proposed control strategy, in the grid-connected mode the battery can neither get overcharged nor overly discharged. In the islanded mode of operation, however, there will likely be a mismatch between the net power generation and consumption within the distribution network. Consequently, the network frequency  $\omega$  deviates from its nominal value  $\omega_0$ , if no corrective control is exercised. In this case, the balance of power is regained by correction of the delivered real power, i.e.  $P_t$ . This objective is fulfilled, indirectly, by adjustment of  $P_{cref}$  through the command  $P_{droop}$  and based on the frequency error  $\omega_0 - \omega$ , Fig. 2.2. Thus,  $P_c$  rises (drops) as the frequency drops (rises), until the power is balanced again and a new operating frequency is reached.

### 2.5.2 Reactive-Power Management Scheme

Fig. 2.4 illustrates a block diagram of the reactive-power management scheme of the WPSU. Fig. 2.4 shows that  $Q_{cref}$  is the superposition of the command  $Q_{dis-ref}$  and the reactive-power/voltage droop signal  $Q_{droop}$ . As shown in Fig. 2.4,  $Q_{droop}$  is the output of a first-order filter whose input is the voltage magnitude error  $V_{sm-ref} - v_{sm}$ , where  $V_{sm-ref}$  and  $v_{sm}$  are the nominal and actual peak values of  $v_{s-abc}(t)$ , respectively. The droop filter has a dc gain of  $k_Q$  and a time-constant of  $\tau_Q$ .

In case that the WPSU is connected to a stiff grid,  $v_{s-abc}$  is dictated and  $v_{sm}$  is close to  $V_{sm-ref}$ . Hence,  $Q_{droop}$  is small and  $Q_{cref} \approx Q_{dis-ref}$ . Thus,  $Q_{dis-ref}$  can be used to control the power-factor that the WPSU exhibits

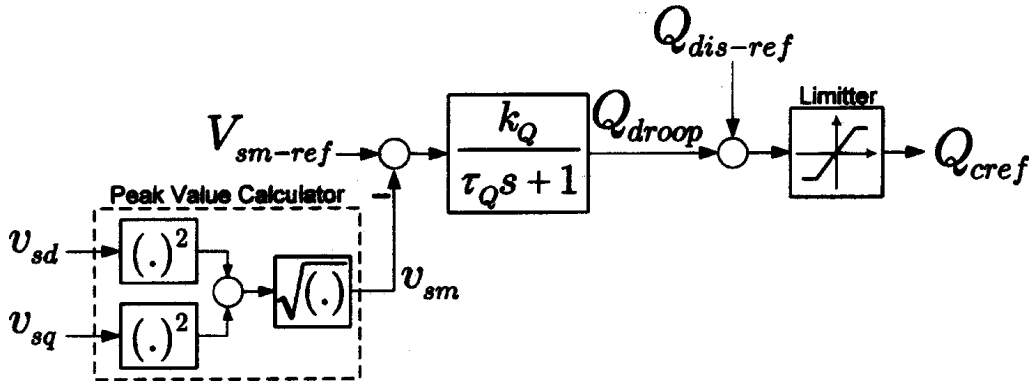


Fig. 2.4: Block diagram of the reactive-power management scheme

to the power system. Alternately, if the WPSU is interfaced with a non-stiff grid, deviations of  $v_{sm}$  from  $V_{sm-ref}$  result in changes in  $Q_{droop}$  and consequently in  $Q_{cref}$ , based on the error  $V_{sm-ref} - v_{sm}$ ; this brings  $v_{sm}$  back to a vicinity of  $V_{sm-ref}$ . In the islanded mode of operation, the regulation of  $v_{sm}$  is totally handled by the droop mechanism.

### 2.5.3 Pitch-Angle Control Scheme

In the grid-connected mode of operation, the pitch-angle control can be employed to limit either the delivered real power (in case that  $P_b$  is imposed) or the battery power (in case that  $P_t$  is imposed), if the wind speed exceeds its rated value, e.g. 12 m/s; for wind speeds lower than the rated value, the pitch-angle controller maintains the pitch angle at zero, and the DFIG generated power retains its maximum value expressed by (2.7). In the islanded mode of operation, if the wind speed is high while the network load is small, the pitch-angle controller increases the pitch angle to prevent the battery from getting overcharged.

## 2.6 Simulation Results

To evaluate the effectiveness of the proposed control strategy, simulation studies are performed on a detailed switched model of the system of Fig. 2.1, in the PSCAD/EMTDC software environment. The capacities of the WPSU and the CSU are 1.67 MVA and 400 kVA, respectively; the rated wind speed for both wind power units is 12 m/s and the air density is assumed to be  $\rho = 1.225 \text{ kg/m}^3$ . For most simulations, constant wind speeds subject to stepwise changes are employed as test signals, except for Case 4 and Case 6 in which a more realistic profile of the wind speed has been used [32]. The system parameters are given in Appendix A. In addition, Table A.6, Appendix A, provides the base values for per-unitized variables.

### *A. Case 1: startup response and regulation of the delivered real power*

Initially, the wind speed is 6.0 m/s, the WPSU is connected to the grid, and the DFIG is magnetized through its stator. In addition, the motor load is energized through  $B_2$ , whereas the  $R-L$  load and the CSU are disconnected. Furthermore, the controllers are disabled, the gating pulses of the RSC and the GSC are blocked, and both  $B_r$  and  $B_b$  are open. However,  $B_c$  is closed and the dc-link capacitor is charged to about 1.0 kV, through the antiparallel diodes of the GSC.

At  $t = 0.25 \text{ s}$ , the controllers of GSC are enabled and the gating pulses are unblocked. Thus, as shown in Fig. 2.5(a), the reference commands  $V_{dc-L}$  and  $V_{dc-H}$  are ramped up to 1250 V and 1450 V, respectively, and  $v_{dc}$  rises. Once  $V_{dc-L} < v_{dc} < V_{dc-H}$ , the dc-link voltage regulation scheme

stops the control process and, therefore,  $v_{dc}$  may vary within the limits  $V_{dc-L}$  and  $V_{dc-H}$ , as shown in Fig. 2.5(a).

The control system keeps  $B_r$  open for as long as  $\omega_r$  is lower than about  $0.65 pu$ . Consequently, subsequent to the start-up, the DFIG rotor current and torque are zero. However, the turbine torque is nonzero due to the presence of wind and  $\omega_r$  increases, as illustrated by the dashed line in Fig. 2.5(b). At  $t = 0.57 s$ ,  $\omega_r$  reaches the threshold of about  $0.65 pu$  and a logic mechanism is triggered to close  $B_r$ , to activate the controllers of the RSC, and to unblock the gating pulses of the RSC. Thus, the DFIG torque,  $T_e$ , assumes a nonzero value according to (2.1), and the rate-of-change of  $\omega_r$  decreases, Fig. 2.5(b). At  $t = 0.9 s$  the wind speed changes from  $6.0 m/s$  to  $9.0 m/s$ , and  $\omega_r$  increases towards a new equilibrium of  $0.97 pu$ .

The solid line in Fig. 2.5(b) illustrates that the DFIG generated power,  $P_e$ , is zero from start-up to up until  $t = 0.57 s$ , since  $T_e$  is zero. At  $t = 0.57 s$ , however,  $T_e$  assumes a nonzero value and  $P_e$  increases to about  $0.12 pu$ . This results in a disturbance in the dc-link voltage, Fig. 2.5(a). From  $t = 0.57 s$  on,  $P_e$  changes proportional to the cube of the rotor speed, based on (2.6).

At  $t = 1.0 s$ ,  $B_b$  is closed. Consequently, the dc-link voltage is impressed by the battery and becomes equal to  $1350 V$ , Fig. 2.5(a). At  $t = 1.2 s$ ,  $P_{b-ref}$  is changed from zero to  $P_{b-ref} = P_e - 0.59 pu$ . The solid line in Fig. 2.5(c) illustrates that  $P_t$  rises rapidly and settles at about  $0.57 pu$  which, due to power losses, is slightly lower than  $0.59 pu$ . Fig. 2.5(c) also shows that from  $t = 0$  to  $1.2 s$ ,  $P_t$  is almost equal to  $P_e$ , excepts at  $t = 0$  and  $t = 0.25 s$

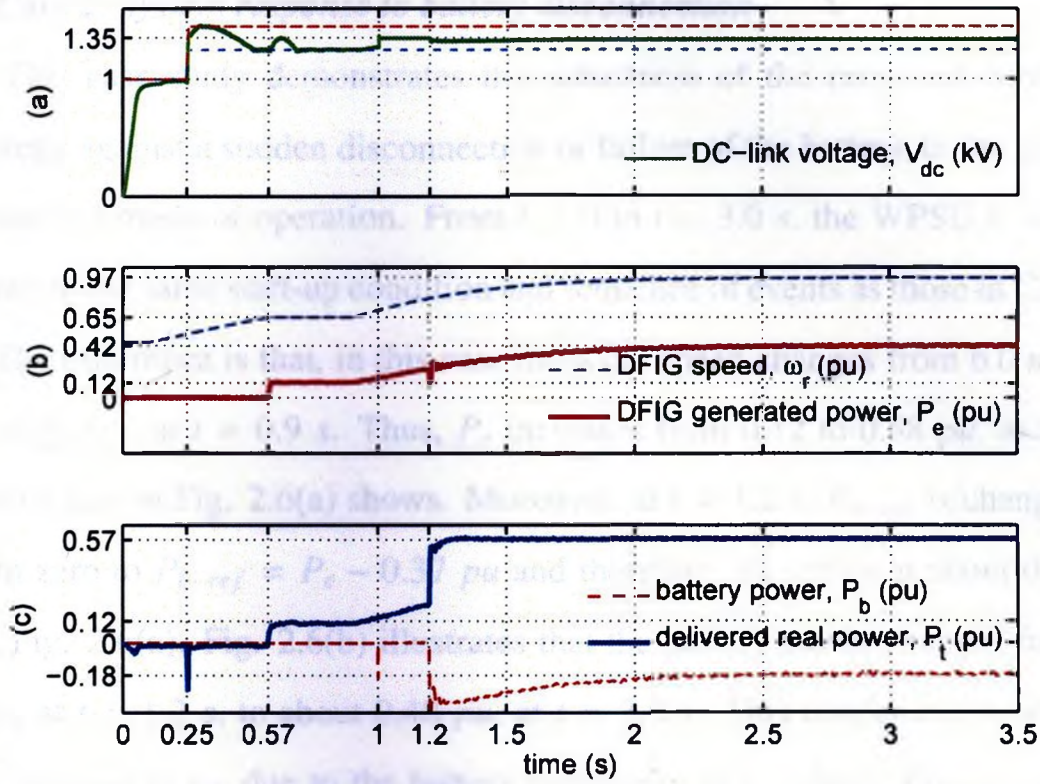


Fig. 2.5: Case1: waveforms of (a) dc-link voltage. (b) DFIG speed and generated power, and (c) battery power and DFIG delivered real power

when  $P_t$  exhibits negative spikes. The first spike corresponds to the dc-link capacitor pre-charging process through the GSC diodes, whereas the second spike is due to the power drawn from the grid, to force  $v_{dc}$  to track  $V_{dc-L}$ .

The dashed line in Fig. 2.5(c) illustrates that the battery power,  $P_b$ , is zero until  $t = 1.2$  s. However, from  $t = 1.2$  s on,  $P_b$  becomes negative to regulate  $P_t$  at 0.57 pu. Fig. 2.5(c) also shows that  $P_b$  exhibits a negative spike at  $t = 1.0$  s. This spike corresponds to the power that flows from the battery to the dc-link capacitor when  $B_b$  gets closed, to push  $v_{dc}$  from 1250 V up to the battery voltage of 1350 V.

### ***B. Case 2: system response to battery disconnection***

This case study demonstrates the robustness of the proposed control strategy against a sudden disconnection or failure of the battery, in the grid-connected mode of operation. From  $t = 0$  to  $t = 3.0$  s, the WPSU is subjected to the same start-up condition and sequence of events as those in Case 1. The difference is that, in this case the wind speed changes from  $6.0$  m/s to  $11.5$  m/s, at  $t = 0.9$  s. Thus,  $P_e$  increases from  $0.12$  to  $0.88$  pu, as the dashed line in Fig. 2.6(a) shows. Moreover, at  $t = 1.2$  s,  $P_{b-ref}$  is changed from zero to  $P_{b-ref} = P_e - 0.37$  pu and therefore,  $P_t$  settles at about  $0.37$  pu, Fig. 2.6(a). Fig. 2.6(b) illustrates that the battery power changes from zero, at  $t = 1.2$  s, to about  $0.48$  pu, at  $t = 3.0$  s. This results in a moderate increase in  $v_{dc}$  due to the battery resistance, Fig. 2.6(c). Figs. 2.6(d) and 2.6(a) show that  $P_c$  takes an opposite pattern of variations as that of  $P_e$ , since  $P_t$  is constant.

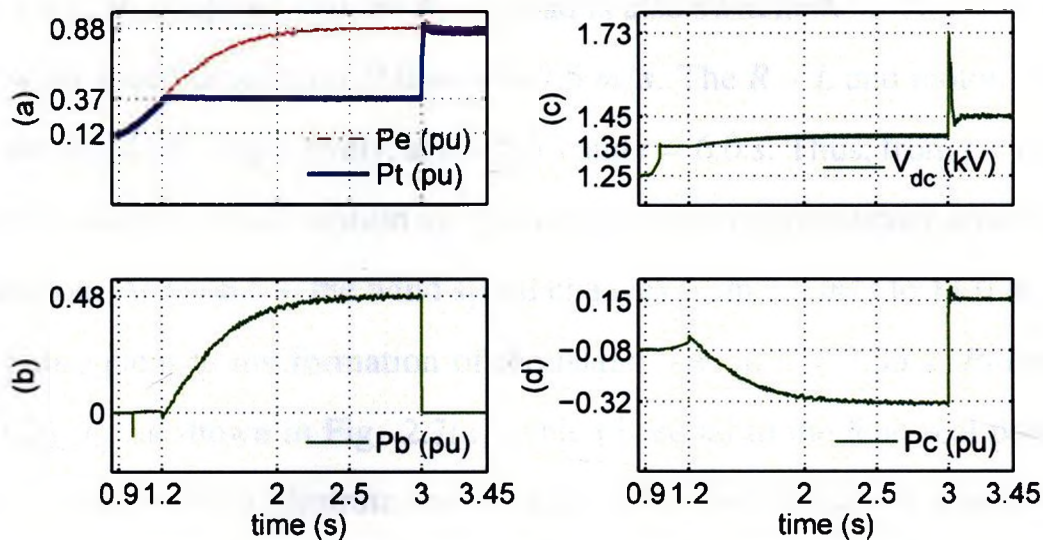


**Fig. 2.6:** Case2: waveforms of (a) DFIG generated and delivered real powers, (b) battery power, (c) dc-link voltage, and (d) GSC real power

At  $t = 3.0$  s,  $B_b$  opens and the battery is disconnected from the dc-link. Consequently,  $P_t$  becomes equal to  $P_e$ , as shown in Fig. 2.6(a), and  $P_b$  drops to zero, Fig. 2.6(b). The difference between  $P_r$  and  $P_c$  is thus delivered to the dc-link capacitor and results in an overshoot of about 20% in  $v_{dc}$ , Fig. 2.6(c). Once  $v_{dc}$  exceeds  $V_{dc-H}$ , the dc-link voltage regulation scheme increases  $P_c$ , as illustrated in Fig. 2.6(d), such that the overshoot is damped in about 10 ms and  $v_{dc}$  settles at  $V_{dc-H}$  ( $= 1450$  V), Fig. 2.6(c).

### C. Case 3: islanded operation

In this case study, the WPSU is initially in the grid-connected mode and the same steady-state condition as that of Case 1 at  $t = 3.5$  s. Thus, the motor-load is energized whereas the  $R - L$  load and the constant-speed wind-power unit are disconnected from the PCC. At  $t = 3.55$  s,  $B_g$  opens and the remote electrification system is isolated from the power system. At

$t = 4.0$  s,  $B_1$  is closed and the  $R - L$  load is also switched on. At  $t = 4.5$  s, the wind speed drops from  $9.0$  m/s to  $7.5$  m/s. The  $R - L$  and motor loads are switched off, respectively, at  $t = 5.5$  s and  $t = 6.0$  s. Thus, from  $t = 6.0$  s on, the islanded electrification system continues to operate under a no-load condition. At  $t = 6.5$  s, the wind speed changes from  $7.5$  m/s to  $11.0$  m/s.

Subsequent to the formation of the island, i.e. at  $t = 3.55$  s,  $P_t$  drops to  $0.26$  pu, as shown in Fig. 2.7(a), which is equal to the load real power. Figs. 2.7(b) and (c) illustrate that  $\omega_r$  and  $P_e$  become disturbed subsequent to each load switching incident, but the system remains stable by and large. The short-term excursions of  $\omega_r$  and  $P_e$  are due to the disturbances on the DFIG stator voltage (not shown), caused by the loads switching incidents. The long-term excursions of  $\omega_r$  and  $P_e$  are, however, due to the wind speed changes at  $t = 4.5$  s and  $t = 6.5$  s.

Fig. 2.7(d) illustrates the behavior of  $P_c$ , as enforced by the droop mechanism of Fig. 2.2, in response to the real power mismatch. Fig. 2.7(e) indicates that the network frequency  $\omega$  increases as the load power drops, and vice versa. After  $t = 6.0$  s, no load remains present within the island. This scenario represents a difficult operational condition for the frequency regulation scheme. However, as Fig. 2.7(e) shows,  $\omega$  settles at about  $1.034$  pu, and the balance of power is maintained by the battery, Fig. 2.7(f). It is to be noted that, due to the proportional nature of the droop-based control strategy, the frequency cannot be regulated to exact  $1.0$  pu, unless the frequency set-point is also adjusted. Without such adjustment of the set-point, the regulation can be improved if larger droop gains are used. This may, however,

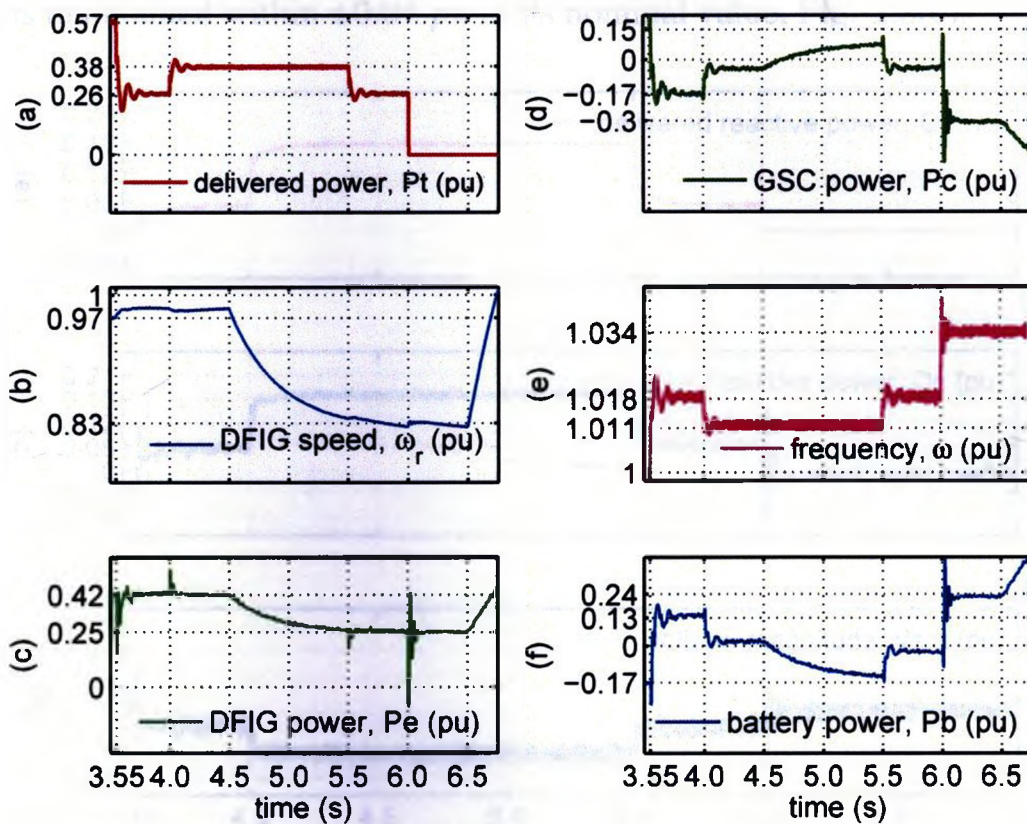


Fig. 2.7: Case3: waveforms of (a) delivered real power, (b) DFIG speed, (c) DFIG generated power, (d) GSC real power, (e) frequency, and (f) battery power

subject the control to instability issues. Another option is to avoid excessive generation surplus by introduction of dump loads, or to avoid excessive power shortage by load shedding.

Figs. 2.8(a) to (c) illustrate the responses of  $Q_t$ ,  $Q_c$ , and  $v_{sm}$ , respectively. Fig. 2.8(a) shows that prior to the islanding event,  $Q_t$  is about  $-0.07$  pu, i.e. the WPSU operates at near unity power-factor. However, subsequent to the islanding incident,  $Q_t$  becomes equal to the load reactive power. From  $t = 4.0$  s to  $t = 5.5$  s,  $Q_t$  is maximum as the  $R-L$  load demands a relatively large reactive power. However, at  $t = 6.0$  s  $Q_t$  drops to zero when both loads are switched off. Thus, the droop mechanism adjusts  $Q_c$ . Fig. 2.8(b), and

$v_{sm}$  is maintained within  $\pm 0.04$  pu of its nominal value, Fig. 2.8(c).

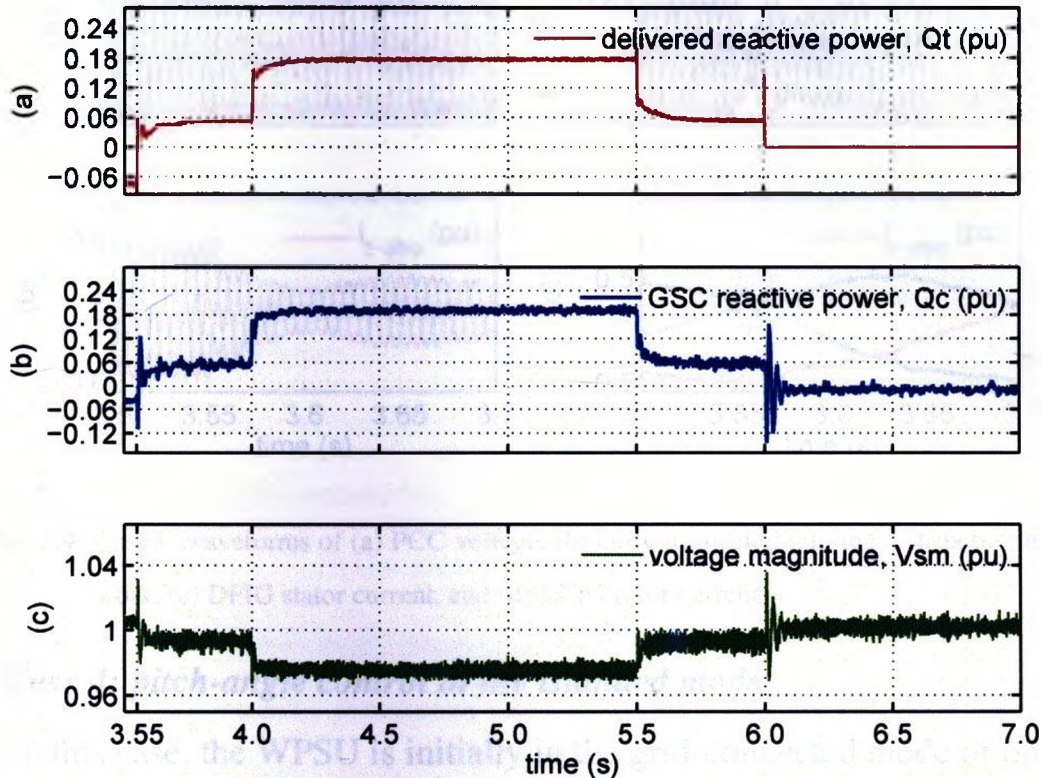


Fig. 2.8: Case3: waveforms of (a) delivered reactive power, (b) GSC reactive power, and (c) PCC voltage magnitude

Fig. 2.9 provides a close-up of the responses of the PCC voltage, the current injected into the distribution network by the WPSU, and the DFIG stator and rotor currents, at about the islanding instant. Fig. 2.9(a) shows that the PCC voltage remains sinusoidal with a relatively constant amplitude. This is in spite of the severe disturbance in  $i_{t-abc}$ , Fig. 2.9(b). Figs. 2.9(c) and (d) illustrate that both the stator and rotor currents become distorted subsequent to the islanding moment. However, they resume their pre-disturbance qualities in less than three 60-Hz cycles.

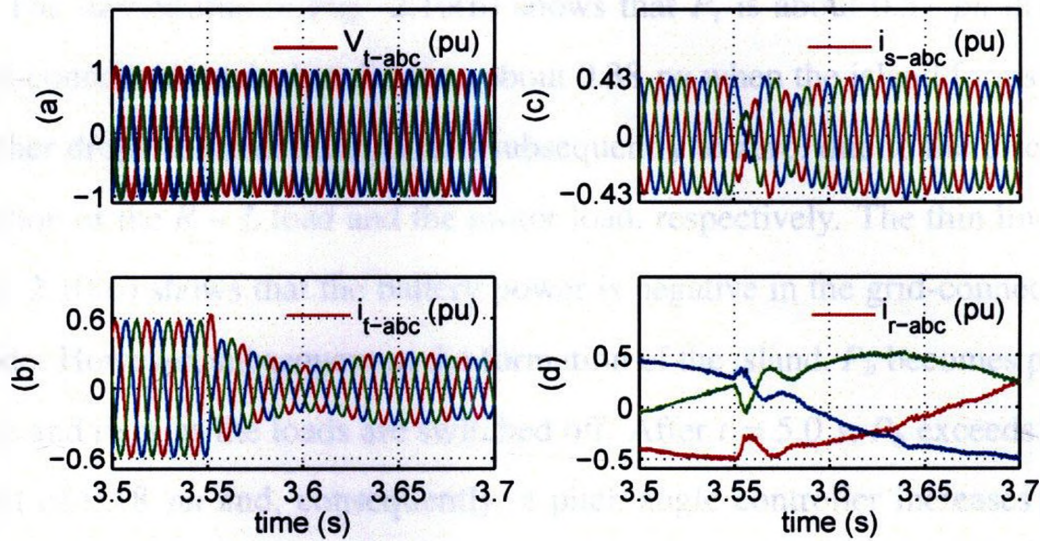
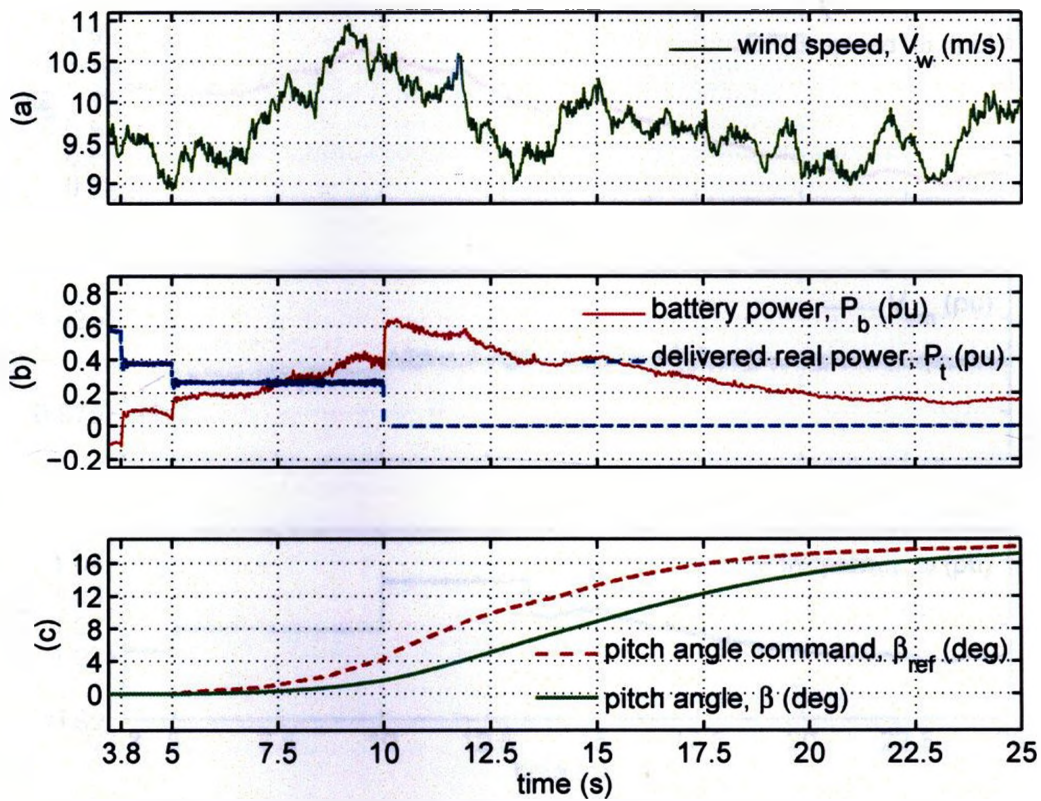


Fig. 2.9: Case3: waveforms of (a) PCC voltage, (b) current injected into the distribution network, (c) DFIG stator current, and (d) DFIG rotor current

#### D. Case 4: pitch-angle control in the islanded mode

In this case, the WPSU is initially in the grid-connected mode of operation and subject to the wind-speed waveform shown in Fig. 2.10(a). In addition, the CSU is disconnected from the PCC, whereas the  $R-L$  and motor loads are energized. The battery power command is set to  $P_{b-ref} = P_e - 0.59 pu$ , while the maximum permissible battery power is specified as  $0.18 pu$ . At  $t = 3.8 s$ , the breaker  $B_g$  opens and the WPSU and the local loads form an island. At  $t = 5.0 s$  the  $R-L$  load is turned off. At  $t = 10 s$  the motor load is also turned off and the islanded electrification system continues to operate under the no-load condition. Figs. 2.10 and 2.11 illustrate the system response to the disturbances.

The dashed line in Fig. 2.10(b) shows that  $P_t$  is about  $0.57 pu$  in the grid-connected mode, but drops to about  $0.38 pu$  when the island forms.  $P_t$  further drops to about  $0.26 pu$  and subsequently to zero, due to the disconnection of the  $R - L$  load and the motor load, respectively. The thin line in Fig. 2.10(b) shows that the battery power is negative in the grid-connected mode. However, subsequent to the formation of the island,  $P_b$  becomes positive and rises as the loads are switched off. After  $t = 5.0 s$ ,  $P_b$  exceeds the limit of  $0.18 pu$  and, consequently, a pitch-angle controller increases the pitch-angle reference command. Thus, the pitch-angle tracks the command and settles at about  $17^\circ$ , in the steady state, as shown in Fig. 2.10(c). The result is that  $P_b$  is limited to about  $0.18 pu$ , Fig. 2.10(b), subject to a transient during which the battery power exceeds  $0.18 pu$ . This is due to the sluggish nature of the mechanical pitch-angle control mechanism; if not permitted by the temporary overcharge characteristic of the battery, this transient period can be avoided by rapid introduction of electrical dump loads.



**Fig. 2.10:** Case4: waveforms of (a) wind speed, (b) battery power and delivered real power, and (c) pitch angle

Fig. 2.11(a) indicates that the system remains stable and  $\omega_r$  is limited to 1.2 pu. Fig. 2.11(b) and (c) illustrate that the network voltage and frequency are regulated, respectively, within 2.5% and 3.4% of their corresponding nominal values.

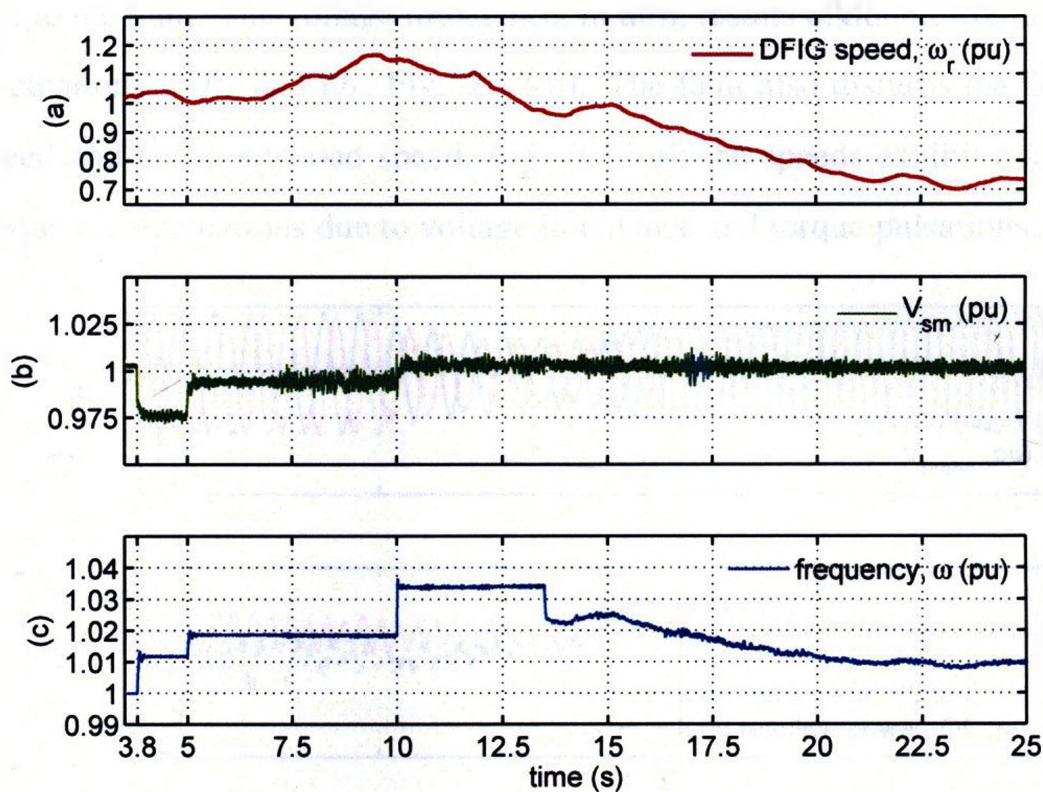


Fig. 2.11: Case4: waveforms of (a) DFIG speed, (b) PCC voltage magnitude, and (c) frequency

### E. Case 5: system response to a line-to-ground fault

In this case, the WPSU is in the grid-connected mode, the wind-speed is  $9.0 \text{ m/s}$ , and  $\omega_r = 0.97 \text{ pu}$ . The battery power command  $P_{b-ref}$  is set to zero and thus  $P_t = P_e = 0.88 \text{ pu}$ . The motor load is energized and draws the real and reactive powers of  $P_L = 0.25 \text{ pu}$  and  $Q_L = 0.05 \text{ pu}$ , respectively. However, the  $R - L$  load and the CSU are not connected to the network. At  $t = 3.7 \text{ s}$ , one phase of the PCC is shorted to the ground, though an impedance of  $0.0033j \text{ pu}$ . Consequently,  $B_g$  opens at  $t = 3.8 \text{ s}$  and the electrification system gets isolated from the power system while the fault is still present.

Fig. 2.12(a) shows that the PCC voltage,  $v_{t-abc}$ , becomes unbalanced

due to the fault. The voltage imbalance, in turn, results in double-frequency fluctuations in  $P_L$  and  $Q_L$ , Fig. 2.12(b). The fault also disturbs the DFIG speed and the motor load speed, Fig. 2.12(c); the speeds exhibit double-frequency fluctuations due to voltage imbalance and torque pulsations.

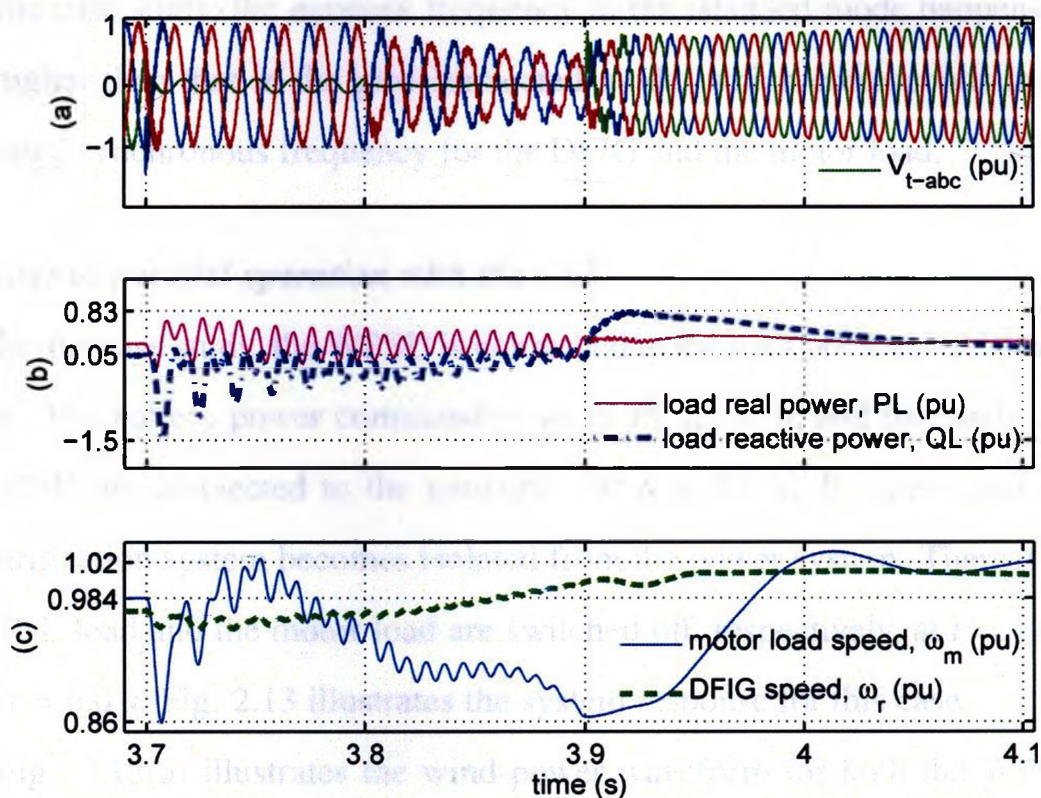


**Fig. 2.12:** Case5: waveforms of (a) PCC voltage, (b) load real and reactive powers, and (c) motor load and DFIG speeds

At  $t = 3.9$  s, the fault is cleared while  $B_g$  remains open, and the system continues to operate in the islanded mode. Fig. 2.12(a) indicates that the WPSU recovers from the fault and  $v_{t-abc}$  retrieves its pre-fault balanced form. Fig. 2.12(a) also shows that subsequent to the fault clearance, the amplitude of  $v_{t-abc}$  increases smoothly, in 7 cycles, and settles at about 1.0 pu. Once the voltage is balanced, the double-frequency fluctuations of  $P_L$

and  $Q_L$  vanish as Fig. 2.12(b) shows. Fig. 2.12(c) shows that subsequent to the fault clearance, the DFIG speed and the motor load speed increase and settle at slightly higher respective steady-state values than those in the pre-fault condition. The reason is that, given the load/generation condition of this case study, the network frequency in the islanded mode happens to be higher than that in the grid-connected mode, which corresponds to an elevated synchronous frequency for the DFIG and the motor load.

#### ***F. Case 6: parallel operation with the CSU***

In this case study, the WPSU is connected to the network and in a steady state. The battery power command is set to  $P_{b-ref} = 0$ , and the loads and the CSU are connected to the network. At  $t = 2.0$  s,  $B_g$  opens and the electrification system becomes isolated from the power system. Thereafter, the R-L load and the motor load are switched off, respectively, at  $t = 4.0$  s and  $t = 6.0$  s. Fig. 2.13 illustrates the system response for this case.

Fig. 2.13(a) illustrates the wind-power waveform for both the WPSU and the CSU. Figs. 2.13(b) and (c), respectively, illustrate the powers generated of the WPSU and CSU. Fig. 2.13(d) shows that subsequent to the islanding incident, the battery power changes from zero to about  $-0.15$  pu, corresponding to flow of power from the battery to the distribution network. However, as the  $R - L$  load is turned off, the battery power becomes smaller in absolute value. At  $t = 6.0$  s, i.e. when motor load is also switched off,  $P_b$  becomes positive and the battery totally absorbs the power generated by both the DFIG and the CSU. Figs. 2.13(e) and (f) indicate that the network

frequency and voltage are regulated and the electrification system remains stable.

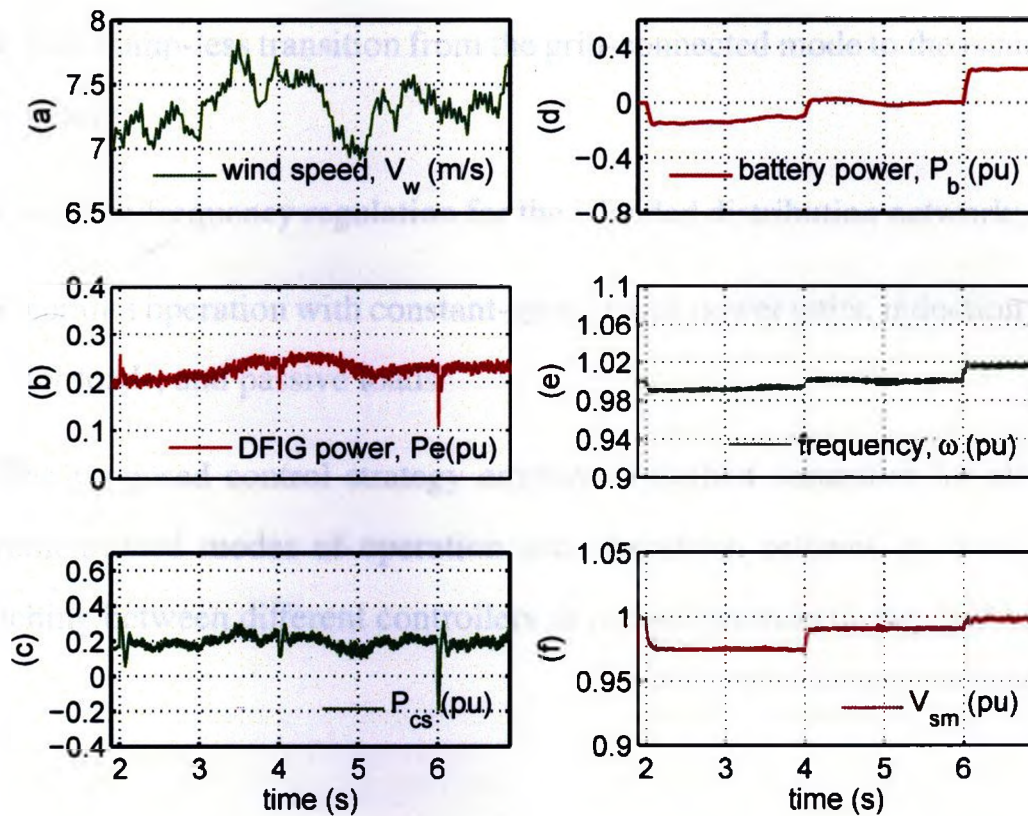


Fig. 2.13: Case6: system responses in the islanded mode, under parallel operation of the WPSU and the CSU

## 2.7 Summary

A multi-mode control strategy is proposed for the WPSU. Under the proposed control strategy the WPSU can operate in the grid-connected mode and preserves the characteristics of a conventional grid-connected DFIG-based wind-power unit, in addition to the capabilities featured in the literature for a wind-power unit that is augmented with battery energy storage.

If a DFIG-based wind-power unit is equipped with a battery, the proposed control strategy also enables islanded operation and the following features:

- fast, bump-less transition from the grid-connected mode to the islanded mode;
- voltage/frequency regulation for the islanded distribution network; and
- parallel operation with constant-speed wind-power units, induction motor loads, and passive loads.

The proposed control strategy employs a unified controller for all the aforementioned modes of operation and, therefore, relieves the need for switching between different controllers or reconfiguration of the hardware.

## **Chapter 3**

# **Stability Analysis of the Wind-Power and Storage Unit (WPSU)**

### **3.1 Introduction**

Chapter 2 developed a control strategy for the WPSU, based on a nonlinear set of equations. Then, the performance of the WPSU was evaluated under the developed control strategy, for different operating conditions in the islanding and grid-connected modes of operation. The simulation studies employed in Chapter 2, although accurate, do not provide an adequate insight into the stability or robustness of the proposed control strategy, in a systematic sense. The analysis reported in this chapter attempts to fill this gap. Thus, this chapter presents a small-signal, linear, model for the WPSU, expressed in the state-space form, on which an eigenvalue analysis can be conducted.

### 3.2 Linearization of a Nonlinear System

To develop a linear model for the WPSU, its describing large-signal, nonlinear, equations are linearized around an operating point of interest. The procedures to derive the large-signal equations are complicated and, therefore, not reported in this thesis. However, they can be found in references [30] and [33]. Thus, this chapter starts its analysis from the equations themselves, which are listed in Appendix B.

Consider the following generic state-space representation of a nonlinear system which has  $n$  state variables,  $m$  inputs, and  $l$  outputs:

$$\begin{aligned}\dot{\mathbf{x}} &= \mathbf{f}(\mathbf{x}, \mathbf{u}), \\ \mathbf{y} &= \mathbf{g}(\mathbf{x}, \mathbf{u}),\end{aligned}\tag{3.1}$$

where  $\mathbf{x}$  is the vector of state variables,  $\mathbf{u}$  is the vector of control and/or disturbance inputs, and  $\mathbf{y}$  is the vector of outputs.  $\mathbf{f}(\cdot, \cdot)$  and  $\mathbf{g}(\cdot, \cdot)$  are the vectors of state- and output functions, respectively:

$$\mathbf{f} = \begin{bmatrix} f_1(\cdot, \cdot, \cdot, \cdot, \cdot) \\ f_2(\cdot, \cdot, \cdot, \cdot, \cdot) \\ \cdot \\ \cdot \\ f_n(\cdot, \cdot, \cdot, \cdot, \cdot) \end{bmatrix}\tag{3.2}$$

$$\mathbf{g} = \begin{bmatrix} g_1(\cdot, \cdot, \cdot, \cdot, \cdot) \\ g_2(\cdot, \cdot, \cdot, \cdot, \cdot) \\ \cdot \\ \cdot \\ g_l(\cdot, \cdot, \cdot, \cdot, \cdot) \end{bmatrix} \quad (3.3)$$

In (3.2) and (3.3), the entries  $f_i$  and  $g_i$  are, in general, nonlinear functions of their arguments.

A steady-state operating point is then described by

$$\begin{aligned} \mathbf{0} &= \mathbf{f}(\mathbf{x}_0, \mathbf{u}_0), \\ \mathbf{y}_0 &= \mathbf{g}(\mathbf{x}_0, \mathbf{u}_0), \end{aligned} \quad (3.4)$$

where  $\mathbf{x}_0$  and  $\mathbf{u}_0$  are the constant state-variable and input vectors, corresponding to the operating point. Now, assume that the inputs and the state variables are perturbed about  $\mathbf{u}_0$  and  $\mathbf{x}_0$ , as

$$\begin{aligned} \mathbf{u} &= \mathbf{u}_0 + \tilde{\mathbf{u}} \\ \mathbf{x} &= \mathbf{x}_0 + \tilde{\mathbf{x}} \end{aligned} \quad (3.5)$$

Then, (3.1) can be rewritten as

$$\begin{aligned} \dot{\mathbf{x}} &= \mathbf{0} + \dot{\tilde{\mathbf{x}}} = \mathbf{f}[(\mathbf{x}_0 + \tilde{\mathbf{x}}), (\mathbf{u}_0 + \tilde{\mathbf{u}})] \\ \mathbf{y} &= \mathbf{y}_0 + \tilde{\mathbf{y}} = \mathbf{g}[(\mathbf{x}_0 + \tilde{\mathbf{x}}), (\mathbf{u}_0 + \tilde{\mathbf{u}})] \end{aligned} \quad (3.6)$$

Assuming that the perturbations are small, the right-hand sides of (3.6) can be approximated by a Taylor's series. Hence

$$\begin{aligned}\dot{\tilde{\mathbf{x}}} &= \mathbf{f}[(\mathbf{x}_0 + \tilde{\mathbf{x}}), (\mathbf{u}_0 + \tilde{\mathbf{u}})] \\ &= \mathbf{f}(\mathbf{x}_0, \mathbf{u}_0) + \left. \frac{\partial \mathbf{f}}{\partial \mathbf{x}} \right|_{u_0, x_0} \tilde{\mathbf{x}} + \left. \frac{\partial \mathbf{f}}{\partial \mathbf{u}} \right|_{u_0, x_0} \tilde{\mathbf{u}} + \dots, \end{aligned} \quad (3.7)$$

$$\begin{aligned}\mathbf{y}_0 + \tilde{\mathbf{y}} &= \mathbf{g}[(\mathbf{x}_0 + \tilde{\mathbf{x}}), (\mathbf{u}_0 + \tilde{\mathbf{u}})] \\ &= \mathbf{g}(\mathbf{x}_0, \mathbf{u}_0) + \left. \frac{\partial \mathbf{g}}{\partial \mathbf{x}} \right|_{u_0, x_0} \tilde{\mathbf{x}} + \left. \frac{\partial \mathbf{g}}{\partial \mathbf{u}} \right|_{u_0, x_0} \tilde{\mathbf{u}} + \dots, \end{aligned} \quad (3.8)$$

Noting that  $\mathbf{0} = \mathbf{f}(\mathbf{x}_0, \mathbf{u}_0)$  and  $\mathbf{y}_0 = \mathbf{g}(\mathbf{x}_0, \mathbf{u}_0)$ , and keeping only the first-order perturbed terms in (3.7) and (3.8), one obtains

$$\begin{aligned}\dot{\tilde{\mathbf{x}}} &= \mathbf{A}\tilde{\mathbf{x}} + \mathbf{B}\tilde{\mathbf{u}} \\ \tilde{\mathbf{y}} &= \mathbf{C}\tilde{\mathbf{x}} + \mathbf{D}\tilde{\mathbf{u}}, \end{aligned} \quad (3.9)$$

where

$$\mathbf{A}_{n \times n} = \frac{\partial \mathbf{f}}{\partial \mathbf{x}} = \begin{bmatrix} \frac{\partial f_1}{\partial x_1} & \dots & \frac{\partial f_1}{\partial x_n} \\ \dots & \dots & \dots \\ \frac{\partial f_n}{\partial x_1} & \dots & \frac{\partial f_n}{\partial x_n} \end{bmatrix} \quad (3.10)$$

$$\mathbf{B}_{n \times m} = \frac{\partial \mathbf{f}}{\partial \mathbf{u}} = \begin{bmatrix} \frac{\partial f_1}{\partial u_1} & \dots & \frac{\partial f_1}{\partial u_m} \\ \dots & \dots & \dots \\ \frac{\partial f_n}{\partial u_1} & \dots & \frac{\partial f_n}{\partial u_m} \end{bmatrix} \quad (3.11)$$

$$\mathbf{C}_{l \times n} = \frac{\partial \mathbf{g}}{\partial \mathbf{x}} = \begin{bmatrix} \frac{\partial g_1}{\partial x_1} & \cdots & \frac{\partial g_1}{\partial x_n} \\ \cdots & \cdots & \cdots \\ \frac{\partial g_l}{\partial x_1} & \cdots & \frac{\partial g_l}{\partial x_n} \end{bmatrix} \quad (3.12)$$

$$\mathbf{D}_{l \times m} = \frac{\partial \mathbf{g}}{\partial \mathbf{u}} = \begin{bmatrix} \frac{\partial g_1}{\partial u_1} & \cdots & \frac{\partial g_1}{\partial u_m} \\ \cdots & \cdots & \cdots \\ \frac{\partial g_l}{\partial u_1} & \cdots & \frac{\partial g_l}{\partial u_m} \end{bmatrix} \quad (3.13)$$

Equation (3.9) represents a small-signal linear model of the original non-linear system, i.e. (3.1), expressed in the classical state-space form.

### 3.3 Small-Signal Model of WPSU

For the purpose of an eigenvalue analysis, to manage the equations more efficiently, the WPSU is divided into four subsystems. These are (1) the DFIG subsystem, (2) the PLL subsystem, (3) the capacitor subsystem, and (4) the grid-side converter (GSC) subsystem. Then, each subsystem is linearized based on the procedure explained above, and a linear state-space representation of the WPSU is constructed. These steps are presented in the following subsections.

#### 3.3.1 Linearized Model of the DFIG Subsystem

The DFIG subsystem is described by Equations (B.1) through (B.7), Equation (B.16), and Equation (B.17). They can be written in the state-space

form

$$\begin{aligned}\dot{\mathbf{x}}_{dfig} &= \mathbf{f}_{dfig}(\mathbf{x}_{dfig}, \mathbf{u}_{dfig}) \\ \mathbf{y}_{dfig} &= \mathbf{g}_{dfig}(\mathbf{x}_{dfig}, \mathbf{u}_{dfig})\end{aligned}\quad (3.14)$$

where

$$\mathbf{x}_{dfig} = \left[ \hat{\lambda}_s \quad \delta \quad \omega_r \quad \xi_d \quad \xi_q \quad i_{rd} \quad i_{rq} \right]^T \quad (3.15)$$

$$\mathbf{u}_{dfig} = \left[ \omega \quad v_{sd} \quad v_{sq} \right]^T \quad (3.16)$$

Based on the linearization process of Section 3.2, these equations constitute the following linear state-space equations:

$$\dot{\tilde{\mathbf{x}}}_{dfig} = \mathbf{A}_{dfig} \tilde{\mathbf{x}}_{dfig} + \mathbf{B}_{dfig1} \begin{bmatrix} \tilde{v}_{sd} \\ \tilde{v}_{sq} \end{bmatrix} + \mathbf{B}_{dfig2} \tilde{\omega} \quad (3.17)$$

$$\begin{bmatrix} \tilde{i}_{sd} \\ \tilde{i}_{sq} \end{bmatrix} = \mathbf{C}_{dfig} \tilde{\mathbf{x}}_{dfig} \quad (3.18)$$

where  $\tilde{v}_{sd}$ ,  $\tilde{v}_{sq}$ , and  $\tilde{\omega}$  are the inputs to the DFIG subsystem and are obtained from the capacitor subsystem and the PLL subsystem; the DFIG subsystem outputs are  $\tilde{i}_{sd}$  and  $\tilde{i}_{sq}$ .

### 3.3.2 Linearized Model of the PLL Subsystem

The PLL subsystem is described by Equations (B.18) through (B.23), which can be expressed in the form

$$\begin{aligned}\dot{\mathbf{x}}_{pll} &= \mathbf{f}_{pll}(\mathbf{x}_{pll}, \mathbf{u}_{pll}) \\ \mathbf{y}_{pll} &= \mathbf{g}_{pll}(\mathbf{x}_{pll}, \mathbf{u}_{pll})\end{aligned}\tag{3.19}$$

where

$$\mathbf{x}_{pll} = \left[ \xi_{pll} \quad \xi_{pll1} \quad \xi_{pll2} \quad \xi_{pll3} \quad \xi_{pll4} \right]^T\tag{3.20}$$

$$\mathbf{u}_{pll} = v_{sq}\tag{3.21}$$

Thus, the linear state-space representation is

$$\dot{\tilde{\mathbf{x}}}_{pll} = \mathbf{A}_{pll}\tilde{\mathbf{x}}_{pll} + \mathbf{B}_{pll}\tilde{v}_{sq}\tag{3.22}$$

$$\tilde{\omega} = \mathbf{C}_{pll}\tilde{\mathbf{x}}_{pll}\tag{3.23}$$

$\tilde{v}_{sq}$  is the input of the PLL subsystem and is obtained from the capacitor subsystem. The output of the PLL subsystem is  $\tilde{\omega}$ .

### 3.3.3 Linearized Model of the Capacitor Subsystem

The capacitor subsystem is characterized by Equations (B.24) and (B.25), of which the state-space representation is

$$\begin{aligned}\dot{\mathbf{x}}_{cap} &= \mathbf{f}_{cap}(\mathbf{x}_{cap}, \mathbf{u}_{cap}) \\ \mathbf{y}_{cap} &= \mathbf{g}_{cap}(\mathbf{x}_{cap}, \mathbf{u}_{cap})\end{aligned}\tag{3.24}$$

where

$$\mathbf{x}_{cap} = \begin{bmatrix} v_{sd} & v_{sq} \end{bmatrix}^T \quad (3.25)$$

$$\mathbf{u}_{cap} = \begin{bmatrix} i_{cd} & i_{cq} & i_{sd} & i_{sq} & i_{td} & i_{tq} \end{bmatrix}^T \quad (3.26)$$

The linear state-space form can be written as

$$\dot{\tilde{\mathbf{x}}}_{cap} = \mathbf{A}_{cap} \tilde{\mathbf{x}}_{cap} + \mathbf{B}_{cap1} \begin{bmatrix} \tilde{i}_{cd} \\ \tilde{i}_{cq} \end{bmatrix} + \mathbf{B}_{cap2} \begin{bmatrix} \tilde{i}_{sd} \\ \tilde{i}_{sq} \end{bmatrix} + \mathbf{B}_{cap3} \begin{bmatrix} \tilde{i}_{td} \\ \tilde{i}_{tq} \end{bmatrix} + \mathbf{B}_{cap4} \tilde{\mathbf{u}} \quad (3.27)$$

$$\begin{bmatrix} \tilde{v}_{sd} \\ \tilde{v}_{sq} \end{bmatrix} = \mathbf{C}_{cap} \tilde{\mathbf{x}}_{cap} \quad (3.28)$$

As (3.27) indicates,  $\tilde{i}_{cd}$ ,  $\tilde{i}_{cq}$ ,  $\tilde{i}_{sd}$ ,  $\tilde{i}_{sq}$ ,  $\tilde{i}_{td}$ , and  $\tilde{i}_{tq}$  are the inputs to the capacitor subsystem;  $\tilde{i}_{cd}$  and  $\tilde{i}_{cq}$  are obtained from the GSC subsystem, whereas  $\tilde{i}_{sd}$  and  $\tilde{i}_{sq}$  are obtained from the DFIG subsystem.  $\tilde{i}_{td}$  and  $\tilde{i}_{tq}$  are the outputs of the load subsystem and considered as disturbance inputs. Equation (3.28) indicates that  $\tilde{v}_{sd}$  and  $\tilde{v}_{sq}$  are the outputs of the capacitor subsystem.

### 3.3.4 Linearized Model of the GSC Subsystem

Equations (B.26) through (B.29) describe the GSC subsystem which also embeds the droop functions. In the state-space form, these equations are written as

$$\begin{aligned} \dot{\mathbf{x}}_{gsc} &= \mathbf{f}_{gsc}(\mathbf{x}_{gsc}, \mathbf{u}_{gsc}) \\ \mathbf{y}_{gsc} &= \mathbf{g}_{gsc}(\mathbf{x}_{gsc}, \mathbf{u}_{gsc}) \end{aligned} \quad (3.29)$$

where

$$\mathbf{x}_{gsc} = \begin{bmatrix} i_{cd} & i_{cq} & i_{cdref} & i_{cqref} \end{bmatrix}^T \quad (3.30)$$

$$\mathbf{u}_{gsc} = \begin{bmatrix} \omega & v_{sd} \end{bmatrix}^T \quad (3.31)$$

The linear counterparts are

$$\dot{\tilde{\mathbf{x}}}_{gsc} = \mathbf{A}_{gsc}\tilde{\mathbf{x}}_{gsc} + \mathbf{B}_{gsc1}\tilde{\omega} + \mathbf{B}_{gsc2}\tilde{v}_{sd} \quad (3.32)$$

$$\begin{bmatrix} \tilde{i}_{cd} \\ \tilde{i}_{cq} \end{bmatrix} = \mathbf{C}_{gsc}\tilde{\mathbf{x}}_{gsc} \quad (3.33)$$

where  $\tilde{\omega}$  and  $\tilde{v}_{sd}$  are the two inputs of the GSC subsystem and obtained, respectively, from the PLL subsystem and the capacitor subsystem.  $\tilde{i}_{cd}$  and  $\tilde{i}_{cq}$  are the outputs of the GSC subsystem.

### 3.3.5 Overall Linearized Model

The four subsystems described in Sections 3.3.1 through 3.3.4 can be combined to form a linear state-space model for the WPSU. This is done by substituting for the output(s) of a subsystem in the relevant input(s) of another subsystem. The result is:

$$\dot{\tilde{\mathbf{x}}}_{wpsu} = \underbrace{\begin{bmatrix} \mathbf{A}_{dfig} & \mathbf{B}_{dfig2}\mathbf{C}_{pll} & \mathbf{B}_{dfig1}\mathbf{C}_{cap} & \mathbf{0} \\ \mathbf{0} & \mathbf{A}_{pll} & \mathbf{B}_{pll-cap}\mathbf{C}_{cap} & \mathbf{0} \\ \mathbf{B}_{cap2}\mathbf{C}_{dfig} & \mathbf{B}_{cap4}\mathbf{C}_{pll} & \mathbf{A}_{cap} & \mathbf{B}_{cap1}\mathbf{C}_{gsc} \\ \mathbf{0} & \mathbf{B}_{gsc1}\mathbf{C}_{pll} & \mathbf{B}_{gsc-cap}\mathbf{C}_{cap} & \mathbf{A}_{gsc} \end{bmatrix}}_{\mathbf{A}_{wpsu}} \tilde{\mathbf{x}}_{wpsu} + \mathbf{B}_{wpsu}\mathbf{u}_{wpsu} \quad (3.34)$$

where,

$$\tilde{\mathbf{x}}_{wpsu} = \left[ \tilde{\mathbf{x}}_{dfig}^T \quad \tilde{\mathbf{x}}_{pll}^T \quad \tilde{\mathbf{x}}_{cap}^T \quad \tilde{\mathbf{x}}_{gsc}^T \right]^T \quad (3.35)$$

$$\mathbf{B}_{wpsu} = \left[ \mathbf{0} \quad \mathbf{0} \quad \mathbf{B}_{cap3} \quad \mathbf{0} \right]^T \quad (3.36)$$

$$\tilde{\mathbf{u}}_{wpsu} = \left[ \tilde{i}_{td} \quad \tilde{i}_{tq} \right]^T \quad (3.37)$$

$$\mathbf{B}_{pll-cap} = \left[ \mathbf{0}_{5 \times 1} \quad \mathbf{B}_{pll} \right] \quad (3.38)$$

$$\mathbf{B}_{gsc-cap} = \left[ \mathbf{B}_{gsc2} \quad \mathbf{0}_{4 \times 1} \right] \quad (3.39)$$

The output(s) of interest can be computed by

$$\mathbf{y}_{wpsu} = \mathbf{C}_{wpsu} \tilde{\mathbf{x}}_{wpsu} \quad (3.40)$$

where  $\mathbf{C}_{wpsu}$  is a suitable output matrix.

Equations (3.34) through (3.40) describe the WPSU of Fig. 2.1(a), with the current components  $\tilde{i}_{td}$  and  $\tilde{i}_{tq}$  as the inputs. The WPSU has 18 state variables contributed by the DFIG subsystem (7 state variables), the PLL subsystem (5 state variable), the capacitor subsystem (2 state variables), and the GSC subsystem (4 state variables). Therefore, there also exist 18 eigenvalues and corresponding eigenmodes, which are influenced by different system parameters and operating conditions. However, as long as the system stability is concerned, dominant eigenvalues and their sensitivities to the parameters and operating conditions are of paramount importance; the other eigenvalues primarily affect the system performance, but not the stability. These issues are discussed in more detail in the next section.

### 3.4 Stability of the WPSU

Based on the linear model of the WPSU, represented by (3.34) through (3.40), a relatively large number of tests have been conducted to characterize the impact of different parameters/operating-points on the dominant eigenvalues; in this chapter, only a few of them are reported, for the sake of conciseness.

Table 3.1 includes the eigenvalues of the WPSU, i.e. the solutions to  $|A_{wpsu} - \lambda_i I| = 0$  ( $i = 1, 2, \dots, 18$ ), for different wind speeds. The results are obtained for the no-load condition, that is,  $i_{td} = \tilde{i}_{td} = 0$  and  $i_{tq} = \tilde{i}_{tq} = 0$ . The eigenvalues, some in conjugate pairs, are indexed from 1 to 18. Table 3.1 identifies three eigenvalues as the dominant one; these are  $\lambda_{18}$  and the pair  $\lambda_{11,12}$ . As Table 3.1 indicates,  $\lambda_{18}$  is pulled further to the left of the  $j\omega$  axis as the wind speed increases. By contrast,  $\lambda_{11,12}$  move towards the Right-Half-Plane (RHP) with the increase of the wind speed. This trend results in two corresponding unstable eigenmodes at the wind speed of 20  $m/s$ . The other eigenvalues are all on the Left-Half-Plane (LHP), relatively fixed in their loci, and quite far from the  $j\omega$  axis. Therefore, their movements do not pose any instability issues. It should be pointed out that, for wind speeds larger than 12  $m/s$  the pitch-angle mechanism of the WPSU takes effect to limit the generated power. This means that the WPSU has a different model than (3.34) through (3.40) for such a range of wind speed. Consequently, the eigenvalues corresponding to the wind speed of 20  $m/s$  in Table 3.1 are included just for demonstrating the trend, and will not take place in reality.

**Table 3.1:** Eigenvalues of the WPSU for Different Wind Speeds

Eigenvalues of $A_{wpsu}$											
$V_w$	$\lambda_{1,2}$	$\lambda_{3,4}$	$\lambda_{5,6}$	$\lambda_7$	$\lambda_8$	$\lambda_{9,10}$	$\lambda_{11,12}$	$\lambda_{13,14}$	$\lambda_{15}$	$\lambda_{16,17}$	$\lambda_{18}$
6 m/s	$-171 \pm$ 6180j	$-195 \pm$ 5424j	$-1044 \pm$ 656j	-519	-492	$-130 \pm$ 319j	$-3.7 \pm$ 68j	$-49 \pm$ 60j	-21	$-18.8 \pm$ 13.4j	-1.8
9 m/s	$-166 \pm$ 6189j	$-188 \pm$ 5418j	$-1053 \pm$ 632j	-520	-492	$-131 \pm$ 325j	$-3.4 \pm$ 66j	$-50 \pm$ 60j	-21	$-18.7 \pm$ 13.6j	-2.8
12 m/s	$-158 \pm$ 6201j	$-179 \pm$ 5411j	$-1066 \pm$ 599j	-522	-493	$-132 \pm$ 332j	$-2.8 \pm$ 64j	$-52 \pm$ 57j	-21	$-18.6 \pm$ 13.9j	-3.7
20 m/s	$-126 \pm$ 6247j	$-141 \pm$ 5384j	$-1120 \pm$ 430j	-493	-531	$-138 \pm$ 363j	<b>1.4</b> $\pm$ <b>62j</b>	$-61 \pm$ 37j	-21	$-17.9 \pm$ 15.8j	-6.2

### 3.5 Robustness of the WPSU

The WPSU consists of four, highly interconnected, subsystems. Thus, identification of the parameters that significantly impact the dominant eigenvalues is a difficult task. The “*Participation Factor*” analysis provides a relatively effective way to circumvent the above-mentioned difficulty. A participation factor provides a relative measure of the manifestation of a particular eigenmode, for example, the one corresponding to a dominant eigenvalue, in a given state variable. This, indirectly, helps to identify the parameters that have remarkable influence on the dominant eigenvalue and thus on the stability of the WPSU.

Table 3.2 lists the state-variables of all subsystems of the WPSU, and participation factors of each state-variable in the eigenmodes corresponding to the 18 eigenvalues. In Table 3.2, the participation factor of a state-variable  $\tilde{x}_l$ ,  $l = 1, 2, \dots, 18$ , in an eigenmode corresponding to an eigenvalue  $\lambda_m$  has

been calculated from [34]– [35]:

$$p_{lm} = \mathbf{v}_m^l \mathbf{u}_m^l \quad (3.41)$$

where  $\mathbf{u}_m^l$  and  $\mathbf{v}_m^l$  are the  $l^{\text{th}}$  elements of the vectors  $\mathbf{u}_m$  and  $\mathbf{v}_m$ , respectively.  $\mathbf{u}_m$  and  $\mathbf{v}_m$  are, respectively, the right eigenvectors of  $\mathbf{A}_{wpsu}$  and  $\mathbf{A}_{wpsu}^T$ , corresponding to the eigenvalue  $\lambda_m$ . In general,  $p_{lm} = a + jb$  is a complex number. However, here the relative participation of a state-variable in an eigenmode is of prime importance. Hence, in Table 3.2 the norm  $\|p_{lm}\| = \sqrt{a^2 + b^2}$  is reported rather than  $p_{lm}$ . The values are rounded off to the thousandths place, with any value smaller than 0.001 denoted by “ $\approx 0$ ”.

The analysis of Section 3.4 identified the pair  $\lambda_{11,12}$  as the (dominant) critical eigenvalues which tend to destabilize the WPSU. Tables 3.2 and 3.3 indicate that the state variables  $\tilde{\lambda}_s$ ,  $\tilde{\xi}_d$ ,  $\tilde{\xi}_{pll}$ , and  $\tilde{i}_{cq}$  actively participate in the eigenmode(s) corresponding to  $\lambda_{11,12}$ . Therefore, it is expected that the controllers related to the foregoing state variables exhibit appreciable impacts on  $\lambda_{11,12}$ . These controllers are (i) the DFIG torque-control scheme, (ii) the PLL filter, and (iii) the reactive-power management scheme, shown in Fig. 2.4.

**Table 3.2:** WPSU State Variables and Their Participation Factors (Wind Speed=9.0 m/s.)

Eigenvalues and State Participation Factors of the Subsystems of WPSU												
Sub-system	States	$\lambda_{1,2}$	$\lambda_{3,4}$	$\lambda_{5,6}$	$\lambda_7$	$\lambda_8$	$\lambda_{9,10}$	$\lambda_{11,12}$	$\lambda_{13,14}$	$\lambda_{15}$	$\lambda_{16,17}$	$\lambda_{18}$
		$-166 \pm 6189j$	$-188 \pm 5418j$	$-1053 \pm 632j$	-	-	$-131 \pm 325j$	$-3.4 \pm 66j$	$-50 \pm 60j$	-21	$-18.7 \pm 13.6j$	-2.8
DFIG	$\tilde{\lambda}_s$	0.022	0.008	$\approx 0$	0.002	0.007	$\approx 0$	<b>0.476</b>	0.004	0.035	0.001	0.0
	$\tilde{\delta}$	0.019	0.025	0.196	0.011	0.005	0.436	0.028	0.511	$\approx 0$	0.048	0.0
	$\tilde{\omega}_r$	0.0	0.0	0.0	$\approx 0$	0.0	$\approx 0$	0.001	0.005	0.0	0.048	1.040
	$\tilde{\xi}_d$	0.0	$\approx 0$	$\approx 0$	$\approx 0$	0.001	0.002	<b>0.139</b>	0.007	0.934	$\approx 0$	$\approx 0$
	$\tilde{\xi}_q$	0.0	$\approx 0$	$\approx 0$	0.003	$\approx 0$	0.002	0.001	0.074	0.003	0.845	0.049
	$\tilde{i}_{rd}$	0.229	0.257	0.045	0.020	0.046	0.026	0.083	0.006	0.056	0.0	0.0
	$\tilde{i}_{rq}$	0.231	0.270	0.012	0.106	0.011	0.039	$\approx 0$	0.062	$\approx 0$	0.066	0.001
PLL	$\tilde{\xi}_{pll}$	0.0	0.0	$\approx 0$	0.0	0.0	0.032	<b>0.734</b>	$\approx 0$	0.077	$\approx 0$	$\approx 0$
	$\tilde{\xi}_{pll1}$	0.0	0.0	0.065	0.033	0.002	0.434	0.002	0.380	0.0	0.013	0.0
	$\tilde{\xi}_{pll2}$	0.0	0.0	0.497	0.085	0.004	1.003	$\approx 0$	0.062	$\approx 0$	$\approx 0$	0.0
	$\tilde{\xi}_{pll3}$	$\approx 0$	$\approx 0$	1.407	0.069	0.003	0.339	0.0	0.004	0.0	0.0	0.0
	$\tilde{\xi}_{pll4}$	0.002	0.002	1.251	0.018	$\approx 0$	0.057	0.0	$\approx 0$	0.0	0.0	0.0
Capacitor	$\tilde{v}_{sd}$	0.248	0.253	$\approx 0$	$\approx 0$	0.0	$\approx 0$	$\approx 0$	$\approx 0$	0.0	0.0	0.0
	$\tilde{v}_{sq}$	0.254	0.249	0.007	0.0	0.0	0.002	$\approx 0$	$\approx 0$	0.0	0.0	0.0
GSC	$\tilde{i}_{cd}$	$\approx 0$	$\approx 0$	0.010	0.038	0.002	0.043	0.004	0.211	0.002	0.773	0.007
	$\tilde{i}_{cq}$	$\approx 0$	0.001	$\approx 0$	0.006	0.014	0.002	<b>0.460</b>	0.025	0.089	0.003	0.0
	$\tilde{i}_{cdref}$	$\approx 0$	$\approx 0$	0.014	0.952	0.109	0.030	$\approx 0$	0.033	0.0	0.024	$\approx 0$
	$\tilde{i}_{cqref}$	$\approx 0$	0.001	$\approx 0$	0.139	0.854	0.001	0.061	0.004	0.002	$\approx 0$	0.0

**Table 3.3:** WPSU State Variables and Their Participation Factors (Wind Speed=12.0 m/s.)

Eigenvalues and State Participation Factors of the Subsystems of WPSU												
Sub-system	States	$\lambda_{1,2}$	$\lambda_{3,4}$	$\lambda_{5,6}$	$\lambda_7$	$\lambda_8$	$\lambda_{9,10}$	$\lambda_{11,12}$	$\lambda_{13,14}$	$\lambda_{15}$	$\lambda_{16,17}$	$\lambda_{18}$
		$-158 \pm 6201j$	$-179 \pm 5411j$	$-1066 \pm 599j$	-	-	$-132 \pm 332j$	$-2.8 \pm 64j$	$-52 \pm 57j$	-21	$-18.6 \pm 13.9j$	-3.7
DFIG	$\tilde{\lambda}_s$	0.022	0.008	0.001	0.002	0.007	0.002	<b>0.471</b>	0.010	0.035	0.001	0.0
	$\tilde{\delta}$	0.026	0.037	0.191	0.015	0.004	0.428	0.031	0.498	$\approx 0$	0.049	0.0
	$\tilde{\omega}_r$	0.0	0.0	0.0	$\approx 0$	0.0	$\approx 0$	0.002	0.005	0.0	0.069	1.053
	$\tilde{\xi}_d$	0.0	$\approx 0$	$\approx 0$	$\approx 0$	0.001	0.002	<b>0.132</b>	0.015	0.930	0.004	0.001
	$\tilde{\xi}_q$	0.0	$\approx 0$	$\approx 0$	0.003	$\approx 0$	0.002	0.001	0.073	0.006	0.850	0.066
	$\tilde{i}_{rd}$	0.231	0.257	0.087	0.020	0.045	0.044	0.075	0.012	0.056	$\approx 0$	0.0
	$\tilde{i}_{rq}$	0.229	0.272	0.014	0.112	0.010	0.039	0.001	0.061	$\approx 0$	0.069	0.001
PLL	$\tilde{\xi}_{pll}$	0.0	0.0	$\approx 0$	0.0	0.030	0.013	<b>0.734</b>	$\approx 0$	0.075	$\approx 0$	$\approx 0$
	$\tilde{\xi}_{pll1}$	0.0	0.0	0.071	0.038	0.001	0.428	0.004	0.398	0.0	0.012	0.0
	$\tilde{\xi}_{pll2}$	0.0	$\approx 0$	0.538	0.096	0.003	1.006	0.001	0.058	0.0	$\approx 0$	0.0
	$\tilde{\xi}_{pll3}$	$\approx 0$	$\approx 0$	1.486	0.079	0.002	0.350	$\approx 0$	0.004	0.0	0.0	0.0
	$\tilde{\xi}_{pll4}$	0.003	0.004	1.319	0.021	$\approx 0$	0.060	0.0	$\approx 0$	0.0	0.0	0.0
Capacitor	$\tilde{v}_{sd}$	0.246	0.255	$\approx 0$	$\approx 0$	0.0	$\approx 0$	$\approx 0$	$\approx 0$	0.0	0.0	0.0
	$\tilde{v}_{sq}$	0.256	0.247	0.006	0.0	0.0	0.002	$\approx 0$	$\approx 0$	0.0	0.0	0.0
GSC	$\tilde{i}_{cd}$	$\approx 0$	$\approx 0$	0.011	0.043	0.001	0.042	0.006	0.201	0.006	0.785	0.010
	$\tilde{i}_{cq}$	$\approx 0$	0.001	$\approx 0$	0.005	0.014	0.002	<b>0.440</b>	0.045	0.093	0.010	$\approx 0$
	$\tilde{i}_{cdref}$	$\approx 0$	$\approx 0$	0.016	0.982	0.086	0.030	$\approx 0$	0.031	$\approx 0$	0.025	$\approx 0$
	$\tilde{i}_{cqref}$	$\approx 0$	0.001	$\approx 0$	0.115	0.878	0.001	0.057	0.007	0.002	$\approx 0$	0.0

### 3.6 Summary

This chapter has studied the small-signal stability of the WPSU, based on the eigenvalue and participation factor analyses. The objective was to characterize the behavior of the dominant eigenvalue(s), under different parameters sets and operating conditions.

## **Chapter 4**

# **Reliability of the Remote Electrification System**

### **4.1 Introduction**

Chapter 2 studied the operation and control of a Wind-Power and Storage Unit (WPSU) to run in the islanded as well as the grid-connected mode of operation. Chapter 3 presented a small-signal model for and an eigenvalue analysis on the WPSU. This chapter deals with the issues of reliability and components rating for the WPSU.

### **4.2 List of Symbols**

The nature of the study reported in this chapter is different than those of Chapter 2 and Chapter 3. This difference has brought about the need for the introduction of new symbols or the use of old symbols in different contexts. Thus, to circumvent any confusions, in this section we introduce the symbols specific to this chapter:

- $s_l$  : Slip of DFIG  
 $f(.)$  : Probability density function  
 $F(.)$  : Cumulative distribution function  
 $P_r(.)$  : Probability of  
 $V$  : Wind speed, in  $m/s$   
 $V_{ci}$  : Cut-in wind speed, in  $m/s$   
 $V_r$  : Rated wind speed, in  $m/s$   
 $V_{co}$  : Cut-out wind speed, in  $m/s$   
 $i$  : Subscript denoting the state-of-health of the generator  
 $j$  : Subscript denoting the wind-speed condition  
 $s_{1j}^{(k)}$  : State in which generator  $k$  is in the wind-speed condition  $j$  and available  
 $s_{2j}^{(k)}$  : State in which generator  $k$  is in the wind-speed condition  $j$  and unavailable  
 $P_{ij}^{(k)}$  : Power output of generator  $k$ , in  $kW$ , in state  $s_{ij}$   
 $P_{ij}$  : Total power output, in  $kW$ , in state  $s_{ij}$   
 $P_{rat}$  : Rated power, in  $kW$   
 $P_{rot}$  : Rotor power of DFIG, in  $kW$   
 $P_{bat}$  : Battery power, in  $kW$   
 $P_L$  : Load power, in  $kW$   
 $P_{Le}$  : Effective load power, in  $kW$   
 $P_{ch-max}$  : Maximum permissible charging battery power, in  $kW$   
 $P_{dch-max}$  : Maximum permissible discharging battery power, in  $kW$   
 $P_{ex}$  : Battery power available for export, in  $kW$

$E_{min}$  : Minimum permissible battery stored energy, in  $kWh$

$E_{max}$  : Maximum permissible battery stored energy, in  $kWh$

### 4.3 Background on Reliability Assessment Methods

Wind energy is stochastic in nature and, as such, is often characterized by means of probabilistic techniques [36]. Reference [37] establishes that probabilistic methods in power systems are preferred over deterministic methods, even for short-term reserve planning calculations. In power systems, two distinct probabilistic methods exist for the calculation of reliability indices [38]. These are: (1) the closed-form (or analytical) method and (2) the simulation-based method [39]. Based on the analytical approach, [40]- [42], Weibull probability density function (pdf) and the corresponding cumulative distribution function (cdf) are usually employed to characterize the wind speed [43]. These functions, in conjunction with the turbine power/wind-speed characteristic function, [44]- [48], characterize the power output of a wind-power unit. The main shortcoming of the analytical approach is that it cannot readily take into account the chronological variations of the wind speed and the battery state-of-charge [12]. By contrast, in the simulation-based approach, wind speed is forecasted through a time-series analysis on the past wind data [49]. Although accurate, the simulation-based method requires a fairly complex forecast model and large amount of past wind data [50]- [51]. In a number of investigations, wind and hybrid systems augmented with battery energy storage are modeled and an-

alyzed through probabilistic techniques [52]- [53]. However, the reported studies do not consider the generators Forced Outage Rate (FOR) and are limited to the islanded mode of operation.

This chapter proposes a new reliability assessment methodology for the WPSU. The proposed reliability assessment methodology combines the traditional simulation-based [39] and analytical [38] approaches and, with minor modifications, is also applicable to different configurations of hybrid systems. The proposed method takes into consideration the FOR of the wind-power unit(s), the FOR of the transmission line, the battery capacity and required power handling capability, and the random natures of the wind and load. Moreover, it requires a fairly limited volume of the past wind-speed data. The proposed algorithm has been implemented in Matlab software environment, and its application to the electrification system of Chapter 2 has been demonstrated.

#### **4.4 Study System**

Fig. 4.1 illustrates a simplified schematic diagram of the study remote electrification system of Fig. 2.1 which is customized for this chapter and repeated here for ease of reference. Fig. 4.1 shows that the WPSU is based on a Doubly-Fed Induction Generator (DFIG) which is controlled by the back-to-back connection of a Rotor-Side Converter (RSC) and a Grid-Side Converter (GSC); a battery bank is interfaced with the converters dc link. Fig. 4.1 also shows that the distribution network embeds a Constant-Speed induction generator-based wind-power Unit (CSU), an aggregate of local

loads, and a switch that can establish or interrupt the connection between the distribution network and the power system.

In Fig. 4.1,  $P_{ij}^{(1)}$  and  $P_{ij}^{(2)}$  signify the wind powers extracted by the WPSU and the CSU, respectively; the total wind power,  $P_{ij}^{(1)} + P_{ij}^{(2)}$ , is denoted hereinafter by  $P_{ij}$ . In the islanded mode, the battery power,  $P_{bat}$ , is automatically controlled through the voltage/frequency regulation scheme introduced in Chapter 2, to compensate for the difference between  $P_{ij}$  and the total load power,  $P_L$ . In the grid-connected mode, however,  $P_{bat}$  is an independent control variable to either charge the battery or deliver a pre-specified amount of power to the rest of the system, as explained in Chapter 2.

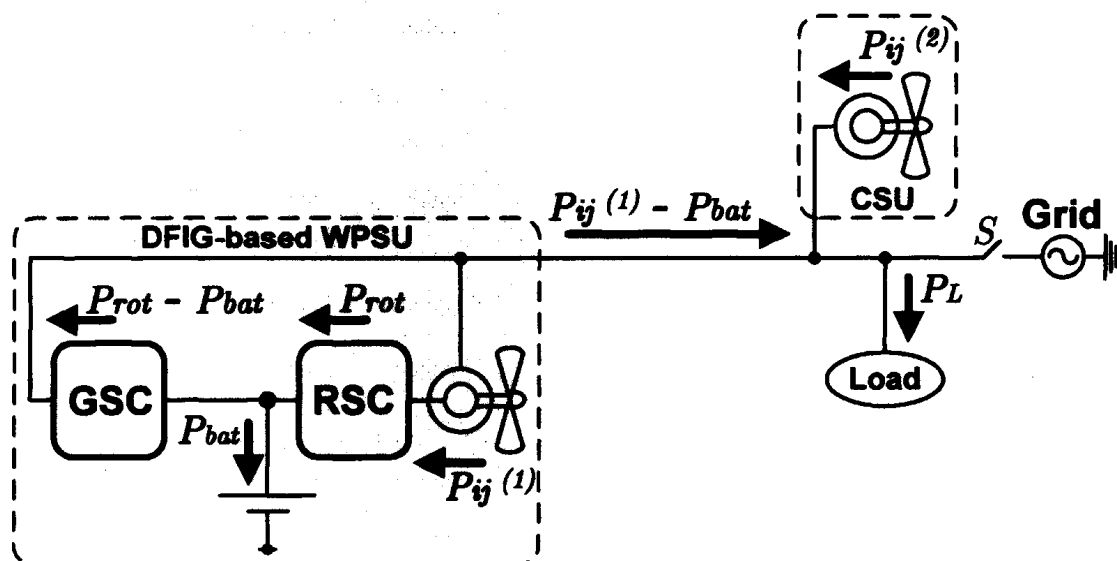


Fig. 4.1: Single line schematic diagram of the remote electrification system

#### 4.4.1 Reliability Indices

##### 4.4.1.1 Loss of Load Expectation (LOLE)

The LOLE is the expected duration within a certain period of time, for example one year, over which the load demand exceeds the total generated power. Mathematically, the LOLE is expressed as

$$\begin{aligned} LOLE &= \sum_{h=1}^{n=8760} P_r \left( (P_{ij}[h] - P_{Le}[h]) < 0 \right) \\ &= \sum_{h=1}^{n=8760} P_r \left( P_{ij}[h] < P_{Le}[h] \right) \quad [hrs/year] \end{aligned} \quad (4.1)$$

where  $P_{ij}[h]$  is the total generation during the  $h^{th}$  hour and  $n = 8760$  is the number of hours in a year.  $P_{Le}[h]$  is the effective load power which is precisely defined in Section 4.4.2.

##### 4.4.1.2 Loss of Load Probability (LOLP)

The probability of the load demand surpassing the total generation is called the LOLP. For accurate results, the LOLP is usually calculated by using a large number of events. The LOLP is unit-less and related to the LOLE as

$$LOLP = \frac{LOLE}{n}, \quad (4.2)$$

where  $n = 8760$  is the number of hours in a year.

##### 4.4.1.3 Loss of Energy Expectation (LOEE)

The total amount of energy in a year, in  $kWh$ , by which the total generation falls short of the load demand is called the LOEE. Mathematically, the

LOEE is formulated as

$$LOEE = \sum_{h=1, P_{Le}[h] > P_{ij}[h]}^{n=8760} (P_{Le}[h] - P_{ij}[h]). \quad (4.3)$$

#### 4.4.2 Proposed Hybrid Approach for Reliability Assessment

The following algorithm is proposed in this thesis for calculation of the reliability indices for the remote electrification system of Fig. 4.1:

1. Hourly wind speeds of, for example, one year, expressed in the form of a time series, are input to the turbine(s) power/wind-speed characteristic function(s), and a time series is generated for the total power generation  $P_{ij} = P_{ij}^{(1)} + P_{ij}^{(2)}$ ;
2. Based on either a load model or a set of hourly recorded data, a time series is constructed for the load power  $P_L$ ;
3. Based on  $P_{ij}$ ,  $P_L$ , and the control logic of the WPSU, the battery stored energy,  $E_{bat}$ , is calculated for all hours. Then, based on  $E_{bat}$ , the battery power available for export,  $P_{ex}$ , and subsequently the “effective load power”,  $P_{Le} = P_L - P_{ex}$ , are calculated for each hour and expressed in time-series forms; and
4. Using the “capacity-in probability table”,  $P_r(P_{ij}[h] < P_{Le}[h])$  is calculated for each hour. Then, the hourly probabilities are integrated to calculate the LOLE, based on (4.1), and the LOLP, based on (4.2). Moreover, all the hourly values of  $P_{Le}[h] - P_{ij}[h]$  that are positive are

identified as the hourly “unserved energy” and summed up to calculate the LOEE, based on (4.3). The generators FOR take part in construction of the capacity-in probability table.

#### 4.4.2.1 Construction of Time Series for the Total Power Generation

To construct the total power generation, hourly wind speed data, i.e.  $V[h]$ , is required. It is assumed in this paper that the data is available for at least one year and can be expressed as a time series. Using the time series and the turbine(s) power/wind-speed characteristic(s), the time series for the total power generation  $P_{ij} = P_{ij}^{(1)} + P_{ij}^{(2)}$  can be constructed. In addition, a continuous pdf can be fitted on the time series to enable calculation of the probability of the wind speed to lie within a certain range. This probability is required for the construction of the capacity-in probability table, as further explained in Section 4.4.2.4. The most commonly adopted pdf for this purpose is the Weibull pdf [43]:

$$f(V) = \frac{\beta}{\alpha} \left(\frac{V}{\alpha}\right)^{\beta-1} \exp\left[-\left(\frac{V}{\alpha}\right)^\beta\right] \quad (4.4)$$

where  $V$  is the wind speed in  $m/s$ .  $\alpha$  and  $\beta$  are the pdf scale and shape parameters, respectively, and can be estimated using the wind speed time series. For the Weibull pdf, (4.4), the corresponding cdf is

$$\begin{aligned} F(V_0) &= Pr(V \leq V_0) = \int_0^{V_0} f(v)dv \\ &= 1 - \exp\left[-\left(\frac{V_0}{\alpha}\right)^\beta\right]. \end{aligned} \quad (4.5)$$

which formulates the probability of the wind speed  $V$  being smaller than a value,  $V_0$ .

For each wind-power unit, the power output,  $P_{ij}^{(k)}$ , is calculated based on [44]:

$$P_{ij}^{(k)} = \begin{cases} 0 & \text{if } V < V_{ci} \text{ or } V > V_{co} \\ (a + bV + cV^2)P_{rat}^{(k)} & \text{if } V_{ci} \leq V \leq V_r \\ P_{rat}^{(k)} & \text{if } V_r \leq V < V_{co} \end{cases} \quad (4.6)$$

where  $V_{ci}$ ,  $V_r$ , and  $V_{co}$  are the cut-in, rated, and cut-out wind speeds, respectively.  $P_{rat}^{(k)}$  signifies the rated power output of the wind-power unit. The coefficients  $a$ ,  $b$ , and  $c$  can be calculated from the following equations [44], [41]:

$$a = \frac{1}{(V_{ci} - V_r)^2} \left\{ V_{ci}(V_{ci} + V_r) - 4(V_{ci} \times V_r) \left( \frac{V_{ci} + V_r}{2V_r} \right)^3 \right\} \quad (4.7)$$

$$b = \frac{1}{(V_{ci} - V_r)^2} \left\{ 4(V_{ci} + V_r) \left( \frac{V_{ci} + V_r}{2V_r} \right)^3 - (3V_{ci} + V_r) \right\} \quad (4.8)$$

$$c = \frac{1}{(V_{ci} - V_r)^2} \left\{ 2 - 4 \left( \frac{V_{ci} + V_r}{2V_r} \right)^3 \right\}. \quad (4.9)$$

Equation (4.6) indicates that the power output is zero for wind speeds below  $V_{ci}$  or above  $V_{co}$ . Based on (4.6), the output power is held constant at  $P_{rat}^{(k)}$  when the wind speed is between  $V_r$  and  $V_{co}$ ; this is ensured by pitch-angle control in the WPSU or by stall control in the CSU. Equation (4.6) further indicates that when the wind speed is between  $V_{ci}$  and  $V_r$ , the power output is a quadratic function of the wind speed.

#### 4.4.2.2 Construction of Time Series for Load Power Consumption

The simplest widely-adopted load model is based on the hourly peak power consumption [38], and is constructed by recording the load peak power in a particular site, over, for example, one year. This model yields a fairly accurate representation of the load, since it also accounts for the seasonal load changes.

Alternatively, the load can be characterized by a pdf. Two commonly used pdfs are the normal pdf and the uniform pdf. For a normally distributed load, the pdf is

$$f(P_L) = \frac{1}{\sqrt{2\pi}\sigma} e^{-\left(\frac{P_L - m}{\sqrt{2}\sigma}\right)^2} \quad (4.10)$$

where  $m$  is the mean value and  $\sigma$  is the standard deviation. For simulations, the corresponding time series for the load power can be generated based on (4.10). For example, in Matlab software environment, the following command can be used to generate a time series for  $P_L[h]$  :

$$P_L[h] = \left(\frac{P_{Lmax} + P_{Lmin}}{2}\right) + \left(\frac{P_{Lmax} - P_{Lmin}}{N_\sigma}\right) \times randn(1, 8760), \quad (4.11)$$

where  $P_L[h]$  is the (random) load power in the  $h^{th}$  hour of the year,  $P_{Lmax}$  is the maximum yearly load peak power, and  $P_{Lmin}$  is the minimum yearly load peak power.  $N_\sigma$  is a parameter that determines the variability of the generated time series.

Similarly, the pdf of a uniformly distributed load can be expressed as

$$f(P_L) = \begin{cases} \frac{1}{P_{Lmax} - P_{Lmin}} & \text{if } P_{Lmin} \leq P_L \leq P_{Lmax} \\ 0 & \text{otherwise} \end{cases} \quad (4.12)$$

for which the time series can be generated, for example, based on the following Matlab command:

$$P_L[h] = P_{Lmin} + (P_{Lmax} - P_{Lmin}) \times rand(1, 8760). \quad (4.13)$$

If the diurnal load variations are of prime importance, the IEEE-RTS load model is often adopted. In this paper, the IEEE-RTS load model is constructed based on the method described in [39] and [54].

Commonly, the hourly load peak power values are arranged in a descending order, and the resultant time series is referred to as the Load Duration Curve (LDC) [39]. An LDC indicates the total number of hours in a year during which the load power is larger than a value on the vertical axis. To enable better comparisons, three LDCs corresponding to a hypothetical load are shown in Fig. 4.2. The load maximum and minimum yearly peak powers are 350 kW and 120 kW, respectively. The three LDCs of Fig. 4.2 are generated based on the IEEE-RTS model, equation (4.13), and equation (4.11) with  $N_\sigma = 8$ , respectively.

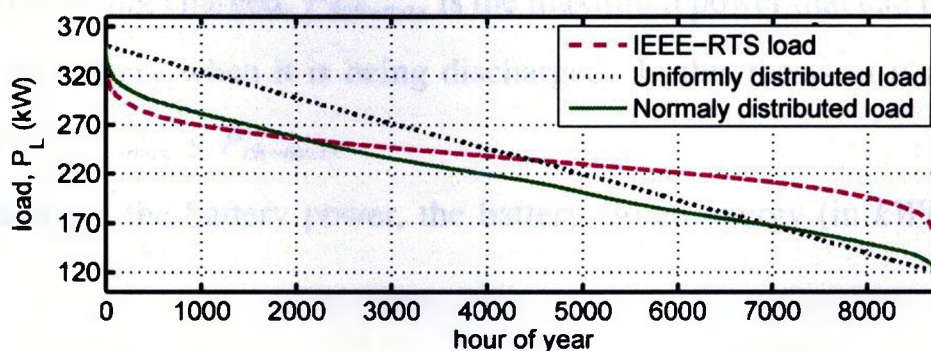


Fig. 4.2: Load Duration Curves (LDCs) corresponding to three different load models

#### 4.4.2.3 Construction of Time Series for Battery Power, Battery Stored Energy, and Battery Power Available for Export

Due to the variable natures of wind and load, in an off-grid electrification system the total power output of the wind-power units does not necessarily match the load power. Therefore, a properly sized battery bank is added to compensate for the power imbalance and to ensure voltage and frequency stability. The battery power is conditioned by the GSC of the WPSU, Fig. 4.1, and is controlled through a voltage/frequency regulation strategy introduced in Chapter: 2.

In the islanded mode, the battery power is expressed as

$$P_{bat}[h] = \begin{cases} -P_{dch-max} & \text{if } P_{ij}[h] - P_L[h] \leq -P_{dch-max} \\ P_{ij}[h] - P_L[h] & \text{if } -P_{dch-max} \leq P_{ij}[h] - P_L[h] \leq P_{ch-max} \\ P_{ch-max} & \text{if } P_{ij}[h] - P_L[h] \geq P_{ch-max} \end{cases} \quad (4.14)$$

where  $P_{ch-max}$  is the maximum power that can be delivered to the battery when it is being charged.  $P_{dch-max}$  is the maximum power that can be drawn from the battery when it is being discharged. In this thesis, it is assumed that  $0 < P_{dch-max} \leq P_{ch-max}$ .

Based on the battery power, the battery stored energy (in *kWh*) is de-

scribed by the following dynamic equation:

$$E_{bat}[h + 1] = \begin{cases} E_{min} & \text{if } E_{bat}[h] + P_{bat}[h] \leq E_{min} \\ E_{bat}[h] + P_{bat}[h] & \text{if } E_{min} \leq E_{bat}[h] + P_{bat}[h] \leq E_{max} \\ E_{max} & \text{if } E_{max} \geq E_{bat}[h] + P_{bat}[h] \end{cases} \quad (4.15)$$

where  $E_{min}$  and  $E_{max}$  are, respectively, the lower and upper limits of the battery stored energy, and  $1 \leq h \leq 8760$ . Moreover,  $E_{bat}[1]$  is picked as  $E_{min}$  to represent the worst-case scenario, although a randomly generated initial value (for example, based on a normal distribution function) or the average value of the battery energy could also have been used.  $E_{min}$  and  $E_{max}$  impose major implications on the reliability of the electrification system of Fig. 4.1.

As (4.14) indicates, the battery power  $P_{bat} = P_{ij} - P_L$  must be limited from the upper side to the maximum value  $P_{ch-max}$ . This is ensured through the pitch-angle control mechanism of WPSU and, if not adequately effective, the introduction of dump loads.  $P_{bat}$  must also be limited from the lower side to  $-P_{dch-max}$ . Thus, in case of inadequate generation, if the pitch angle of the WPSU is already at its minimum, the loads may have to be dropped or the system be entirely shut down. The same measures are also taken if  $E_{bat}[h + 1]$  is either to exceed  $E_{max}$  or to become less than  $E_{min}$ .

The battery power available for export,  $P_{ex}$ , is defined as

$$P_{ex}[h] \triangleq \begin{cases} E_{bat}[h] - E_{min} & \text{if } E_{bat} - E_{min} \leq P_{dch-max} \\ P_{dch-max} & \text{if } E_{bat} - E_{min} > P_{dch-max} \end{cases} \quad (4.16)$$

It should be noted that, unlike  $P_{bat}$ ,  $P_{ex}$  is a positive mathematical variable which bears no physical meaning.  $P_{ex}$  represents the amount of power that

can potentially be drawn from the battery if  $P_L$  exceeds  $P_{ij}$ . As (4.16) indicates,  $P_{ex}$  depends on  $E_{bat}$  and is limited to  $P_{dch-max}$ ; its magnitude is such that the battery cannot be discharged to any level lower than  $E_{min}$ , in a one-hour period.

#### 4.4.2.4 Construction of the Capacity-In Probability Table

FOR is the probability of a generator being out of service for a period of time [38]. Alternatively,  $1-FOR$  is the probability of a generator being operational. Thus, the power output of a wind-power unit, as formulated by (4.6), depends not only on the wind condition, but also on the FOR. This is graphically illustrated by the state transition diagram of Fig. 4.3 in which three states are identified as “Down”, “Up1”, and “Up2”. The state “Down” indicates that either the generator is out of service or the wind speed lies within the first piece of (4.6). “Up1” and “Up2” both represent a healthy generator. They, however, correspond to two different wind speed ranges; these are, respectively, (1) the wind speeds higher than  $V_{ci}$  but lower than

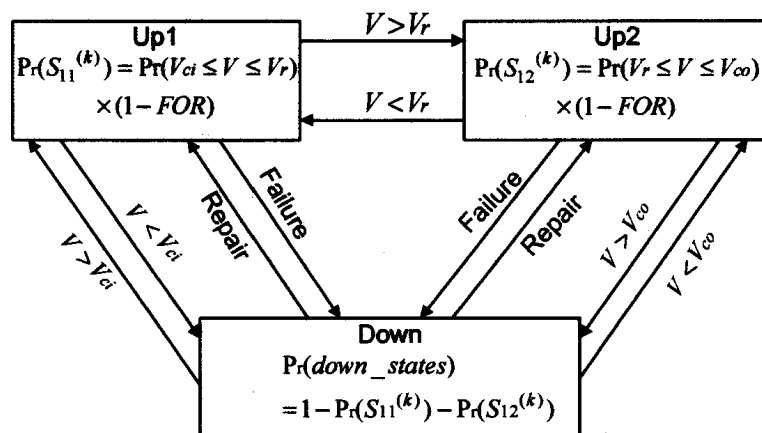


Fig. 4.3: State transition diagram for a wind-power unit without energy storage

**Table 4.1:** States Probabilities for Generator  $k$ 

State	State Probability	Expected Power Output
$S_{11}^{(k)}$	$(1 - FOR) \times P_r(V_{ci} \leq V \leq V_r)$	$P_{11}^{(k)}$ (equation (4.17))
$S_{12}^{(k)}$	$(1 - FOR) \times P_r(V_r \leq V < V_{co})$	$P_{12}^{(k)} = P_{rat}^{(k)}$
$S_{13}^{(k)}$	$(1 - FOR) \times P_r(V < V_{ci} \cup V \geq V_{co})$	$P_{13}^{(k)} \equiv 0$
$S_{21}^{(k)}$	$FOR \times P_r(V_{ci} \leq V \leq V_r)$	$P_{21}^{(k)} \equiv 0$
$S_{22}^{(k)}$	$FOR \times P_r(V_r \leq V < V_{co})$	$P_{22}^{(k)} \equiv 0$
$S_{23}^{(k)}$	$FOR \times P_r(V < V_{ci} \cup V \geq V_{co})$	$P_{23}^{(k)} \equiv 0$

$V_r$ , and (2) the wind speeds higher than  $V_r$  but lower than  $V_{co}$ . Table 4.1 provides the states probabilities and the corresponding power outputs, based on the diagram of Fig. 4.3. The states are generically denoted by  $S_{ij}^{(k)}$ .

For  $S_{ij}^{(k)}$ ,  $k = 1$  corresponds to the WPSU, whereas  $k = 2$  represents the CSU. The subscript  $i$  represents the state-of-health of the generator in question. Thus,  $i = 1$  represents a healthy corresponding generator, whereas  $i = 2$  indicates that the generator is out of service. The subscript  $j$  corresponds to a wind-speed range, as identified in Table 4.2. Due to the three wind-speed conditions and states of health, each generator can assume any of the six states introduced in Table 4.1. A brief explanation on the construction of Table 4.1 follows.

Consider, for example, the states  $S_{11}^{(k)}$  and  $S_{12}^{(k)}$ . These states indicate that the generator  $k$  is healthy and can potentially deliver power. For both

**Table 4.2:** Explanation of Subscript  $j$  in  $S_{ij}^{(k)}$  ( $i = 1$  or  $2$ )

$j$	Wind Condition
1	$V_{ci} \leq V \leq V_r$
2	$V_r \leq V < V_{co}$
3	$V < V_{ci}$ or $V \geq V_{co}$

states, the wind speed is in such a range that enables power generation. Now consider the state  $S_{13}^{(k)}$ ; although in this state the generator is healthy, the power output is zero due to the wind speed range (see Table 4.2). In the states  $S_{21}^{(k)}$ ,  $S_{22}^{(k)}$ , and  $S_{23}^{(k)}$ , the generator is out of service. Consequently, the power output is zero, irrespective of the wind-speed condition. In Table 4.1, the power output corresponding to the state  $S_{ij}^{(k)}$  is denoted by  $P_{ij}^{(k)}$ . Thus, as Table 4.1 shows, a generator delivers power only if it is healthy and the wind speed is in an appropriate range.

The probability of each state is equal to the probability of the unit being healthy or unhealthy, multiplied by the probability of the wind-speed being within the corresponding range. For example, the probability of  $S_{11}^{(k)}$  is the probability of the generator being up, that is  $1-\text{FOR}$ , times  $P_r(V_{ci} \leq V \leq V_r)$  which is calculated based on (4.5). As another example, the probability of  $s_{22}^{(k)}$  is the probability of the generator being out of service, i.e.  $\text{FOR}$ , multiplied by  $P_r(V_r \leq V < V_{co})$ , and so forth.

If both the WPSU and the CSU are considered, Table 4.1 can be expanded to Table 4.3 which includes all possible combinations of the states,

**Table 4.3:** State Probabilities and Corresponding Power Outputs for the System of Fig. 4.1

$j$	$S_{ij}^{(1)}$	$S_{lj}^{(2)}$	$P_r(S_{ij}^{(1)} \& S_{lj}^{(2)})$	Expected Total Power Output
1	$S_{11}^{(1)}$	$S_{11}^{(2)}$	$(1 - FOR)^2 \times Pr(V_{ci} \leq V < V_r)$	$P_{11}^{(1)} + P_{11}^{(2)}$
	$S_{11}^{(1)}$	$S_{21}^{(2)}$	$(1 - FOR)(FOR) \times Pr(V_{ci} \leq V < V_r)$	$P_{11}^{(1)}$
	$S_{21}^{(1)}$	$S_{11}^{(2)}$	$(FOR)(1 - FOR) \times Pr(V_{ci} \leq V < V_r)$	$P_{11}^{(2)}$
	$S_{21}^{(1)}$	$S_{21}^{(2)}$	$(FOR)^2 \times Pr(V_{ci} \leq V < V_r)$	0
2	$S_{12}^{(1)}$	$S_{12}^{(2)}$	$(1 - FOR)^2 \times Pr(V_r \leq V < V_{co})$	$P_{12}^{(1)} + P_{12}^{(2)} = P_{rat}^{(1)} + P_{rat}^{(2)}$
	$S_{12}^{(1)}$	$S_{22}^{(2)}$	$(1 - FOR)(FOR) \times Pr(V_r \leq V < V_{co})$	$P_{12}^{(1)} = P_{rat}^{(1)}$
	$S_{22}^{(1)}$	$S_{12}^{(2)}$	$(FOR)(1 - FOR) \times Pr(V_r \leq V < V_{co})$	$P_{12}^{(2)} = P_{rat}^{(2)}$
	$S_{22}^{(1)}$	$S_{22}^{(2)}$	$(FOR)^2 \times Pr(V_r \leq V < V_{co})$	0
3	$S_{13}^{(1)}$	$S_{13}^{(2)}$	$(1 - FOR)^2 \times Pr(V < V_{ci} \& V > V_{co})$	0
	$S_{13}^{(1)}$	$S_{23}^{(2)}$	$(1 - FOR)(FOR) \times Pr(V < V_{ci} \& V > V_{co})$	0
	$S_{23}^{(1)}$	$S_{13}^{(2)}$	$(FOR)(1 - FOR) \times Pr(V < V_{ci} \& V > V_{co})$	0
	$S_{23}^{(1)}$	$S_{23}^{(2)}$	$(FOR)^2 \times Pr(V < V_{ci} \& V > V_{co})$	0

their corresponding probabilities, and their respective power outputs. It should be noted that since both generators are assumed to be subject to the same wind condition, for calculation of  $P_r(S_{ij}^{(1)} \& S_{ij}^{(2)})$ , the probability of the wind speed to be within a specific range appears as a first-order factor. However, the probability of the availability or unavailability of a generator is assumed to be independent of that of the other generator; the former probability is 1-FOR whereas the latter one is FOR.

If the elements of Table 4.3 are evaluated numerically and sorted in a descending order in terms of  $P_{ij}$ , the resultant table is referred to as the capacity-in probability table. The capacity-in probability table provides the probability of the generated power being less than or equal to a given value.

In constructing the numerical version of the capacity-in probability table, one complication is encountered; for each of the states  $S_{11}^{(1)} \& S_{11}^{(2)}$ ,  $S_{11}^{(1)} \& S_{21}^{(2)}$ , and  $S_{21}^{(1)} \& S_{11}^{(2)}$ , the power output of the healthy unit(s), i.e.  $P_{11}^{(k)}$ , can assume any value(s) between zero and the unit(s) corresponding rated power(s), depending on the wind speed in that particular hour. Similarly, the probability of the wind speed to be equal to the wind speed in that hour must be computed. To resolve this complication, the wind-speed range  $V_{ci} \leq V \leq V_r$  is divided into a number of equal intervals. Then, the average power corresponding to each interval is estimated as

$$P_{11}^{(k)} = \frac{\int_{\eta}^{(\eta+\Delta V)} P_{rat}^{(k)} (a + bv + cv^2) dv}{\Delta V}, \quad (4.17)$$

where  $\eta$  marks the beginning of the interval and  $\Delta V$  is the interval length.

The probability of the wind speed being in the range  $\eta \leq V \leq \eta + \Delta V$  is calculated based on (4.5) as

$$\begin{aligned} Pr(\eta \leq V \leq \eta + \Delta V) &= \int_{\eta}^{(\eta+\Delta V)} f(V)dV \\ &= F(\eta + \Delta V) - F(\eta) \end{aligned} \quad (4.18)$$

In this chapter, the range  $V_{ci} \leq V \leq V_r$  is divided into four equal intervals. Therefore, the top three rows of Table 4.3, collectively, correspond to twelve rows of the numerical version of Table 4.3, which is reported in Section 4.6 as Table 4.4.

## 4.5 Grid-Side Converter (GSC) Rating

In a conventional DFIG-based wind-power unit, the RSC and GSC handle a relatively small fraction of the DFIG generated power, approximately proportional to the DFIG slip and roughly limited to less than about 30% of the DFIG rated power. While in the WPSU of Fig. 4.1 the rating of the RSC is the same as that in a conventional counterpart, the rating of the GSC may need to be considerably larger than due to both the battery and rotor power flows, Fig. 4.1.

The rotor power can be expressed in terms of the power output  $P_{ij}^{(1)}$  as

$$P_{rot} = \frac{s_l}{1 + s_l} P_{ij}^{(1)} \quad (4.19)$$

where  $s_l$  signifies the DFIG slip and is related to  $P_{ij}^{(1)}$  as

$$s_l = \begin{cases} (KP_{ij}^{(1)})^{1/3} - 1 & \text{if } V_{ci} \leq V \leq V_{co} \\ \text{don't care otherwise} & \end{cases} \quad (4.20)$$

where  $K$  is a constant. Fig. 4.4 illustrates the patterns of variation of  $s_l$ ,  $P_{rot}$ , and  $P_{ij}^{(1)}$ , for the WPSU when the wind speed changes from about 4 m/s to 20 m/s, and  $K = 1.309 \times 10^{-3} (kW)^{-1}$ .

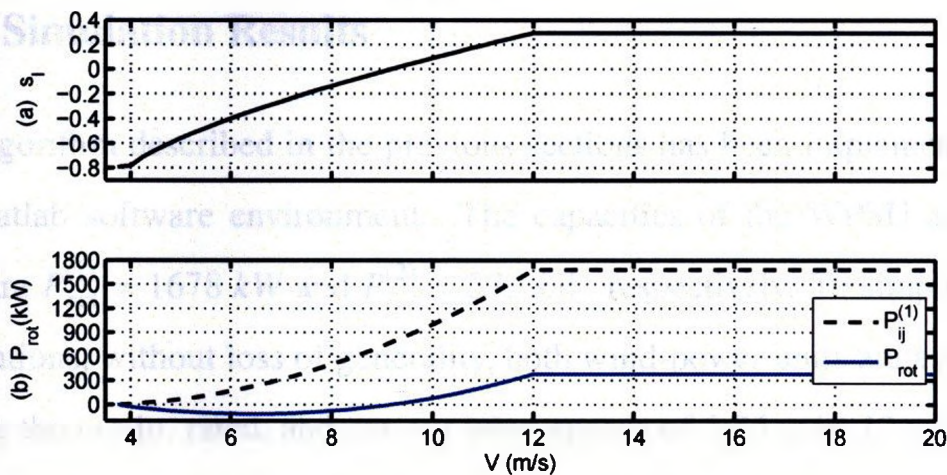


Fig. 4.4: Variations of (a) slip and (b) rotor power as functions of the wind speed

Equations (4.19) and (4.20) enable the construction of a time series for  $P_{rot}$ . The time series for  $P_{rot}$  is, in turn, used to construct a time series for the GSC power, as

$$P_{GSC}[h] = P_{rot}[h] - P_{bat}[h] \quad (4.21)$$

where  $P_{bat}[h]$  is given by (4.14). Equation (4.21) indicates that  $P_{GSC}$  is composed of two counteracting components. To appreciate this, assume that the wind speed is large at some hours. This results in a large output power  $P_{ij}$ . Thus, the DFIG rotor power is positive and relatively large (equations

(4.19) and (4.20), Fig. 4.4). On the other hand, the large power generation most likely exceeds the load and, thus, results in a positive large value of  $P_{bat}$ . Consequently, the effect of large  $P_{rot}$  in  $P_{GSC}$  is outweighed. The same conclusions can also be made for a condition where the wind speed and the power output are low. The effect described above is desirable since it is in favor of a lower capacity GSC.

## 4.6 Simulation Results

The algorithm described in the previous sections has been implemented in the Matlab software environment. The capacities of the WPSU and the CSU are  $P_{rat}^{(1)} = 1678 \text{ kW}$  and  $P_{rat}^{(2)} = 373 \text{ kW}$ , respectively. To simplify the calculations, without loss of generality, both wind-power units are assumed to have the cut-in, rated, and cut-out wind speeds of  $3.75 \text{ m/s}$ ,  $12 \text{ m/s}$ , and  $23.25 \text{ m/s}$ , respectively. The numerical values for the coefficients  $a$ ,  $b$ , and  $c$  are  $0.1203$ ,  $-0.08$ , and  $0.0128$ , respectively. The other parameters are as follows, unless otherwise mentioned:

The wind-speed data is obtained from Environment Canada [55]. The data is recorded in the year 2007, in Argentinia (AUT), Newfoundland. The same data is also used to specify the parameters of Weibull pdf as  $\alpha = 8.0231$  and  $\beta = 1.9852$ . For the load power, an IEEE-RTS load model has been constructed [38], [54], that corresponds to the minimum and maximum yearly peak power values of, respectively,  $120 \text{ kW}$  and  $350 \text{ kW}$ , Fig. 4.2. For the batteries,  $P_{ch-max} = 800 \text{ kW}$ ,  $P_{dch-max} = 350 \text{ kW}$ , and  $E_{min} = 0.05E_{max}$ . For both the WPSU and the CSU, FOR= 3%. However, FOR= 0 for the

battery and the GSC. Table 4.4 is the numerical version of the capacity-in probability table of Table 4.3 and is used for calculation of the LOLE. For example, if  $P_{Le}[h] = 720 \text{ kW}$  at a given hour, then based on Table 4.4,  $P_r(P_{ij}[h] \leq 700 \text{ kW}) = 0.6457$ ; this process is repeated for all the hours of the year and the LOLE is determined based on (4.1).

**Table 4.4:** Numerical Version of the Capacity-In Probability Table of Table 4.3

$\gamma$	$P_r(P_{ij} = \gamma)$	$P_r(P_{ij} \leq \gamma)$
2051	0.0974	1.0000
1678	0.0051	0.9026
1609	0.0979	0.8975
1316	0.0052	0.7995
872	0.1487	0.7944
714	0.0078	0.6457
373	0.0051	0.6378
360	0.1883	0.6327
294	0.0099	0.4444
292	0.0052	0.4345
158	0.0078	0.4293
70	0.1910	0.4215
65	0.0099	0.2305
57	0.0101	0.2206
12	0.0101	0.2106
0	0.2005	0.2005

#### 4.6.1 Case-1: Impact of Units FOR on the LOLE

The impact of the battery capacity  $E_{max}$  on the LOLE, for different values of FOR, is illustrated in Fig. 4.5. It is observed that, as expected, without battery the LOLE is prohibitively large. However, it decreases with the increase of  $E_{max}$ ; for values beyond about 30,000 kWh, the LOLE is relatively small and any further increase in  $E_{max}$  does not result in a substantially lower LOLE. Fig. 4.5 also indicates that a higher FOR corresponds to a higher LOLE, for a given battery capacity. This impact, however, becomes less pronounced as the battery capacity is increased.

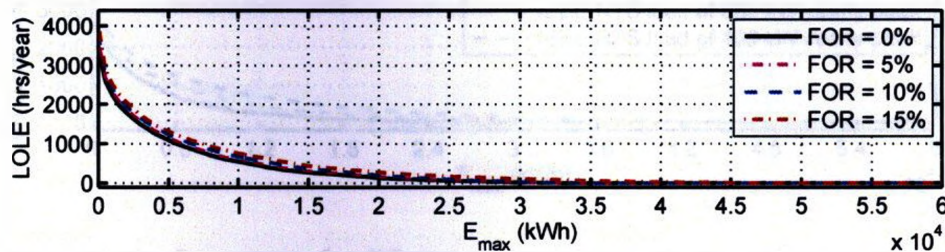


Fig. 4.5: Variations of LOLE vs. battery capacity, for different FOR

#### 4.6.2 Case-2: Impact of Load Distribution and Maximum Yearly Peak Power on the LOLE.

The load distribution can have an appreciable impact on the LOLE versus  $E_{max}$  curve. Fig. 4.6(a) illustrates the curves corresponding to the three different load distributions of Fig. 4.2. Fig. 4.6(a) indicates that while the LOLE exhibits very similar patterns of variation for the normal- and uniform-distributed loads, for a given  $E_{max}$ , the LOLE is the lowest for the

IEEE-RTS load.

Fig. 4.6(b) shows the LOLE versus  $E_{max}$  curves for three IEEE-RTS loads of different yearly maximum peak power values. It is observed that, expectedly, the LOLE increases as the load maximum peak power increases. However, the impact is relatively small for adequately large battery capacities, for example larger than 24,000 kWh.

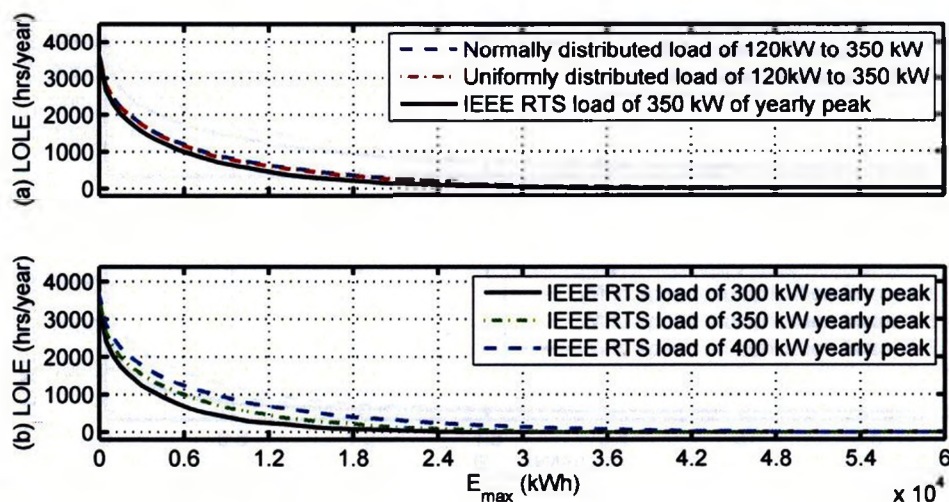


Fig. 4.6: LOLE vs.  $E_{max}$  curves for different (a) load distributions, and (b) load yearly peak powers

### 4.6.3 Case-3: Impact of Wind Profile and Magnitude on the LOLE.

The methodology presented in this chapter takes advantage of year-round wind-speed data. However, the wind profile is invariably different from year to year. Fig. 4.7(a) illustrates that the LOLE versus  $E_{max}$  curves based on the wind-speed data of the years 2007 and 2005 are remarkably different. However, the impact become negligible if the battery capacity is adequately large, for example larger than 24,000 kWh.

Fig. 4.7(b) demonstrates the effect of the wind strength on the LOLE versus  $E_{max}$  curve. To run this simulation, the wind-speed time series of the year 2007 has been scaled by factors of 1.1, 1.3, and 1.5. Fig. 4.7(b) shows that, as expected, for a given battery capacity the LOLE becomes lower as the scale factor becomes larger. However, the impact becomes negligible at adequately large battery capacities, for example larger than 24,000 kWh.

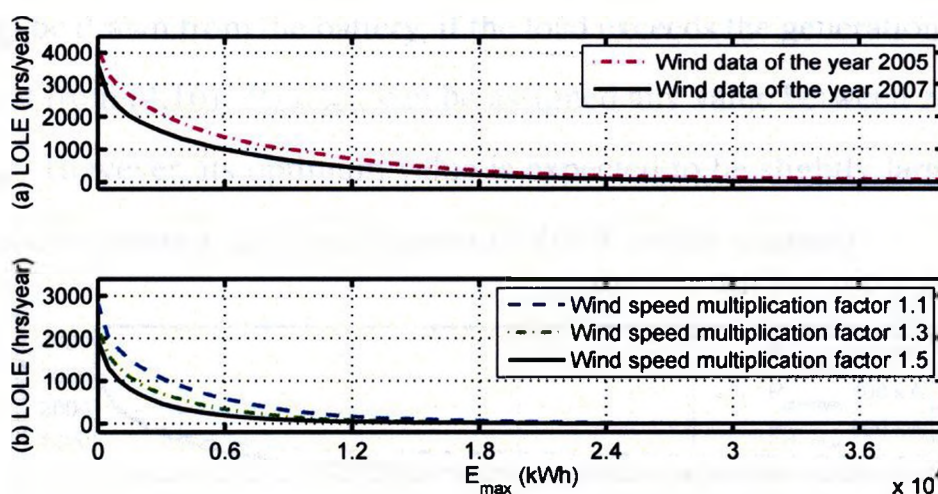


Fig. 4.7: LOLE vs.  $E_{max}$  curves for different (a) wind-speed time series, and (b) wind speed magnitudes

#### 4.6.4 Case-4: Impact of Maximum Permissible Battery Power on the LOLE

This case study demonstrates the impact of the maximum permissible battery charging and discharging rates, i.e.  $P_{ch-max}$  and  $P_{dch-max}$ , on the LOLE versus  $E_{max}$  curves. Fig. 4.8(a) indicates that for a given  $E_{max}$ , the LOLE decreases as  $P_{ch-max}$  is increased. The reason is that a higher  $P_{ch-max}$  enables a faster battery charging which, in turn, ensures that more energy would be stored in the battery to be dispatched, if at any subsequent hour the load

exceeds the generation. A higher  $P_{ch-max}$  translates into a higher-capacity GSC to handle the battery power and, therefore, should be chosen as the lowest value that fulfills the LOLE requirements.

Similarly, Fig. 4.8(b) indicates that, for a given battery capacity, the LOLE drops as  $P_{dch-max}$  is increased. The impact of  $P_{dch-max}$  on the LOLE is direct. The reason is that  $P_{dch-max}$  corresponds to the maximum power that can be drawn from the battery, if the load exceeds the generation; this is apparent from (4.16).  $P_{dch-max}$  can be assigned any value between zero and  $P_{ch-max}$ . However, its optimum value is expected to be slightly larger than the load maximum yearly peak power (350 kW in this chapter).

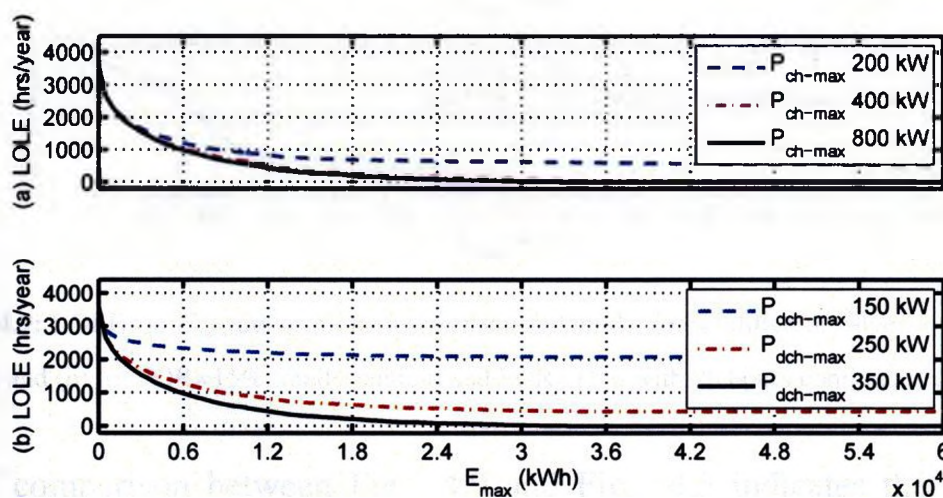
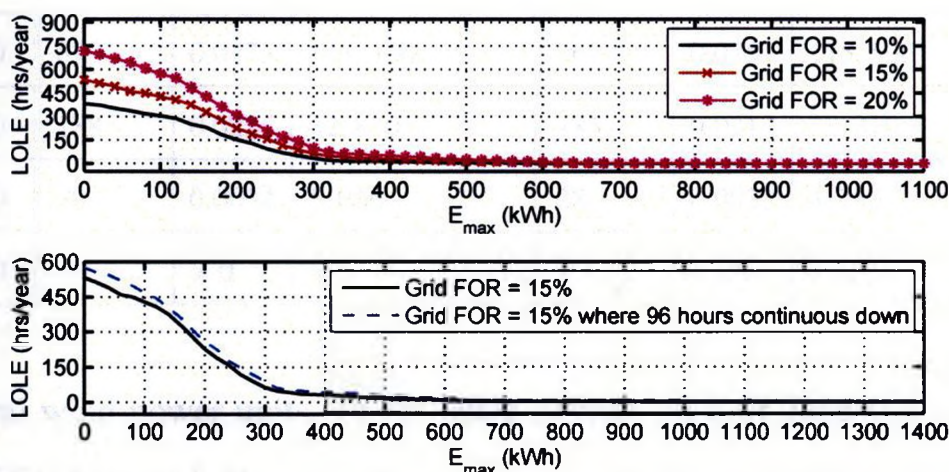


Fig. 4.8: LOLE vs.  $E_{max}$  curves for (a)  $P_{dch-max} = 350$  kW and different values of  $P_{ch-max}$ ; (b)  $P_{ch-max} = 800$  kW and different values of  $P_{dch-max}$ .

#### 4.6.5 Case-5: Impact of Grid FOR on the LOLE

The system of Fig. 4.1 can also operate in the grid-connected mode (2). Therefore, it is worthwhile studying the impact of the grid FOR on the

LOLE. Fig. 4.9(a) illustrates three LOLE versus  $E_{max}$  curves that correspond to different values of the grid FOR. Fig. 4.9(b) also illustrates a curve that corresponds to a grid FOR of 15% with the assumption that the grid downtime includes a continuous 96-hour period. Fig. 4.9 indicates that, for a given battery capacity, the LOLE increases with the increase of FOR. Moreover, for a given FOR, the LOLE is higher if the down times are continuous.



**Fig. 4.9:** LOLE vs.  $E_{max}$  curves in the grid-connected mode, for (a) different values of the grid FOR and (b) for FOR=15% totally random and FOR=15% with 96 hours continuous down

A comparison between Fig. 4.9 and Fig. 4.5 indicates that the required battery capacity is considerably smaller in the grid-connected mode, as compared to the the islanded mode, even if the grid is fairly unreliable.

#### 4.6.6 Case-6: Impact of Number of Generators on the LOLE

It is generally believed that modularity translates into higher reliability. Table 4.5 provides a comparison between the reliability indices of the study system of Fig. 4.1 and those of a hypothetical four-generator system of

**Table 4.5:** Reliability Indices for the System of Fig. 4.1 and a Hypothetical Four-Generator System

Battery Size kWh	System of Fig. 4.1 (1678 + 373) kW			Four-Generator System (4 × 513) kW		
	LOLE hrs/year	LOLP	LOEE kWh	LOLE hrs/year	LOLP	LOEE kWh
0	4,031	0.4602	648,100	3,953	0.4513	633,600
10,000	679	0.0775	118,400	663	0.0757	115,500
20,000	188	0.0215	32,870	185	0.0212	32,310
30,000	30	0.0034	5,066	28	0.0033	4,783
35,000	≈ 0	≈ 0	≈ 0	≈ 0	≈ 0	≈ 0

identical wind-power units. In the latter system, all four generators are of the WPSU type and altogether have a power rating equal to that of the system of Fig. 4.1. For both systems,  $P_{ch-max}$ ,  $P_{dch-max}$ , and FOR are 800 kW, 350 kW, and 5%, respectively, and only the islanded mode is considered.

Table 4.5 indicates that the reliability indices are more or less the same in both systems. The reason is that, with respect to the assumed load profile, the generators capacities in the two-generator system are such that the load could still be supplied if one of the generators fails. Hence, the modularity is not very advantageous in this case. The advantage of modularity, however, manifests itself if the load is so large that the failure of one of the two generators would most likely cause the load to exceed the generation.

#### 4.6.7 Case-7: Grid-Side Converter Rating

$P_{GSC}[h]$  is the power that flows through the GSC, at the given hour. Thus the absolute value of  $P_{GSC}[h]$  corresponds to the magnitude of power that the GSC must be able to handle in the  $h^{th}$  hour. To obtain an idea about the required GSC power rating, the absolute values of  $P_{GSC}[h]$  are sorted in a descending order and plotted versus the hour axis. The resultant curve is shown in Fig. 4.10 and can be interpreted in a way similar to an LDC (Fig. 4.2). Thus, Fig. 4.10 indicates the total number of hours during which the GSC power is larger than a certain value on the vertical axis. For our system of study, Fig. 4.10 shows that the GSC power is always lower than about 800 kW. This result is consistent with the discussion of Section 4.5 that the maximum value of  $|P_{GSC}|$  is about the same as  $P_{ch-max}$ . However, it will be remembered that, in determining the kVA rating of the GSC, the reactive power that this converter exchanges with the rest of the system must also be taken into consideration.

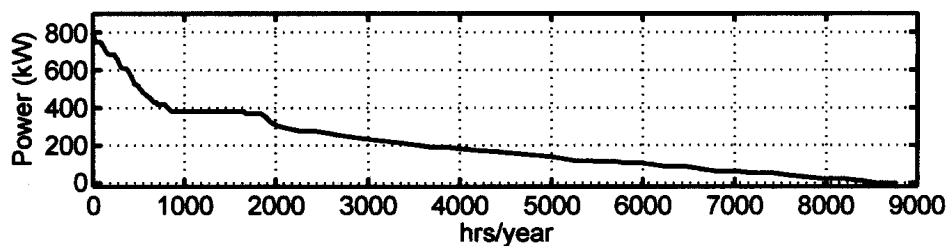


**Fig. 4.10:** A curve indicating the total number of hours per year during which the GSC power exceeds a certain value on the vertical axis

## **4.7 Summary**

Based on a new reliability assessment method, the reliability of the remote electrification system employing the WPSU was evaluated in this chapter. It was shown that many parameters impact the system reliability. Among those, the wind strength plays a significant role. However, the battery capacity plays the most crucial role; the impact of all other parameters become negligible at an adequately large battery capacity. It was also discussed that the battery maximum discharging power should be chosen slightly higher than the expected maximum load peak power. However, provided the battery is properly rated, the maximum charging power can be assigned a considerably larger value, to ensure rapid energy storage and higher reliability. It was further shown that the operation in the grid-connected mode results in a considerably higher reliability, for a given battery capacity, even if the grid is fairly unreliable.

## **Chapter 5**

# **Conclusions and Future Work**

### **5.1 Conclusions**

The modeling, control, and reliability of a doubly-fed induction generator (DFIG)-based wind-power system augmented with battery energy storage was studied in this thesis. The idea was to employ the proposed configuration and control for electrification of remote communities which are either completely isolated from or unreliably connected to a power grid, for the ultimate goal of mitigating the reliance on diesel-based electric power generation.

The thesis identified a control strategy and its constituents to enable the integration of battery energy storage. It was shown that the proposed control strategy enables the operation of the wind-power/storage system in both the off-grid (islanded) and grid-connected modes of operation. It was further demonstrated that under the developed control strategy, the wind-power/storage system can operate in parallel with constant-speed wind-power units, passive loads, and induction motor loads. The effectiveness of the

proposed control strategy was demonstrated through extensive simulation studies conducted by PSCAD/EMTDC software package.

The thesis also studied the reliability aspects of the proposed wind-power/storage system, for an example remote electrification system. A new reliability assessment method was developed in this thesis, which combines the existing analytical and simulation-based probabilistic approaches. Based on the developed reliability analysis method, it was shown that the capacity of the battery energy storage, magnitude and profile of wind, and the load profile impose remarkable impacts on the reliability of the overall electrification system. The analysis also indicated that, a connection to the power grid, however unreliable, significantly mitigates the need for a large battery to achieve a given degree of reliability.

## **5.2 Future Work**

The following topics are suggested as continuation of the research work reported in this thesis:

- Investigation on the feasibility and modeling/control aspects of an extended configuration which also embeds photovoltaic solar power units;
- A more focused investigation on the stability and robustness of the proposed control strategy, especially in the islanded mode of operation, to different load conditions; and
- A cost-benefit analysis and economical feasibility study on the proposed configuration.
- A more detailed modeling and characterization of battery requirements for remote electrification applications.

# Appendices

# Appendix A

## System Data

Tables A.1-A.5 provide data for the electrification system of Fig. 2.1. Table A.6 identifies the base values for the per-unit variables of Chapter 2.

**Table A.1:** Control System Parameters

Parameter	Value	Comments
$\tau_1$	1.0 ms	transfer-function (2.9)
$\tau_2$	1.0 ms	transfer-function (2.12)
$k_p$	28.27 MW/pu	see Fig. 2.2
$k_Q$	13.15 MVar/pu	see Fig. 2.4
$\tau_P$	2 ms	see Fig. 2.2
$\tau_Q$	2 ms	see Fig. 2.4
$V_{dc-L}$	1250 V	see Fig. 2.2
$V_{dc-H}$	1450 V	see Fig. 2.2
$V_{sm-ref}$	612 V	see Fig. 2.4

**Table A.2:** DFIG and Constant-speed Turbine Parameters

DFIG Turbine Parameter	Value	Comments
turbine radius, $r$	35.25 $m$	
$C_{pmax}$	0.41	
$\lambda_{opt}$	6.85	
$k_{opt}$	0.0144 $Nms^2$	
gearbox ratio, $N$	210	
effective inertia constant, $H$	0.25 $s$	
Constant-Speed Turbine Parameter	Value	Comments
turbine radius, $r$	18.84 $m$	
$C_{pmax}$	0.41	
$\lambda_{opt}$	3.49	
gearbox ratio, $N$	175	
effective inertia constant, $H$	0.25 $s$	

**Table A.3:** DFIG Parameters

DFIG Parameter	Value	Comments
nominal power	1.67 $MVA$	
nominal voltage	750 $V_{rms}$	line-to-line
nominal frequency	60 $Hz$	
number of poles	2	
rotor/stator turns ratio	3.0	
stator resistance, $R_s$	0.0092 $pu$	
rotor resistance, $R_r$	0.0082 $pu$	
magnetizing inductance, $L_m$	4.130 $pu$	
stator inductance, $L_s$	4.202 $pu$	
rotor inductance, $L_r$	4.202 $pu$	

**Table A.4:** Power-Electronic Interface and Network Parameters

Converter Parameter	Value	Comments
$T_{r1}$ nominal power	1.9 MVA	
$T_{r1}$ voltage ratio	13.8/0.75	Y/Delta
$T_{r1}$ leakage inductance	0.01 pu	
$T_{r1}$ ohmic resistance	0.01 pu	
on-state resistance of valves	1.2 mΩ	
interface inductance, $L$	447 μH	
interface resistance, $R$	4.8 mΩ	
shunt capacitance, $C_f$	235 μF	$Q_f = 50 \text{ kVAr}$
switching frequency	2340 Hz	$39 \times 60 \text{ Hz}$
DC-link capacitance, $C_L$	4000 μF	
battery internal EMF, $E_b$	1350 V	
battery inductance, $L_b$	20 μH	
battery resistance, $R_b$	59 mΩ	
Network and Interface Parameter	Value	Comments
grid voltage, $V_{gabc}$	13.8 kV <sub>rms</sub>	line-to-line
line inductance, $L_g$	6.3 mH	
line resistance, $R_g$	2.38 Ω	
$T_{r2}, T_{r3}$ nominal power	400 kVA	
$T_{r2}, T_{r3}$ voltage ratio	13.8/0.48	Y/Delta
$T_{r2}, T_{r3}$ leakage inductance	0.1 pu	
$T_{r2}, T_{r3}$ ohmic resistance	0.01 pu	
PF correction capacitance, $C_2$	825 μF	

**Table A.5: Induction Generator and Motor Parameters**

DFIG Parameter	Value	Comments
nominal power	400 <i>kVA</i>	
nominal voltage	480 $V_{rms}$	line-to-line
nominal frequency	60 <i>Hz</i>	
rotor/stator turns ratio	1.0	
stator resistance, $R_s$	0.010 <i>pu</i>	
rotor resistance, $R_r$	0.007 <i>pu</i>	
magnetizing inductance, $L_m$	4.250 <i>pu</i>	
stator inductance, $L_s$	4.318 <i>pu</i>	
rotor inductance, $L_r$	4.318 <i>pu</i>	

**Table A.6: Base Values for the WPSU Parameters**

Parameters	Values	Comments
base angular frequency and velocity	377 <i>rad</i>	
base voltage	0.612 <i>kV</i>	peak value, line-to-neutral
base current	1.826 <i>kA</i>	peak value
base power	1.677 <i>MVA</i>	

## Appendix B

### Nonlinear and Linearized Equations

For the purpose of dynamic analysis, the WPSU is divided into four subsystems: (1) the DFIG subsystem, (2) the PLL subsystem, (3) the capacitor subsystem, and (4) the grid-side converter (GSC) subsystem. The following sections present the equations corresponding to the aforementioned subsystems.

#### B.0.1 Equations of DFIG Subsystem

Dynamic equations of a DFIG are derived based on the generalized theory of rotating electric machines, using electromagnetic theory [30], or the concept of coupled inductors [33]. The equations are typically arranged for electric drive systems and not in the standard state-space form. However, they can be modified in a fairly straightforward manner and written in the state-space form, as follows.

$$\frac{d\hat{\lambda}_s}{dt} = -\frac{1}{\tau_s}\hat{\lambda}_s + v_{sd} \cos \delta - v_{sq} \sin \delta + \frac{L_m}{\tau_s}i_{rd} \quad (\text{B.1})$$

$$\frac{d\delta}{dt} = \omega - \frac{1}{\hat{\lambda}_s} (v_{sd} \sin \delta + v_{sq} \cos \delta) - \left( \frac{L_m}{\tau_s} \right) \frac{i_{rq}}{\hat{\lambda}_s} \quad (\text{B.2})$$

$$\frac{d\omega_r}{dt} = \frac{1}{J} \left[ T_{tur} - \frac{3}{2(1 + \sigma_s)} \hat{\lambda}_s i_{rq} \right] \quad (\text{B.3})$$

$$\frac{d\xi_d}{dt} = -i_{rd} + i_{rdref} \quad (\text{B.4})$$

$$\frac{d\xi_q}{dt} = -i_{rq} + i_{rqref} \quad (\text{B.5})$$

$$\begin{aligned} \frac{di_{rd}}{dt} = ai_{rd} + \left( \omega - \omega_0 - \frac{d\delta}{dt} \right) i_{rq} + \frac{k_{pt}}{\sigma\tau_r} i_{rdref} + \frac{k_{it}}{\sigma\tau_r} \xi_d + \frac{b}{\tau_s} \hat{\lambda}_s \\ -bv_{sd} \cos \delta + bv_{sq} \sin \delta \end{aligned} \quad (\text{B.6})$$

$$\frac{di_{rq}}{dt} = ci_{rq} + (i_{rd} + b\hat{\lambda}_s) \left( \omega - \omega_0 + \frac{d\delta}{dt} \right) + \frac{k_{pt}}{\sigma\tau_r} i_{rqref} + \frac{k_{it}}{\sigma\tau_r} \xi_q \quad (\text{B.7})$$

where

$$T_{tur} = h(\beta_{pitch}, V_w, \omega_r), \quad (\text{B.8})$$

$$i_{rqref} = \frac{2}{3} (1 + \sigma_s) \omega_0 k_{opt} \frac{\omega_r^2}{\sqrt{v_{sd}^2 + v_{sq}^2}} \quad (\text{B.9})$$

in which  $h(., ., .)$  is a nonlinear function,  $k_{opt}$  is a constant,  $k_{pt}$  and  $k_{it}$  are the proportional and integral gains of a PI compensator, and

$$a = - \left[ \frac{1}{\sigma\tau_r} + \frac{1 - \sigma}{\sigma\tau_s} + \frac{k_{pt}}{\sigma\tau_r} \right], \quad (\text{B.10})$$

$$b = \frac{(1 - \sigma)}{\sigma L_m} \quad (\text{B.11})$$

$$c = -\frac{(1 + k_{pt})}{\sigma\tau_r}. \quad (\text{B.12})$$

$\sigma$  is the DFIG leakage factor and defined as

$$\sigma = 1 - \frac{1}{(1 + \sigma_r)(1 + \sigma_s)}, \quad (\text{B.13})$$

where  $\sigma_r$  and  $\sigma_s$  are the rotor and stator leakage factors, respectively.  $\tau_s$  and  $\tau_r$  are, respectively, the stator and rotor time constants and defined as

$$\tau_s = \frac{(1 + \sigma_s)L_m}{R_s} \quad (\text{B.14})$$

$$\tau_r = \frac{(1 + \sigma_r)L_m}{R_r}. \quad (\text{B.15})$$

$i_{rdref}$  is often set equal to a constant value.

$i_{sd}$  and  $i_{sq}$  are the outputs of the DFIG subsystem and given by

$$i_{sd} = \frac{1}{\tau_s R_s} \left[ \hat{\lambda}_s \cos \delta - L_m(i_{rd} \cos \delta + i_{rq} \sin \delta) \right] \quad (\text{B.16})$$

$$i_{sq} = \frac{1}{\tau_s R_s} \left[ -\hat{\lambda}_s \sin \delta - L_m(i_{rq} \cos \delta - i_{rd} \sin \delta) \right]. \quad (\text{B.17})$$

## B.0.2 Equations of PLL Subsystem

The PLL is a dynamic system that processes  $v_{sq}$  by a filter and delivers  $\omega$ .

It is described by the following equations:

$$\frac{d\xi_{pll}}{dt} = \xi_{pll1} \quad (\text{B.18})$$

$$\frac{d\xi_{pll1}}{dt} = \xi_{pll2} \quad (\text{B.19})$$

$$\frac{d\xi_{pll2}}{dt} = \xi_{pll3} \quad (\text{B.20})$$

$$\frac{d\xi_{pll3}}{dt} = \xi_{pll4} \quad (\text{B.21})$$

$$\frac{d\xi_{pll4}}{dt} = -\alpha_1\xi_{pll1} - \alpha_2\xi_{pll2} - \alpha_3\xi_{pll3} - \alpha_4\xi_{pll4} + v_{sq}; \quad (\text{B.22})$$

The output equation for the PLL subsystem is

$$\omega = \beta_0\xi_{pll} + \beta_1\xi_{pll1} + \beta_2\xi_{pll2} + \beta_3\xi_{pll3} + \beta_4\xi_{pll4}, \quad (\text{B.23})$$

where  $(\alpha_1, \dots, \alpha_4)$  and  $(\beta_0, \dots, \beta_4)$  are the parameters of the PLL filter.

### B.0.3 Equations of Capacitor Subsystem

The capacitor subsystem is described by the following equations:

$$\frac{dv_{sd}}{dt} = \omega v_{sq} + \frac{1}{C_f} (i_{cd} - i_{sd} - i_{td}) \quad (\text{B.24})$$

$$\frac{dv_{sq}}{dt} = -\omega v_{sd} + \frac{1}{C_f} (i_{cq} - i_{sq} - i_{tq}). \quad (\text{B.25})$$

$v_{sd}$  and  $v_{sq}$  are also the outputs of the capacitor subsystem.

### B.0.4 Equations of GSC Subsystem

The GSC subsystem is described by the following equations:

$$\frac{di_{cd}}{dt} = -\frac{1}{\tau_i} i_{cd} + \frac{1}{\tau_i} i_{cdref} \quad (\text{B.26})$$

$$\frac{di_{cq}}{dt} = -\frac{1}{\tau_i}i_{cq} + \frac{1}{\tau_i}i_{cqref} \quad (\text{B.27})$$

$$\frac{di_{cdref}}{dt} = -\frac{1}{\tau_p}i_{cdref} + \frac{k_p\omega_0}{\tau_p} - \frac{k_p}{\tau_p}\omega \quad (\text{B.28})$$

$$\frac{di_{cqref}}{dt} = -\frac{1}{\tau_Q}i_{cqref} + \frac{k_Q\hat{v}_{sn}}{\tau_Q} - \frac{k_Q}{\tau_Q}\sqrt{v_{sd}^2 + v_{sq}^2}, \quad (\text{B.29})$$

where  $k_p$  and  $\tau_p$  are the parameters of the real-power management scheme, i.e. Fig. 2.2. Similarly,  $k_Q$  and  $\tau_Q$  are the parameters of the reactive-power management scheme, Fig. 2.4. The constants  $\omega_0$  and  $\hat{v}_{sn}$  are the nominal value of the frequency, and the PCC line-to-neutral peak voltage, respectively. It is pointed out that  $i_{cd}$  and  $i_{cq}$  are also the outputs of the GSC subsystem.

## References

- [1] [Online]. Available: <http://www.solarenergy.org>.
- [2] J. Ayoub, S. Henderson, R. Alward and F. Sheriff, "Living off-grid on renewable energy in the Yukon," *SESCI 2004 Conference*, Waterloo, Canada, August 2004, 12 pages. Also available on-line at <http://canmetenergy.nrcan.gc.ca/fichier.php/codectec/En/2004-128/2004-128e.pdf>.
- [3] Hydro One Inc., [Online]. Available: <http://www.hydroone.com>.
- [4] F. Katiraei and C. Abbey, "Diesel plant sizing and performance analysis of a remote wind-diesel microgrid," *IEEE Power Engineering Society General Meeting, PES 2007*, Tampa, USA, June 2007, 8 pages.
- [5] D. G. Infield, G. W. Slack, N. H. Lipman and P. J. Musgrove, "Review of wind/diesel strategies," *IEE Proceedings*, vol. 130, no. 9, pp. 613-619, December 1983.
- [6] C. V. Nayar, W. B. Lawrance and S. J. Phillipps, "Solar/wind/diesel hybrid energy systems for remote areas," *24th Intersociety Energy Conversion Engineering Conference, IECEC 89*, Washington DC, USA, August 1989, vol. 4, pp. 2029-2034.
- [7] T. V. Chambers and J. Mutale, "Selection of diesel generators for small rural wind-diesel power systems," *41st International Universities Power Engineering Conference, UPEC 06*, Newcastle, UK, September 2006, vol. 1, pp. 51-55.
- [8] A. S. Kini and U. R. Yaragatti, "Modeling and simulation of a wind/diesel hybrid power systems," *IEEE International Conference on Industrial Technology, ICIT 06*, Mumbai, India, December 2006, pp. 1670-1675.

- [9] P. A. Scott and M. A. Mueller, "Modeling fully variable speed hybrid wind-diesel systems," *41st International Universities Power Engineering Conference, UPEC 06*, Newcastle, UK, September 2006, vol. 1, pp. 212-216.
- [10] L. A. C. Lopes and R. G. Almeida, "Wind-driven self-excited induction generator with voltage and frequency regulated by a reduced-rating voltage source inverter," *IEEE Transactions on Energy Conversion*, vol. 21, no. 2, pp. 297-304, June 2006.
- [11] J. P. Barton and D. J. Infield, "Energy storage and its use with intermittent renewable energy," *IEEE Transactions on Energy Conversion*, vol. 19, No. 2, pp. 441-448, June 2004.
- [12] R. Billinton, Bagen and Y. Cui, "Reliability evaluation of small stand-alone wind energy conversion systems using a time series simulation model," *IEE Proceedings – Generation, Transmission, and Distribution*, vol. 150, no. 1, pp. 96-100, January 2003.
- [13] Bagen and R. Billinton, "Incorporating well-being considerations in generating systems using energy storage," *IEEE Transactions on Energy Conversion*, vol. 20, No. 1, pp. 225-230, March 2005.
- [14] Bagen and R. Billinton, "Evaluation of different operating strategies in small stand-alone power systems," *IEEE Transactions on Energy Conversion*, vol. 20, no. 3, pp. 654-660, September 2005.
- [15] M. Korpas and A. T. Holen, "Operation planning of hydrogen storage connected to wind power operating in a power market," *IEEE Transactions on Energy Conversion*, vol. 21, no. 3, pp. 742-749, September 2006.
- [16] S. Miyake and N. Tokuda, "Vanadium redox-flow battery for a variety of applications," *Power Engineering Society General Meeting, PES 2001*, pp. 450-451, July 2001.
- [17] A. Arulampalam, M. Barnes, N. Jenkins and J. B. Ekanayake, "Power quality and stability improvement of a wind farm using STATCOM supported with hybrid battery energy storage," *IEE Proceedings – Generation, Transmission, and Distribution*, vol. 153, no. 6, pp. 701-710, November 2006.
- [18] D. J. Swider, "Compressed air energy storage in an electricity system with significant wind power generation," *IEEE Transactions on Energy Conversion*, vol. 22, no. 1, pp. 95-102, March 2007.

- [19] M. Black and G. Strbac, "Value of bulk energy storage for managing wind power fluctuations," *IEEE Transactions on Energy Conversion*, vol. 22, no. 1, pp. 197-205, March 2007.
- [20] T. Ackermann, et al, *Wind Power in Power Systems*, John Wiley & Sons, 2005.
- [21] R. Cardenas, R. Pena, G. Asher and J. Clare, "Power smoothing in wind generation systems using a sensorless vector controlled induction machine driving a flywheel," *IEEE Transactions on Energy Conversion*, vol. 19, no. 1, pp. 206-216, March 2004.
- [22] C. Abbey and G. Joos, "Integration of energy storage with a doubly-fed induction machine for wind power applications," *Proceedings of IEEE Power Electronics Specialists Conference, PESC 04*, vol. 3, pp. 1964-1968, June 2004.
- [23] M. Aktarujjman, M. A. Kashem, M. Negnevitsky and G. Ledwich, "Control stabilisation of an island system with DFIG wind turbine," *1st International Power and Energy Conference, PECon 2006*, pp. 312-317, November 2006.
- [24] M. C. Chandorkar, D. Divan and R. Adapa, "Control of parallel connected inverters in stand-alone ac supply systems," *IEEE Transactions on Industry Applications*, vol. 29, no. 1, pp. 136-143, September 2004.
- [25] Y. Li, D. M. Vilathgamuwa and P. C. Loh, "Design, analysis, and real-time testing of a controller for multibus microgrid system," *IEEE Transactions on Power Electronics*, vol. 19, no. 5, pp. 1195-1204, September 2004.
- [26] PSCAD/EMTDC v. 4.2, Manitoba HVDC Research Centre, Winnipeg, MB, Canada.
- [27] H. Verwijs, "Europe turns a blind eye to big battery," *European Energy Review*, vol. 2, no. 3, pp. 72-74, March-April 2009.
- [28] J. Cousseau, C. Siret, P. Biensan and M. Broussely, "Recent developments in Li-ion prismatic cells," *Journal of Power Sources*, vol. 162, no. 2, pp. 790-796, November 2005.
- [29] R. Datta and V. T. Ranganathan, "Variable-speed wind-power generation using doubly fed wound rotor induction machine - a comparison with alternative schemes," *IEEE Transactions on Energy Conversion*, vol. 17, no. 3, pp. 414-421, September 2002.
- [30] W. Leonhard, *Control of Electrical Drives*, 3rd ed., Springer, 2001.

- [31] C. Schauder and H. Mehta, "Vector analysis and control of advanced static VAR compensators," *IEE Proceedings – Generation, Transmission, and Distribution*, vol. 140, no. 4, pp. 299-306, July 1993.
- [32] B. G. Rawn, "Wind energy conversion systems as power filters: a control methodology," *M.A.Sc. Thesis, University of Toronto, ON, Canada*, 2004.
- [33] A. Yazdani and R. Iravani, *Voltage-Sourced Converters in Power Systems*, John-Wiley & Sons, 2010.
- [34] P. Kundur, *Power System Stability and Control*, McGraw Hill, 1994.
- [35] A. Yazdani and P. P. Das, "A Control methodology and characterization of dynamics for a photovoltaic (PV) system interfaced with a distribution network," *IEEE Transactions on Power Delivery*, vol. 24, no. 3, pp. 1195-1204, July 2009.
- [36] A. G. Bakirtzis, "A probabilistic method for the evaluation of the reliability of stand alone wind energy systems," *IEEE Transactions on Energy Conversion*, vol. 7, no. 1, pp. 99-107, March 1992.
- [37] K. R. Voorspools and W. D. D'haeseleer, "Are deterministic methods suitable for short term reserve planning?," *Journal of Energy Conversion and Management*, vol. 46, no. 13-14, pp. 2042-2052, August 2005.
- [38] R. Billinton and R. N. Allan, *Reliability Evaluation of Power Systems*, 2nd ed., New York: Plenum, 1996.
- [39] R. Billinton and R. N. Allan, *Reliability Evaluation of Engineering Systems*, 2nd ed., New York: Plenum, 1992.
- [40] A. Ehsani, M. Fotuhi, A. Abbaspour and A. M. Ranjbar, "An analytical method for the reliability evaluation of wind energy systems," *IEEE International Region 10 Conference, TENCON 05*, Melbourne, Australia, November 2005, 7 pages.
- [41] A. A. Chowdhury, "Reliability models for large wind farms in generation system planning," *IEEE Power Engineering Society General Meeting*, San Francisco, USA, June 2005, vol. 2, pp. 1926-1933.

- [42] X. Liu and S. Islam, "Reliability evaluation of a wind-diesel hybrid power system with battery bank using discrete wind speed frame analysis," *9th International Conference on Probabilistic Method Applied to Power Systems*, Stockholm, Sweden, June 2006, 7 pages.
- [43] G. M. Masters, *Renewable and Efficient Electric Power Systems*, New Jersey: John Wiley & Sons Inc., 2004.
- [44] P. Giorsetto and K. F. Utsurogi, "Development of a new procedure for reliability modeling of wind turbine generators," *IEEE Transactions on Power Apparatus and Systems*, vol. PAS-102, no. 1, pp. 134-143, January 1983.
- [45] I. Abouzahr and R. Ramakumar, "Loss of power supply probability of stand-alone wind electric conversion systems: a closed form solution approach," *IEEE Transactions on Energy Conversion*, vol. 5, no. 3, pp. 445-452, September 1990.
- [46] I. Abouzahr and R. Ramakumar, "An approach to assess the performance of utility-interactive wind electric conversion systems," *IEEE Transactions on Energy Conversion*, vol. 6, no. 4, pp. 627-638, December 1991.
- [47] A. C. Saramourtsis, A. G. Bakirtzis, P. S. Dokopoulos and E.S. Gavanidou "Probabilistic evaluation of performance of wind-diesel energy systems," *IEEE Transactions on Energy Conversion*, vol. 9, no. 4, pp. 743-752, December 1994.
- [48] S. H. Karaki and R. B. Chedid, "Probabilistic performance assessment of wind energy conversion systems," *IEEE Transactions on Energy Conversion*, vol. 14, no. 2, pp. 217-224, June 1999.
- [49] R. Billinton, H. Chen and R. Ghajar, "Time-series models for reliability evaluation of power systems including wind energy," *Journal of Microelectronics and Reliability*, vol. 36, no. 9, pp. 1253-1261, 1996.
- [50] R. Karki, P. Hu and R. Billinton, "A simplified wind power generation model for reliability evaluation," *IEEE Transactions on Energy Conversion*, vol. 21, no. 2, pp. 533-540, June 2006.
- [51] R. Karki, P. Hu and R. Billinton, "Reliability evaluation of a wind power delivery system using an approximate wind model," *41st International Universities Power Engineering Conference, UPEC 06*, Newcastle, UK, September 2006, vol. 1, pp. 113-117.

- [52] B. S. Borowy and Z. M. Salameh, "Methodology for optimally sizing the combination of a battery bank and PV array in a wind/PV hybrid system," *IEEE Transactions on Energy Conversion*, vol. 11, no. 2, pp. 367-375, June 1996.
- [53] F. M. A. Ghali, M. M. A. Aziz and F. A. Syam, "Simulation and analysis of hybrid systems using probabilistic techniques," *Power Conversion Conference*, Naqaoka, Japan, August 1997, vol. 2, pp. 831-835.
- [54] P. F. Albretch, and Test System Task Force, "IEEE reliability test system," *IEEE Transactions on Power Apparatus and Systems*, vol. PAS-98, no. 6, pp. 2047-2054, November/December 1979.
- [55] [Online]. Available: <http://www.climate.weatheroffice.ec.gc.ca>.